EXPERIMENTAL INVESTIGATION OF WIND-FORCED DROP STABILITY

A Dissertation

by

JASON ALLEN SCHMUCKER

Submitted to the Office of Graduate Studies of
Texas A&M University
in partial fulfillment of the requirements for the degree of

DOCTOR OF PHILOSOPHY

August 2012

Major Subject: Aerospace Engineering

Experimental Investigation of Wind-Forced Drop Stability

EXPERIMENTAL INVESTIGATION OF WIND-FORCED DROP STABILITY

A Dissertation

by

JASON ALLEN SCHMUCKER

Submitted to the Office of Graduate Studies of
Texas A&M University
in partial fulfillment of the requirements for the degree of

DOCTOR OF PHILOSOPHY

Approved by:

Chair of Committee,	Edward B. White
Committee Members,	Rodney Bowersox
	Adonios Karpetis
	Kristen Maitland
Head of Department,	Dimitris Lagoudas

August 2012

Major Subject: Aerospace Engineering

ABSTRACT

Experimental Investigation of Wind-Forced Drop Stability. (August 2012)

Jason Allen Schmucker, B.A., Goshen College; M.S., Case Western Reserve University

Chair of Advisory Committee: Dr. Edward B. White

The stability of drops forced by both wind and gravity is a fluid mechanics problem relevant to heat exchangers, fuel cells, and aircraft icing. To investigate this phenomenon, drops from 15 μL to 400 μL were placed on the rough aluminum ($R_A = 3.26$ μm) floor of a tiltable wind tunnel and brought to critical conditions, when the drop begins to run downstream. Various combinations of drop size, inclination angle, and flow speed were employed. A measurement technique capable of measuring full 3D drop profiles was implemented to investigate the drops' evolution toward runback. The measurement requires the comparison of the speckle pattern captured by an overhead drop image with a corresponding image of the dry surface. Stability limits for 235 drops are measured as functions of drop volume and surface inclination. Drops experiencing airflow alone are found to shed at a Weber number of 8.0 ± 0.5. From measurement sequences of reconstructed drop profiles, the evolution of contact lines, drop profiles, and contact angle distributions are detailed. Contact line integral adhesion forces are calculated from contact angle distributions and related to the forcing air velocity. Drops whose stability limits are dominated by gravity are found to exhibit significantly different evolution toward runback than those dominated by airflow.

To my wife, Melanie

ACKNOWLEDGEMENTS

I extend humble thanks to many people without whom the process of completing this work would have been far more difficult. To my advisor, Dr. Edward White, I owe many thanks for your guidance, motivation, and confidence in me. The benefits I have received from your mentoring over the past seven years are far too numerous to list here. You were always there with support and encouragement when the inevitable obstacles appeared.

I would also like to thank the other members of my committee, Drs. Rodney Bowersox, Adonios Karpetis and Kristen Maitland, for their input in my research, along with many provocative questions that encouraged further exploration.

To my undergraduate advisor, Dr. Carl Helrich, I am thankful for your encouragement to pursue graduate education. You first introduced me to scientific research and instilled in me an appreciation for the wonder of the natural world. Without you I would not be where I am today.

For their assistance in the tedious process of data collection, I owe Jason Monschke and Calin Canahai many thanks. Josh Osterhout was instrumental in the design and construction of the experimental rig. I am also thankful to many other fellow graduate students in the Aerospace Engineering department, including Nick Denissen, Rob Downs, Julie Parish, Nicole Sharp, Bobby Ehrmann, and Jamie Weber. Together we shared in the experience of graduate school, commiserated over setbacks in our research, celebrated our triumphs, and made progress together. You helped make this an enjoyable experience.

I am thankful for the continual love of all my family, who were always supportive of me along this path through the long years it has taken. I thank my dad for his constant and genuine interest in my work and all those Friday afternoon phonecalls to check up on my progress and encourage me. And to my wife, Mel, my constant companion, I love you. Together we decided to leave our homes—where we grew up, went to college together, and got married—so that I could pursue this degree. And while it wasn't always easy, without a doubt we have grown closer together and achieved something special. Without your support, none of this could have happened.

TABLE OF CONTENTS

Page

CHAPTER Page

LIST OF FIGURES

FIGURE Page

FIGURE Page

FIGURE Page

CHAPTER I

INTRODUCTION

When a liquid drop rests on a surface in the presence of airflow, the drop may either remain fixed in place or run back along the surface. At low flow speeds, the downstream force provided by the airflow is balanced by the adhesion force between the drop and the surface. At higher velocities, the force exerted on the drop by the flow exceeds the ability of the drop to adhere to the surface and it runs downstream.

The practical implications of whether wind forcing can dislodge a drop from a surface affect aircraft icing, heat exchangers, fuel cells and other industrial processes. In situations requiring the removal of liquid drops from a surface, drops' response to forcing is critical. As an example, heat exchanger efficiency can be enhanced via condensation of liquid drops and smaller drops lead to better performance (Kandlikar and Steinke, 2002). So, a condenser surface produced to shed the smallest possible drops will be more efficient as it allows new drops to condense in the spaces left by shed drops, and thus increase heat transfer.

In a fuel cell, hydrogen and oxygen combine to produce electricy and waste water. Fuel cells utilizing proton exchange membranes produce this waste water in the form of drops at the membrane interface. Air flowing above the membrane sweeps away the drops if the flow is above a critical velocity (Theodorakakos et al., 2006). This shedding process is critical both for exhausting the waste products and, more importantly, because the amount of water in the membrane influences the efficiency of the fuel cell.

This dissertation follows the style of Experiments in Fluids.

The formation of ice on aircraft can be catastrophic. At relatively warm temperatures, the accretion of ice depends strongly on the behavior of liquid water on the wing. Icing prediction codes such as `LEWICE` (2008) attempt to simulate the entire aircraft-icing process from tracking the water drops in the freestream, to the collection and movement of liquid water on the wing surface, and finally freezing and ice growth (Kind et al., 1998, Cebeci and Kafyeke, 2003). To accomplish this requires accurate models of the transport of liquid water on the surface. Early models of the process assumed a thin water film was responsible for transport of water on the wing (Messinger, 1953). However, Olsen and Walker (1986) observed both stationary drops near the stagnation region and larger drops moving downstream; these conditions contradicted the established modeling assumptions of Messinger, which are widely used in computation of ice formation on aircraft. It is well known that ice accretion rates depend strongly on whether impinging water drops remain fixed near a wings leading edge or whether they are swept away by wind forcing before they can freeze (Kind et al., 1998). Nevertheless, the Messinger model remains the predominant method for calculating ice accretion rates, due to the lack of detail in understanding the drop runback problem. Improved understanding of the drop runback process will enable better modelling of the runback problem and prediction of ice accretion.

A. Drop Physics

A liquid drop on a solid surface forms an interface with the surrounding gas that meets the solid at the contact line, where all three phases intersect. The angle between the surface and the tangent to the liquid/gas interface is the contact angle, θ. The interface between the solid, liquid, and gas phase possesses a surface energy and corresponding interfactial tensions γ_{sl}, γ_{lg}, and γ_{sg}. Young's equation,

$\gamma_{\mathrm{lg}} \cos(\theta_i) = \gamma_{\mathrm{sg}} - \gamma_{\mathrm{sl}}$ predicts the ideal contact angle of a system from these interfacial tensions. The equation represents a one-dimensional balance of forces. The surface tensions determine the extent to which a liquid wets a surface. Highly wetting systems have low contact angles and the drop spreads over the surface to a much greater extent than low wetting systems, such as superhydrophobic surfaces that can have contact angles well over 100°.

Laplace related the surface tension of the interface to the curvature and surface tension of the liquid through the Young–Laplace equation:

$$\begin{aligned} \Delta p &= -\gamma \nabla \cdot \hat{n} \\ &= \gamma \left(\frac{1}{R_1} + \frac{1}{R_2} \right), \end{aligned} \tag{1.1}$$

where $\hat{n}$ is the surface normal and R_1 and R_2 are the radii of curvature. The surface tension acting on the interface is balanced by a pressure jump across the interface. Thus, in the absence of gravity, the action of surface tension will pull a drop into a spherical cap shape with an internal pressure higher than the ambient. Gravity tends to flatten a drop from the spherical cap shape it would take due to surface tension.

In practice, all real surfaces are rough and contain chemical inhomogeneities. This complicates the application of Young's equation for contact angle and introduces hysteresis. The contact angle can take on a range of values between the advancing contact angle, θ_{a}, and the receding contact angle, θ_{r}. The hysteresis is defined as their difference, $\Delta\theta = \theta_{\mathrm{a}} - \theta_{\mathrm{r}}$. Chemical inhomogeneities can alter the thermodynamics of the system on a small scale, changing the hydrophobicity or hydrophilicity of the surface. Even in the absence of inhomogeneities, rough surfaces are comprised of many points with different slopes relative to the nominal surface plane. As a result, the apparent macroscopic contact angle is a combination of the intrinsic contact angle from Young's equation and the local surface angle, as in Fig. 1. The Wenzel

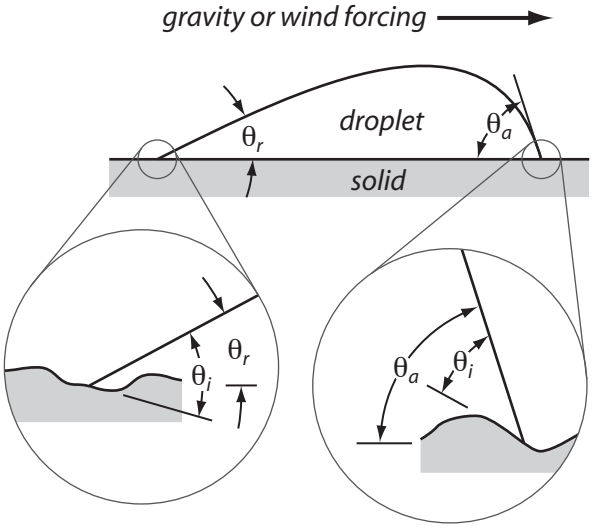

Fig. 1 : Surface roughness and contact angle hysteresis

equation (1936) relates the apparent contact angle θ_{W} to the intrinsic contact angle as $\cos\theta_{\mathrm{W}} = r\cos\theta_i$, where r is the ratio of wetted area to projected area ($r = 1$ for perfectly smooth surfaces and $r > 1$ for rough surfaces). However, the Wenzel equation makes no predictions about contact angle hysteresis. Marmur (1996) gives a detailed explanation of how a drop on a rough surface is able to occupy one of many metastable states. Wolansky and Marmur (1999) demonstrate that the drop configuration which has a circular contact line with contact angle θ_{W} about the entire perimeter is the minimum energy among all the states. However, the Wenzel equation only applies for axisymmetric drops much larger than the roughness scale. Marmur (2006) and Tadmor (2008) discuss some of the intricacies and fundamental issues present when measuring and discussing contact angles on imperfect surfaces.

Drops on a surface are often subjected to external forces. The stability problem involves a complex balance of forces on the drop and the motion of the three-phase contact line about the drop's perimeter. The literature on drop stability does not

provide a consistent definition for the drop stability limit. For this dissertation, the drop stability limit or runback is defined as the point when the drop can no longer maintain adhesion to the surface and begins to run downstream, as noted by motion of the rearmost point on the receding contact line. This is the point of incipient motion, after which the drop will continue to run.

The most common types of forces experienced by drops are gravity and wind. When a drop is subjected to gravity forcing on a non-horizontal substrate, the downslope component of the gravity force is $W\sin(\alpha)$, where W is the weight of the drop and α is the inclination angle of the surface. Gravity provides a body force, a simpler case than the conditions of wind forcing. The Bond number describes the ratio of gravitational forces and surface tension and is defined as $Bo = \rho g \ell^2/\gamma$, where ℓ is a reference length such as drop height, h.

Wind forcing involves the motion of the surrounding fluid and the internal flow within the drop, which are coupled at the drop interface, the location of which can be unsteady. (The runback stability limit does not necessarily coincide with the onset of interface unsteadiness.) Drops forced by surrounding airflow are subjected to both pressure and viscous stresses. When viscous shear forces are expected to dominate, the capillary number, $Ca = \mu U_{\text{ref}}/\gamma$, becomes important, where μ is the drop viscosity and U_{ref} is a reference velocity. When pressure forces are dominant, the Weber number, $We = \rho U_{\text{ref}}^2 \ell/\gamma$ becomes important. In systems where the capillary number is important, the ratio of drop viscosity to moving fluid viscosity is important. Viscosity ratio influences both the rate of drop deformation with increasing flow velocity and the equilibrium conditions (Dimitrakopoulos, 2007). Likewise, density ratio becomes important for Weber number dominated systems. Given its ubiquity, the water/air system was chosen as the working fluid for all experiments performed. This prevents the use of viscosity and density ratios as parameters of interest, as is

common in computational studies.

The characteristics of the flow provide a critical component to the stability of a wind-forced drop. The force aplied to a drop by the flow is influenced by whether the drop experiences a uniform velocity, uniform shear, or the flow in a specific boundary layer profile. Laminar and turbulent flows may also produce different effects in the forced drop. The drop-based Reynolds number is $Re = \rho U_{\text{ref}} h/\mu$. The low Reynolds number regime is characterized by smooth steady flow over the drop. Flow visualizations by Acarlar (1987) revealed the development of hairpin vortices shedding from flow over hemispheres in a boundary layer for height-based Reynolds number greater than about 120. For higher Reynolds numbers, these shedding vortices produce unsteady pressure fluctuations, and in the case of a liquid drop can induce large oscillations of the drop/air interface. Such behavior has been experimentally observed (White and Schmucker, 2008). The drag forces on a drop are highly contingent upon the drop shape, and thus the contact angle, wetting characteristics, and impinging flow field of the system.

B. Research History

The behavior of liquid drops in conditions of partial wetting has been studied from a variety of perspectives, including physical chemistry, thermodynamics, and fluid dynamics and across molecular to drop-sized length scales (de Gennes, 1985). A wealth of knowledge has been gained concerning the basic characteristics and physics of drops on surfaces, under both sessile drop conditions, the more complicated case when a drop experiences external forces, and even the dynamics of drop motion along a surface. Nevertheless, gaps in understanding remain, particularly in the case of wind-forced drops on rough surfaces, which still present significant barriers to

understanding from theoretical, computational, and experimental approaches. The following discussion details the history and current state of drop stability research from theoretical, computational and experimental perspectives. A review of relevant experimental techniques is presented with the goal of motivating the present application of a new drop measurement method to the study of wind-forced drops.

1. Drop Stability and Behavior

Early experiments revealed that an increase in contact angle hysteresis increases a drop's ability to resist motion along a surface. Experiments by MacDougall and Ockrent (1942), Bikerman (1950), and Furmidge (1962) confirm this phenomenon. Their observations consisted mainly of such macroscopic parameters as surface tilt angle, volume, width, length, surface tension, and advancing and receding contact angles. MacDougall and Ockrent tilted drops and captured side projections of the drop area, noting that at the critical inclination the contact angle is always θ_a at the furthest point on the downslope side and θ_r on the upslope side, independent of the initial drop shape. Furmidge developed a theory to correlate the retention of drops to the contact angle hysteresis. Bikerman performed a series of experiments to find critical inclination angles for a variety of drop sizes on stainless steel surfaces of varying roughness. Ultimately, expressions were derived for the stability conditions based on these macroscopic parameters.

Bikerman's surfaces ranged in rms profile height from 0.030 to 3.1 μm with nominal contact angles in the range of 60° to 91°. For drop volumes of 50 to 400 μL, the critical tilt angles for the smoothest surface spanned the range of 6.75° to 28°. On the roughest surface with greater hysteresis, the same drop volumes correspond to incipient sliding at 13.5° and 59.5°. Bikerman observed advancement of downslope portion of the contact line even at the slightest inclination angles. Subsequently, the

drops attained a static equilibrium in the new elongated configuration. Bikerman concluded that modifications to the contact line and contact angle are critical to the drop stability problem. Unfortunately, the measurement techniques applied by Bikerman permit only a global understanding of the stability problem, leading Bikerman to lament that "An exact test is impossible as the shape of the drop is too intricate."

More recent work by ElSherbini (2004a, 2004b) attempted to characterize the full drop profile of a gravity-forced drop. An apparatus was constructed to rotate the sideview camera around the tilted drop, recording sideview slices through the drop that could be combined to produce a full profile. The contact line was fit by matched ellipses for the front and rear portions of the drop; drop profile slices were modeled with matched circular arcs. These results conflict with the contact line shapes observed by Bikerman, perhaps suggesting that drop shape and behavior under forcing is highly dependent upon system characteristics.

Much of the theory concerning the stability of drops is credited to Dussan and coworkers. Dussan (Dussan V. and Davis, 1974, Dussan V., 1976) performed experiments designed to investigate the boundary conditions at the moving contact line and developed a theoretical model for the observed behavior. Dussan and Chow (1983) developed a lubrication model of drop stability on tilted surfaces based on the assumption that the contact angle is θ_a everywhere on the downslope side and θ_r everywhere on the upslope side, with these curved portions connected by two parallel straight line segments. The straight line segments are required in their model to prevent a singularity in the contact angle. This modeling assumption was based on observations from earlier experiments by Furmidge (1962) and Bikerman (1950).

Dussan's asymptotic solution was limited to drops with small surface slopes and small hysteresis ($\theta_a \ll 1$ and $(\theta_r - \theta_a)/\theta_a \ll 1$). Once again, it was observed that

the contact angle hysteresis is the single most important factor in determining drop stability, and that proper treatment of the boundary conditions, especially at the contact line, is of utmost importance for proper solution of the problem. Dussan continued this series of papers first by eliminating the constraint of small surface slopes (Dussan V., 1985) (with maximum hysteresis of 10°) and subsequently solving the stability problem when the surrounding fluid is in motion (Dussan V., 1987), resulting in a critical shear rate dependent on the system contact angles, surface tension, and fluid viscosity. The latter solution, however, is limited to small advancing contact angle and small hysteresis.

A recent experimental study by Milne (2009) further confirmed that wetting parameters such as contact angle play a crucial role in determining the drop shedding threshold. A scaling analysis predicts the critical velocity to be

$$U_{\text{crit}} = \sqrt{\frac{2kL_b\gamma\left(\cos\theta_{\text{r}} - \cos\theta_{\text{a}}\right)}{\rho A C_D}} \tag{1.2}$$

where A and L_b are the sideview drop area and base length of the unforced drop. The parameter k and the drag coefficient C_D account for the variable adhesion force the drop experiences due to different contact line and contact angle configurations. The water and hexadecane drops on PMMA, Teflon, and a superhydrophobic aluminum surface had drop heights in the range of 0.9 to 2.5 times the boundary layer thickness. A fit for the experimental critical air velocity data depended upon the parameter group $(L_b/A)^{1/2}$ and was valid for three different surfaces.

Numerical simulations have also provided insight into the intricacies of the drop stability problem. Durbin (1988) used a free-streamline method to investigate the stability of two-dimensional drops to wind forcing at high Reynolds numbers. The drop's heights were equal to or greater than the boundary layer thickness and stability limits were expressed as critical Weber numbers as functions of contact angle and

$\Delta\theta$. Feng and Basaran (1994) considered the stability of 2D drops at small Reynolds numbers. They found a strong dependence of the stability limit on Weber number and that the drops tend to evolve according to two main mode shapes.

Li and Pozrikidis (1996) performed 3D simulations of shear flow over a drop adhering to a surface in the absence of gravity. The viscosity ratio was one and contact lines were restricted to be circular or elliptic and remained pinned in this position throughout the simulation. Drops with elliptic contact lines were found to be less stable to forcing. Drop shapes were found to qualitatively agree with the two dimensional results of Feng and Basaran (1994).

Dimitrakopoulos and Higdon (1997, 1998) performed numerical simulations of the Ca thresholds, stability, and equilibria of two- and three-dimensional drops. These papers were intended for comparison and validation of the lubrication limit theories of Dussan and coworkers. They concluded the useful range of Dussan's lubrication model is very limited.

More recently, Dimitrakopoulos (2007) examined which portions of circular contact lines move first for low Reynolds numbers. Ding and Spelt (2008) performed numerical simulations of three-dimensional drops on a wall at low Reynolds number and found good agreement with the low-Re results of Dimitrakopoulos. They provided detailed plots of the contact line shape and the contact angle distribution around the contact line just before and after the critical flow speed.

Disagreement exists in the literature on the variation of contact angle along the contact line of a drop. Clearly, the variation must be continuous, but the steepness of jumps in contact angle is not widely agreed upon or even consistent between different studies. For example, considering gravity-forced drops, ElSherbini and Jacobi (2004a,b) found the contact angle varied smoothly about the entire contact line and could be well described by a third-degree polynomial. However, Dimitrakopoulos and

Higdon (1999) found the contact angle to jump from θ_r to θ_a within around 30° of circumferential position. Similar steep jumps in contact angle were observed by Ding and Spelt (2008) in the case of wind-forced drops. Conversely, Li and Pozrikidis (1996) found the contact angle to vary smoothly around the drop perimeter.

Moreover, there is disagreement on the shape the contact lines takes while under forcing from gravity or airflow. Many models include assumptions about the distribution of contact angle about the drop perimeter. For example, Dussan (1985) assumed the contact line takes the shape of two arcs connected by a straight section, in accordance with the observations of Bikerman (1950). ElSherbini (2004a, 2004b) proposed the contact line of gravity forced drops is best fit by two matched ellipses which is a similar approach. Extrand and Kumagai (1995) also observed front-to-back asymmetry of gravity-forced drops and employed an elliptic contact line model. The simulations of Dimitrakopoulos, however, produced drops which initially elongated in the transverse, rather than downstream direction under certain conditions.

2. Drop Shape Measurement Techniques

The techniques used in drop stability experiments have not undergone significant changes for many decades. Experiments typically use global observations of drop parameters to produce stability correlations and make conclusions about the nature of the drop stability problem. It is instructive to review techniques applied by other researchers and the current best practices for drop stability experiments. Doing so clarifies the need for more comprehensive experimental data.

In Bikerman's early study, a topview camera was used to record the dimensions and shape of the drop. Drop volume and surface tilt angle were also recorded. Topview and side cameras remain the most common technique applied by the research community. For example, Podgorski, et al. (2001) performed a simple qualitative study of the

behavior of the dynamic contact line of drops running down an inclined plane using a topview camera. This allowed a classification of drop behaviors over different ranges of the capillary number. As capillary number is increased, the drops evolve from a rounded contact line, develop an increasingly pointed corner as the trailing edge, then a cusp which desposits smaller drops. Extrand (1995) used a sideview camera to study contact angle hysteresis, drop shape, and drop retention on a tiltable plane. McAlister, et al. (2005) used a similar approach to investigate the break-off of drops and rivulets forced by airflow under varying gravity conditions. The experiments by Milne (2009) also used a sideview camera for drop measurements.

Undoubtedly, top and side views can provide meaningful qualitative results. As Milne (2009) showed, quantitative data collected from sideview images can be sufficient to produce correlations from drop runback thresholds. However, the quantitative results are a limiting factor for later analysis (as exhibited through Milne's use of the empirical factor, k) because the top and sideview technique lacks the ability to track the instantaneous fully three-dimensional shape. A sideview image only permits measurement of the contact angle at the leading and trailing drop edge. However, a full profile measurement is necessary for a rigorous analysis of the surface tension forces acting on the drop at its contact line. Detailed profile measurements also enable validation of drop stability theory and simulations.

Sessile drop methods and Wilhelmy balance measurements (Marmur, 1996) are often used to measure contact angles of specific fluid-fluid-solid interfaces. Sessile drop methods use sideview images to measure the contact angle of an axisymmetric drop, usually through computer image analysis (Stalder et al., 2006). The Wilhemly method measures the force exerted on a thin plate inserted into the liquid and relates this to the contact angle of the system. These can provide accurate contact angle data but do not enable measurement of dynamic drop behavior or variable contact

angles on rough surfaces.

Work by Rio, et al. (2005) used a laser line-scanning technique to measure line profiles of drops sliding down inclined glass plates. The technique was later adapted to measure slices perpendicular to the motion of travel of a drop, allowing for a full reconstruction of the drop shape as it passed over the measurement location. This method, however, requires the drop to be in motion and assumes the drop maintains a constant shape and velocity as it slides. Therefore, it is not suitable for the stability problem.

C. Motivation and Objectives

The preceding review of relevant literature concerning drop stability reveals notable room for improvement of drop stability knowledge through the application of a more sophisticated measurement technique. Experimental data is essential to achieve a better understanding of the characteristics of the stability limit and for validation of theory and models previously applied to the problem. A technique capable of this has been developed by the author and is implemented in the drop stability experiments detailed in this dissertation. This technique provides instantaneous, non-intrusive, full 3D profile measurements of drops on rough surfaces. It is thus applicable to studying the stability problem in situations of common engineering interest.

An improved understanding of drop stability requires more complete data about how the contact-line shape and contact angles evolve under wind forcing. Thus far, no experiments have been performed in a manner providing comprehensive data on the evolution of the contact line and contact angle distribution as a drop is brought from rest to critical forcing conditions. Observation of the contact line, contact angle distribution and drop profile will provide insight into the balance of forces acting

on the drop and elucidate which parameters are most important to drop stability, enabling a fuller understanding of drop stability limits on rough surfaces.

The main goal of this dissertation is to provide a new characterization of the fundamental nature of the drop stability problem through the application of the drop profile measurement technique. Specifically, the following questions are addressed:

1. What is the critical force that causes a drop to run back along a surface and how does it depend on Bond number and the relative contributions of gravity and wind forcing?
2. How do the contact line and contact angle distribution evolve as increased forcing is applied?
3. What is the shape of a wind-forced drop at the runback threshold?

To answer these questions, the specific research objectives are to

1. measure the evolution of the drop profile, contact line shape, and contact angles as gravity and wind forcing are increased and
2. identify stability limits in terms of Weber number as functions of Bond number and surface inclination.

To fulfill these objectives, an experimental facility capable of applying forcing to drops has been designed and built. Drops are measured by a unique method capable of reconstructing the full three-dimensional drop profile. Using the facility and measurement technique, the stability limits are tested over a range of parameters, with particular care taken to observe the behavior of the contact line and contact angle as the drop adjusts its position to find a stable configuration until it is no longer able to do so and runs downstream.

The dissertation is organized as follows. Chapter II presents a thorough description of both the experimental setup and procedures. This first entails a presentation

of the design and construction of the experimental facility used to conduct these drop experiments. Then, the technique implemented to measure full three-dimensional profiles of wind-forced drops is described, including the hardware setup and analysis algorithms. Chapter III details the experimental results obtained through the implementation of these tools. Stability limits and critical forcing levels are presented for each test configuration. Chapter IV describes the observed evolution of drop shapes with increased forcing, with care taken to observe similarities and differences between the behavior in different parameter regimes. Where applicable, these results are compared to those of theory, simulation and experiment in the literature. Chapter V presents conclusions and outlines directions for future work.

CHAPTER II

EXPERIMENTAL SETUP AND PROCEDURES

A. Wind Tunnel

1. Design

To explore the combination of gravity and wind-forcing necessitates a wind tunnel capable of rotating up to 90° while maintaining well-aligned top and sideview optical access necessary for drop shape and motion observations. This precludes the use of any existing wind tunnel facilities; a new wind tunnel is built specifically for the purposes of these experiments. The tunnel must also allow for different floor pieces so that different materials and roughnesses can be tested. The following sections will present design guidelines, building and implementation, and flow measurements performed in the wind tunnel.

Keeping the intended experiments in mind, a list of experimental facility needs includes the following. The wind tunnel must provide forcing of drops with combined gravity and wind through a mechanism that will tilt the test section in a downwind direction. (The reasons for this combined forcing are explained later.) To properly conduct experimental testing and validation of previous analytical and numerical studies of drop stability to wind forcing, the rig must be capable of providing similar conditions to the range of non-dimensional parameters used in the literature. Here is presented a short summary of some literature relevant to setting these parameters for a wind tunnel, then a discussion is given of the design requirements of a wind tunnel to match the appropriate parameters.

Work by Dussan (1987) found a critical shear rate for drops with small advancing

contact angle and small contact angle hysteresis to be

$$\frac{dU}{dy} = \frac{0.452\gamma\theta_A^{4/3}(\theta_A - \theta_R)}{V^{1/3}\mu_s}, \tag{2.1}$$

where μ_s is the viscosity of the moving fluid and γ is the surface tension of the drop fluid. Using the air/water system and contact angles restricted by the limits of the asymptotic theory, this equation produces values of dU/dy with magnitude $\mathcal{O}(1$ m/s/mm). Later, Dimitrakopoulos (2007) conducted numerical simulations in a similar regime as Dussan's theoretical work and found that the applicability of lubrication models such as Dussan's is extremely limited. It is more practical to consider higher Re drops whose stability limit can be best expressed as a critical Weber number.

Durbin (1988) conducted a 2D, high Reynolds number, free-streamline study of drop stability for which the drop height was greater than boundary layer thickness, separation was strong, and pressure drag was the dominant dislodging force. Weber number was found to have a maximum critical value of about five for configurations with maximum contact angle hysteresis. Again, this study included the assumption that drop slope is small and can be approximated by the surface normal. More recently, Ding and Spelt (2008) performed 3D numerical simulations of drops in density- and viscosity-matched shear flow at Reynolds numbers up to 80 and Weber numbers up to four.

Thus, in an attempt to approximate the creeping flow conditions of the most advanced drop stability simulations to date, these experiments will seek to match the attached flow, low/moderate Reynolds number conditions of Dussan, Ding, and Dimitrakopoulos. Given the ease and necessity of using the water/air combination for drop and moving fluid, it is chosen as the working fluid combination, unfortunately removing the ability to control viscosity and density ratios in the simple manner of

a numerical simulation. Therefore, it will be near impossible to reach the stability limit of drops in the shear flow regime of Stokes flow given the density and viscosity ratios of air and water. Instead, the focus will be on higher Weber numbers suitable for pressure-driven drops.

To closely approximate the steady flow regime studied in the literature, it must be ensured that no unsteady flow separation occurs in the wake of the drop. For laminar boundary layer flow over hemisphere roughness elements, Acarlar (1987) found regular shedding (in the form of distinct hairpin vortices) to begin at $Re_k \approx 120$. This Reynolds number is based on the hemisphere height and the associated velocity at that distance from the plate. Therefore, these experiments will aim to stay in the range $Re_k < 100$ in order to maintain steady regular flow over the drops.

The adhesion force at the stability limit for a drop on a surface tilted at angle α is

$$F_{\text{adh}} = mg \sin \alpha_{\text{crit}}. \tag{2.2}$$

Tilting the surface at an angle less than the critical tilt angle, α_{crit}, at which the drop runs and combining that sub-critical gravity forcing with airflow, a simple representation of the force balance at the stability limit is

$$F_{\text{adh}} = mg \sin \alpha + \frac{1}{2} \rho U^2 C_D A_{\text{frontal}} \tag{2.3}$$

where the drag force is crudely approximated as the pressure force on the projected frontal surface area of the drop using the velocity at the tip of the drop. Tilting to 90% of the critical angle, and using the data from Bikerman (1950) for the tilting stability limit of water drops of volumes from 50 to 400 μL, a calculation can be made of the velocity required to provide sufficient air forcing to dislodge sub-critically tilted drops. Bikerman lists equilibrium contact angles for water drops on stainless steel surfaces of different roughness. (Bikerman used 18-8 stainless steel

with $h_{\text{rms}} = 3.1, 1.0, 0.40, 0.10, 0.045$, and 0.030 μm.) Using the assumption that the drops take a spherical cap shape, contact angles from Bikerman and the known volume can be used to calculate projected frontal surface area of the drops. Then, the drop tip velocity required to dislodge the drops is

$$U^2 = \frac{2F_{\text{drag}}}{\rho A_{\text{frontal}} C_D}. \tag{2.4}$$

Including the full range of drop size on all six surfaces tested by Bikerman, tip velocities fall within the range of 1.3 to 2.3 m/s for drops tilted to 90% of the critical tilt angle. To estimate the wind tunnel speed needed to achieve these velocities at the drop heights, this data is combined with the fully developed parabolic velocity profile of the designed wind tunnel. In that case, critical forcing is achieved at max velocities of 1.9 to 7.4 m/s. Using instead 1/2 of the drop height as the reference location to account for the fact the drop is situated in a shear flow, the centerline velocity range for wind tunnel speeds is 3.3 to 14.1 m/s. Naturally, the largest drops are most unstable to both gravity and airflow forcing.

Alternatively, the shear force can be used to calculate the stability limit, producing the following force balance:

$$F_{\text{adh}} = mg \sin \alpha + \tau_{\text{wall}} A_{\text{contact}}. \tag{2.5}$$

where the drag force on the drop due to the airflow is approximated as the wall shear times the contact area of the drop. Using this approximation for the dislodging force, the same Bikerman drops become unstable at velocities of $U_\infty = 1.0$ to 10.6 m/s. Again, this is based on the parabolic velocity profile; for velocity profiles with thinner boundary layers, the maximum wind tunnel velocity would be lower.

Removing the force of gravity due to tilting and considering the stability of the drop to only airflow, the force balance is simply between adhesion and aerodynamic

pressure and shear. With the same Bikerman drop characteristics, the drop stability limit fell within the range of tip velocities between 4.2 and 8.1 m/s, while corresponding Reynolds numbers ranged from 1000 to 2200 and Weber numbers from 1.7 to 3.3. For a reference location of 1/2 the drop height, this necessitates a wind tunnel velocity range of 10.6 to 49.0 m/s. It is likely that a small wind tunnel would provide a slug flow with thin boundary layers rather than fully developed Poiseulle flow. This is preferable because the maximum wind tunnel velocity is not so high as for Poiseulle flow.

2. Implementation

To implement a rotating tunnel that could provide this flow velocity, a frame was constructed of T-slotted framing as shown in the schematic in Fig. 2. The frame provides a stable base for the tilting apparatus and is isolated from building vibrations through vibration isolator feet. The frame is primarily constructed of triangular sections to provide a rigid platform. Rotary bearings are attached to the top of both sides of the frame, to which the tiltable platform is connected. Since the wind tunnel test section is elevated above the tiltable platform base, the platform is mounted at a level below the bearing level such that the axis of rotation is aligned with the substrate surface. Thus, the drop experiences minimal translation as the inclination angle increases. The tilt platform also has mounting holes to which the cameras and wind tunnel are rigidly mounted.

At one end of the tilt platform, the rotation shaft is connected to a stepper motor through a $20:1$ worm gear. The stepper motor is a Silverpak 17C from Lin Engineering and has $51,200$ steps per revolution. Combined with the $20:1$ gear, steps of 0.00035° are possible.

The wind tunnel is designed according to typical wind tunnel paradigms (Barlow,

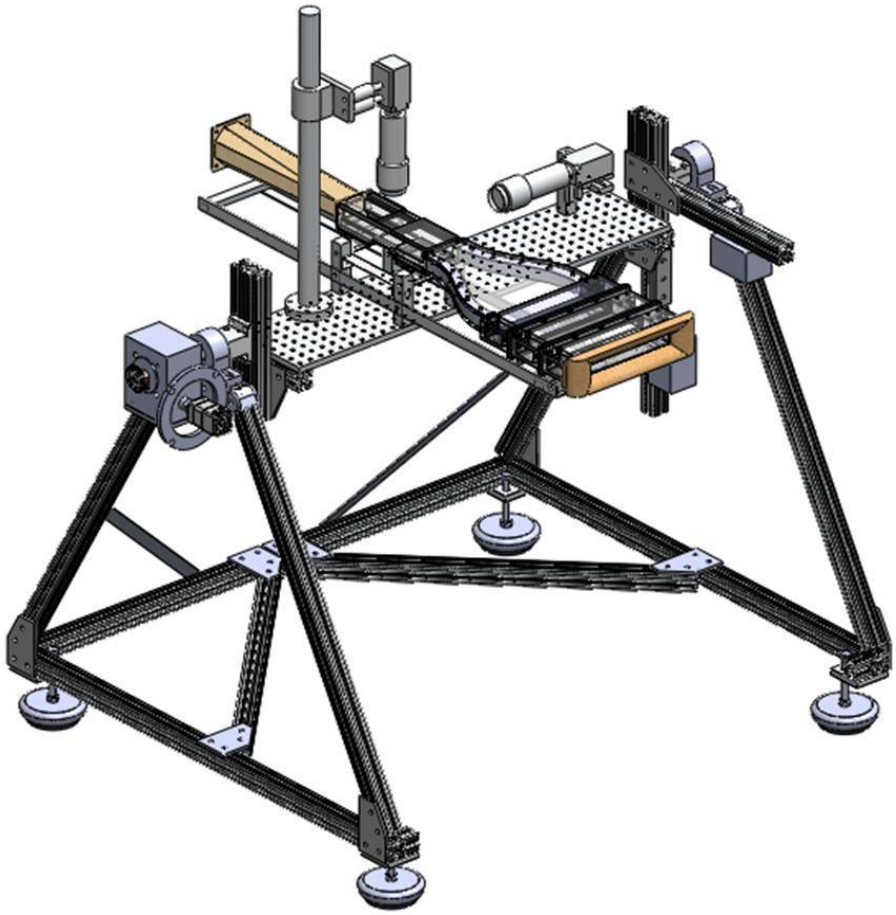

Fig. 2 : Wind tunnel and experimental rig for drop stability experiments

1999). A schematic is shown in Fig. 2. It is an open return wind tunnel that draws in ambient room air and exhausts to the same. The inlet has a cross section of 1 inch tall by eight inches wide and begins with an inlet fairing to promote smooth entry of airflow into the tunnel. The air passes immediately through a paper honeycomb with a length-to-diamter ratio of four. Next, the flow passes through two screens with 30 wires per inch and 65% open area. The screens are separated by 3.5 in. The screens break up any large scale turbulence into smaller features that dissipate faster, before entering the test section. Finally, the flow passes through a 10 in long contraction which reduces the tunnel width from 8 in to 2 in. The contraction profile is a fifth-order polynomial with zero slope and curvature at both ends.

The flow then enters the test section, which is 1 in tall by 2 in wide. The test section walls are made of machined acrylic. Halfway along the 10 in test section length is a slot where interchangeable surface samples fit into the tunnel floor. Above the surface samples, the roof of the test section is a 1/8 in thick square of high quality BK-7 glass to provide optical access for the topview camera.

Following the test section, the flow passes through a diffuser with a half angle of 5.5° to prevent separation and any flow unsteadiness that could propagate upstream into the test section. At the end of the diffuser is an 80 mm fan which produces the pressure drop to drive flow through the tunnel. The fan is a Delta axial vaned fan model PFC0812DE-SP04 and runs on a 12 V supply. Speed control of the fan is achieved through a pulse width modulation (PWM) input.

In order to compare experimental results to theory, computation, and other experiments in the literature, it is important to know the characteristics of the flow to which the drops are exposed. To that end, a series of hotwire anemometer boundary layer scans were carried out to measure the profile of the boundary layer on the floor of the tunnel in the location where the drops are placed.

The wind tunnel is designed to provide critical forcing to drops at low flow speeds. At low flow speeds, natural convection from the hotwire becomes important, so its calibration must account for this effect. Therefore, a low speed hotwire calibration used by Johansson and Alfredsson (1982) was implemented here as in Eq. 2.6, where E is the hotwire voltage, E_0 is the hotwire voltage with zero flow velocity, and A, B and n are the calibration constants.

$$U = A\left(E^2 - E_0^2\right)^n + B\left(E - E_0\right)^{1/2} \tag{2.6}$$

Hotwire calibrations were performed relative to a pitot tube measurement of the dynamic pressure. An MKS Baratron 698A differential pressure transducer measured the differential pressure between the dynamic and static pressure in the test section. The pressure uncertainty associated with this transducer is 0.05% of the measurement. An A.A. Labs AN-1003 anemometer system was used to power the hotwires and send the signal to a National Instruments USB-6211 data acquisition board.

To perform a hotwire calibration, the wind tunnel was run over a range of velocities from 0.5 to 15 m/s. At each speed, the hotwire voltages and pitot tube velocities are recorded. The calibration constants A, B, and n are then calculated using the Levenberg–Marquadt nonlinear least squares algorithm in Labview. A typical result of this calibration procedure is shown in Fig. 3. The hotwires were found to have a frequency response of around 17 kHz, sufficiently high for these boundary layer scans.

A hotwire holder and traverse system was constructed to translate the hotwire vertically toward the wind tunnel floor. Its position was measured with a dial indicator with resolution of 0.0005 in. The hotwire was traversed manually, with a sideview camera providing position feedback. Boundary layer profiles were recorded at three spanwise locations: the centerline of the test section and 1/2 in on either side. Ten seconds of data were recorded at 10 kHz. Since the dial indicator specifies only relative

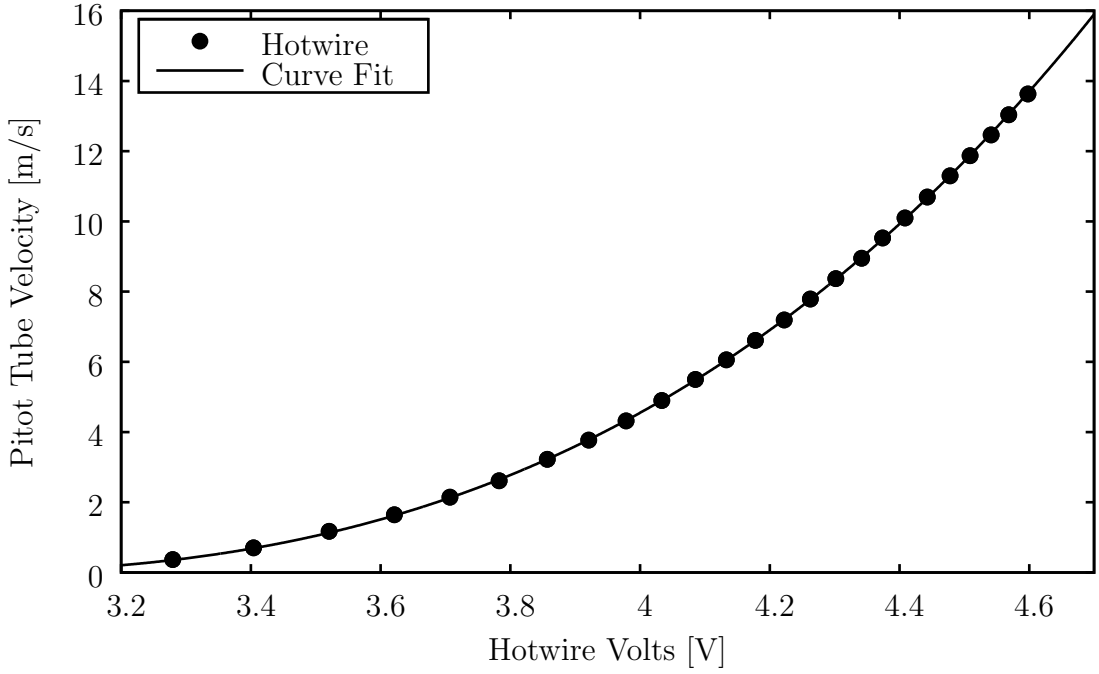

Fig. 3 : A typical set of hotwire anemometer calibration data

position between hotwire measurements and not absolute position relative to the test section floor, it is necessary to adjust each position to the absolute reference frame. To do this, hotwire measurements are recorded to within the linear profile portion of the boundary layer and a curve fit is made to extrapolate the wall position. A typical boundary layer velocity profile is shown in Fig. 4. It is evident that the test duct has not yet achieved a fully developed channel flow profile, but rather has a uniform velocity over much of the test section with the shear layer confined to several millimeters above the wall.

Ideally, the boundary layer will be self-similar at all tunnel speeds. This permits fitting the profile with a single analytical function for easy documentation of the flow. To do this, y is normalized by the boundary layer displacement thickness, δ^*, which is calculated as an integral of $u(y)$ from the surface to the freestream (Schlichting, 2000). Momentum thickness is computed in the same fashion. The displacement thickness,

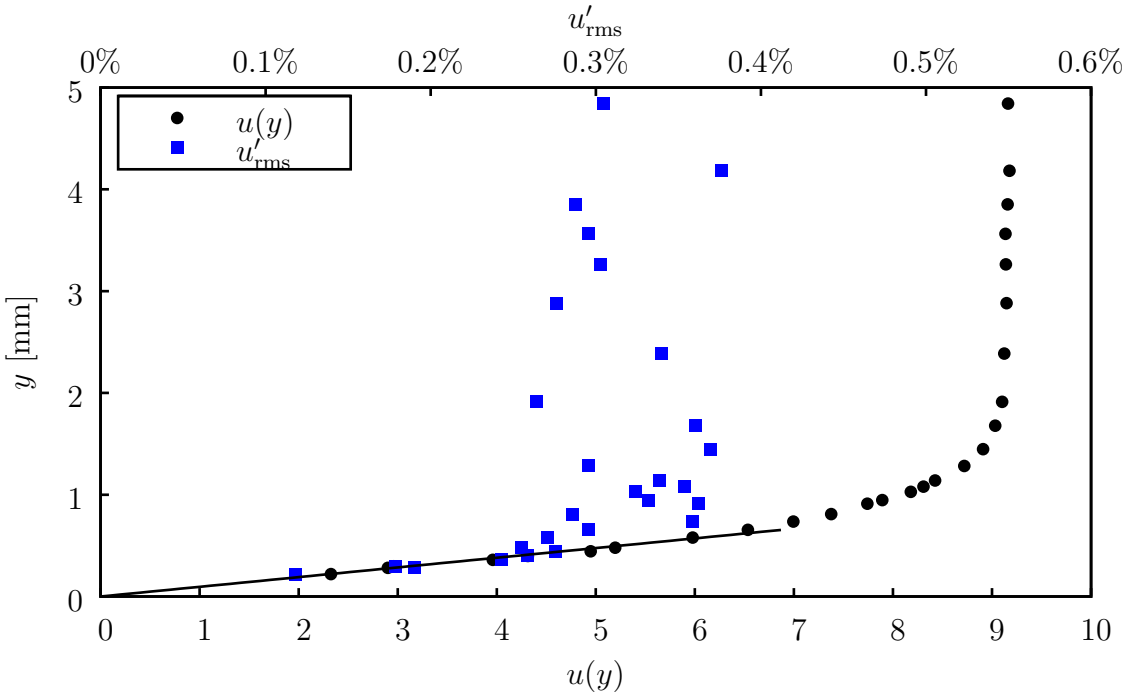

Fig. 4 : A typical boundary layer profile

momentum thickness, and shape factor, $H = \delta^*/\Theta$ for the various test conditions are shown in Fig. 5.

Normalizing y by δ^* and u by U_∞ for each test condition, the data collapse to a self-similar curve, shown in Fig. 6. Through a trial-and-error approach, the equation

$$f\left(\frac{y}{\delta^*}\right) = 1 - \exp\left[-a\left(\frac{y}{\delta^*}\right)^b\right] \tag{2.7}$$

is found to sufficiently fit the data by application of a non-linear least squares curve fit to find the constants $a = 0.89$ and $b = 1.37$. Finally, a correlation for δ^* as a function of U_∞ is required to complete a full characterization of the wind tunnel flow. Fitting the function $\delta^* = cU_\infty^{-d}$ to the data produces the constants $c = 1.72 \pm 0.64$ mm(m/s)$^{1/2}$ and $d = -0.52 \pm 0.17$.

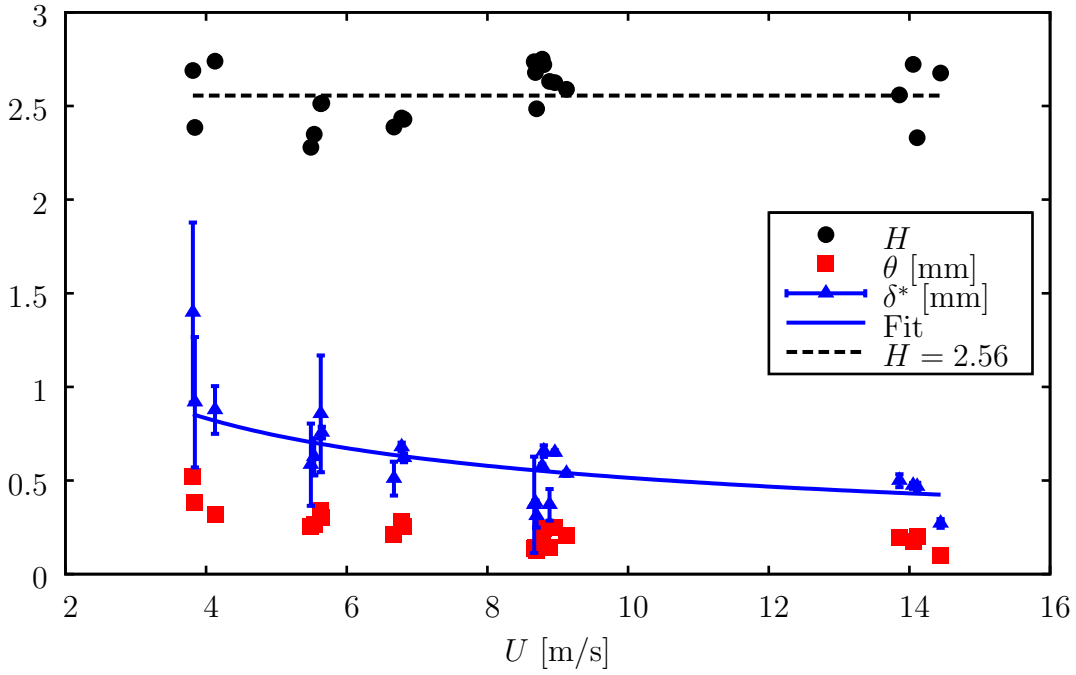

Fig. 5 : Displacement thickness, momentum thickness and shape factor for various wind tunnel speeds

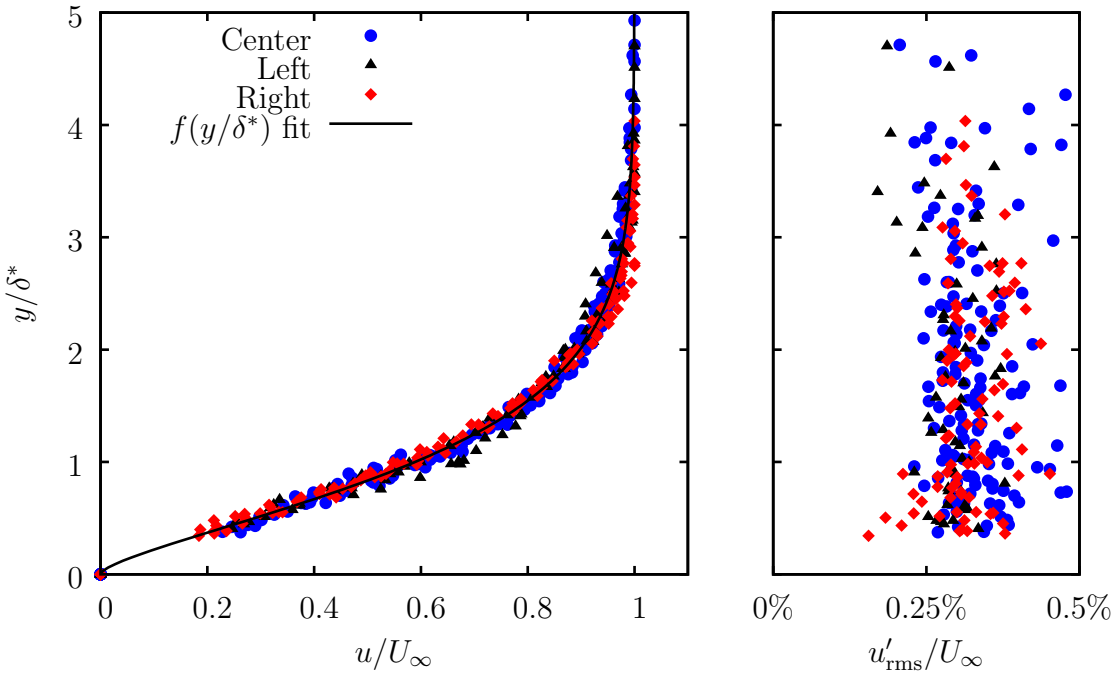

Fig. 6 : Non-dimensional boundary layer profiles and turbulence intensity profiles

Also of interest is the turbulence intensity in the test section. Ideally the flow will be laminar with very low velocity fluctuations. Since the hotwire has only measured the u-component of velocity, this is used as an analog for turbulence intensity. As seen in Fig. 6, u'_{rms} is in the range of about 0.2 to 0.4% of the freestream speed, an acceptable level for these experiments.

The rough surface sample used in these experiments is a 2 in long (in the streamwise direction) by 1 in wide piece of sandblasted aluminum. A Mitutoyo Surftest SJ-400 roughness tester was used to measure the roughness of the sample. The diamond-tipped stylus is a 60° cone with a 2 μm tip radius. Eight different traces were made in different directions along the surface, with the resulting parameters averaged and reported here. The mean deviation of the roughness from the nominal surface profile is $R_A = 3.26$ μm. $R_y = 20.9$ is the height of the tallest peak minus the depth of the lowest valley; $R_q = 4.04$ is the root-mean-square of the surface profile.

B. Measurement Techniques

1. Forcing Measurements

Two macroscopic forces are applied to drops during experiments, gravity and wind. Each image of a drop is captured at a particular level of forcing, the amount of which must be measured accurately as a critical part of the experimental data set.

The flow velocity in the test section is monitored during drop experiments by measuring the pressure drop across the wind tunnel contraction. Two pressure ports are located in sections of straight flow 0.25 in before and after the contraction. The pressure difference is measured with an MKS Baratron Type 226A differential capacitive manometer. The unit is factory calibrated to a measurement error of 0.3% of the reading. The Δp values were correlated to hotwire measurements of the freestream speed in the test section and are used to set the tunnel speed. A proportional gain feedback loop uses the Δp measurements as velocity feedback, while tunnel speed is controlled by the duty cycle of a pulse width modulated signal to the wind tunnel fan.

The inclination angle of the substrate is measured through a rotary encoder connected to the shaft that drives the rotation stage. The encoder is a U.S. Digital model EM1 transmissive optical encoder. The rotary disk is model DISK-2-2500-500-IE and has 2500 counts per revolution. Combined with the quadrature capabilities of the encoder module, an angular resolution of 0.036° is achieved. A feedback loop was programmed to monitor the tilt angle and ensure it is within tolerance of the commanded angle.

2. Drop Measurements

The drop measurement method employed in this research was developed in recent years by the author and coworkers (Schmucker and White, 2007, Schmucker

et al., 2012). The technique has been developed for measuring three-dimensional instantaneous drop profiles on rough surfaces. The rough surface is illuminated using a laser (or other high intensity light source) and images are captured of the resulting speckle pattern with and without the drop in place. The analysis consists of finding the contact line, measuring the deformation of the speckle field caused by refraction of light at the drop surface, then reconstructing the drop using simulated annealing optimization to find the drop shape whose shift vector field best matches the one measured. An error analysis of the technique was performed using a Monte Carlo technique and comparisons to sideview drop images for a large sample of drops. Mean contact angle measurement error was found to be $-1.6°$ with a 1-σ error bound of $-6.9°, +2.0°$. This section provides details of the measurement technique for reference.

Propagation of light rays from the surface to the camera is illustrated in Fig. 7 (with the scale of the surface roughness exaggerated). When the surface is dry, a small cone of rays represented by R_A leaves point P and forms an image on the camera sensor. With a drop in place, however, the light follows the path along R_B, refracting at the drop interface according to Snell's Law: $n_{\text{air}} \sin\theta_1 = n_{\text{water}} \sin\theta_2$, where n_{air} and n_{water} are the refractive indices of air and water, respectively. The refraction produces a change in the light ray's path so that the speckle intensity characteristic of point P appears to shift in the image plane by the distance s. This shift occurs in the direction of decreasing height, y, of the drop interface. The shift distance is given by $s = y \tan(\theta_1 - \theta_2)$.

In order to perform full reconstruction of the drop profile, the surface gradient, $\nabla y = (\partial y/\partial x, \partial y/\partial z)$, is required rather than the surface angle, θ_1. The angle θ_1 is expressed in terms of the surface gradient by $\theta_1 = -\tan^{-1}(|\nabla y|)$. Combining this

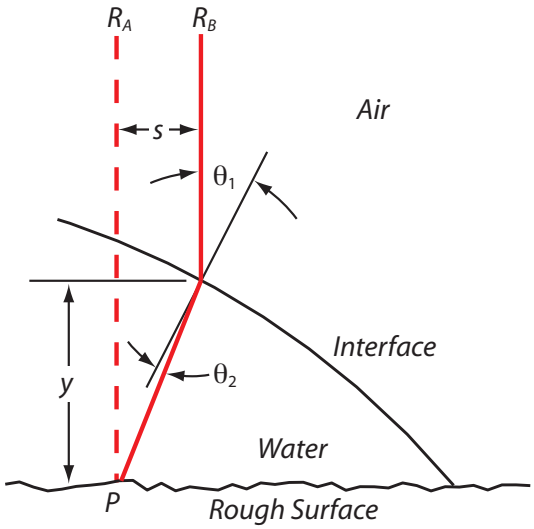

Fig. 7 : Ray tracing of light propagation and refraction at drop interface

relation and Snell's Law with the equation for speckle shift distance yields

$$\vec{s} = -y \tan\left[\tan^{-1}\left(|\nabla y|\right) - \sin^{-1}\left[\frac{n_{\text{air}}}{n_{\text{water}}} \sin\left(\tan^{-1}\left(|\nabla y|\right)\right)\right]\right] \frac{\nabla y}{|\nabla y|} \qquad (2.8)$$

where $\vec{s}$ is a two-dimensional vector of speckle shifts in the x and z surface coordinates. A measurement of the speckle shift vector field, $\vec{s}(x, z)$, within the drop domain can then be used to solve the right-hand side of Eq. 2.8 for the drop profile $y(x, z)$. Measurement of the speckle shift vectors is performed by a cross-correlation operation performed between the control and drop image. In simple terms, a small subregion of the control image is swept through the drop image to find the location where its speckle pattern best matches that seen through the drop.

The camera is a Pixelink PL-B741U with a global shutter and a resolution of 1280×1024 pixels. An 18–108 mm zoom lens is fixed to it and provides a field of view range acceptable for various drop sizes. The camera and lens are aligned with the optical axis perpendicular to the test surface. A control image is first captured of the dry illuminated surface. Any number of drop images are captured during an experiment. An example control and drop image are shown in Fig. 8.

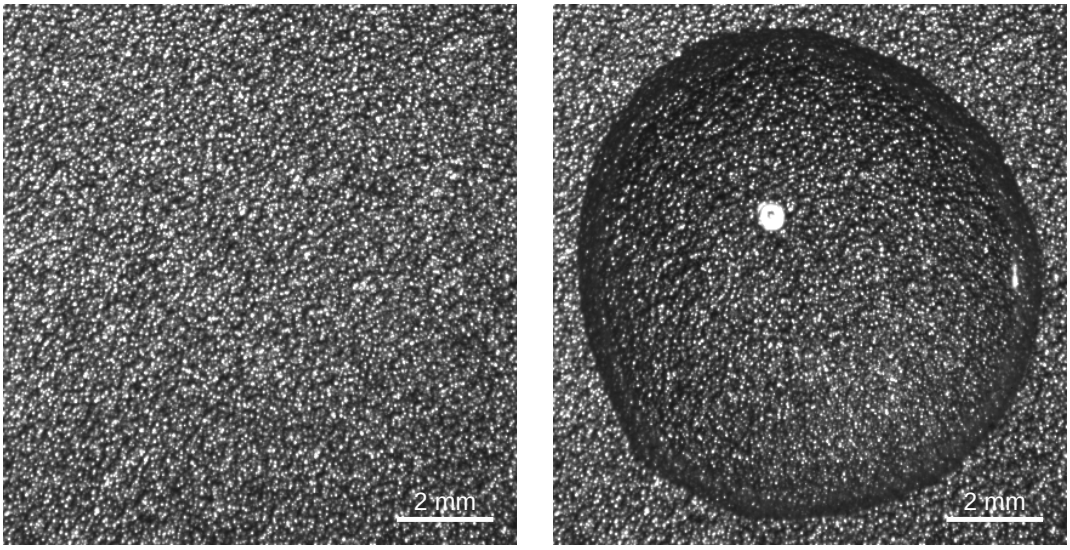

(a) Control image (b) Drop image

Fig. 8 : Control and drop image pair

The first step of the image analysis algorithm for reconstructing a drop profile from a control-drop image pair is to determine the location of the contact line. Common methods for the detection of image edges involve filtering with derivative kernels. In this case, however, the speckled nature of the drop images precludes application of this technique. Instead, the control image is subtracted from the drop image. Since speckles outside the drop area do not shift between images, this subtraction produces an area outside the drop with a nearly zero pixel value. (This assumes most pixels within the drop area have moved appreciably; sometimes this is not the case and contact line measurement proves difficult.) The subtracted pixel values within the drop are irrelevant; it is merely their large magnitude relative to the values outside the drop that is useful.

The intensity differences are rectified and a threshold routine applied to convert to binary values (inside or outside the drop). This initially detected contact line can be somewhat jagged—a clearly nonphysical solution. Accordingly, the process is repeated

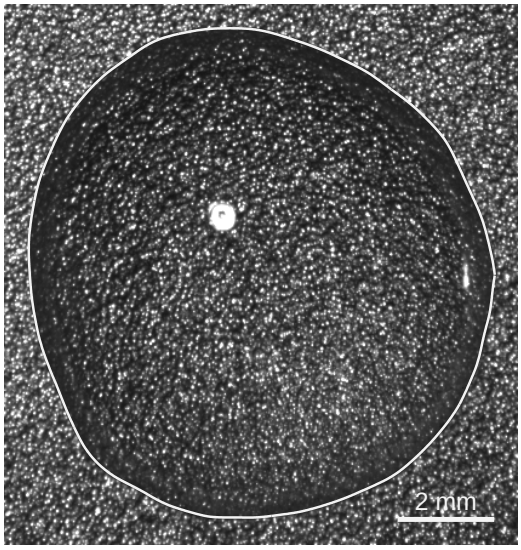

Fig. 9 : Drop edge detection

after the image cross-correlation (detailed in the following paragraphs) measures the global shift between the control and drop specklegrams, allowing for better alignment of the control and drop images. Finally, the drop radius as a function of angular position is filtered by an unweighted central moving average filter with window size five percent of the contact line length to produce a final smooth contact line.

The speckle shift vector field is measured using cross correlation between the control and drop images. Square subregions are taken from the drop image; for each subregion, $I^{x,z}_{\text{drop}}$, a cross-correlation is calculated between the subregion of the drop specklegram and shifted subregions of the control image, $I_{\text{cont.}}(x-a, z-b)$, as

$$\zeta(a,b) = \frac{\sum_{x,z}\left[I_{\text{drop}}(x,z) - \left\langle I^{a,b}_{\text{drop}}\right\rangle\right]\left[I_{\text{cont.}}(x-a,z-b) - \langle I_{\text{cont.}}\rangle\right]}{\left\{\sum_{x,z}\left[I_{\text{drop}}(x,z) - \left\langle I^{a,b}_{\text{drop}}\right\rangle\right]^2 \sum_{x,z}\left[I_{\text{cont.}}(x-a,z-b) - \langle I_{\text{cont.}}\rangle\right]^2\right\}^{1/2}}. \tag{2.9}$$

Mean subregion intensities (indicated by angle brackets) are subtracted to give a matrix of correlation values, $\zeta(a,b)$, in the range $[-1,1]$. It is assumed that the highest ζ indicates the shifted position of the subregion and this gives the shift vector

$\vec{s}$. Sometimes, inherent measurement uncertainty confounds the correlation and the algorithm returns grossly incorrect results. These outlier vectors complicate the later reconstruction process. A scheme is implemented to identify these outlier vectors.

The components of $\vec{s}$, as calculated by Eq. 2.9, take integer values when expressed in the pixel coordinate system. The correlation peak is most often broadened over a range of more than one pixel, and interpolation is used to determine the sub-pixel displacement. Using the standard approximation that the correlation peak has a nearly Gaussian shape, the sub-pixel displacement is calculated using a Gaussian peak fit (Westerweel, 1993, 1997) where sub-pixel displacements, δ, are given by

$$\delta = \frac{\ln \zeta_{-1} - \ln \zeta_{+1}}{2\left(\ln \zeta_{-1} - 2\ln \zeta_0 + \ln \zeta_{+1}\right)}. \tag{2.10}$$

This estimator takes into account the values of the cross correlation matrix at the peak location, ζ_0, along with cross correlation scores on either side of the peak, ζ_{-1} and ζ_{+1}. The same equation is used for both the x and z directions. Proper shift vector measurement involves an intricate interplay between a proper selection of subregion size, the resulting shift vector uncertainty, and the maximum vector magnitude for which the algorithm searches. The issues involved in a suitable shift vector measurement are discussed by Schmucker (2012).

After a satisfactory measurement of the speckle shift vectors and outlier identification (an example of which is shown in Fig. 10) the reconstruction process must solve the right hand side of Eq. 2.8. The approach chosen for reconstructing the drop seeks to minimize the difference between the measured shift vector field and the shift vector field of the reconstructed drop profile. Thus, reconstruction is cast as an optimization problem in which the shape of the reconstructed drop must be adjusted to find the best match with the measured speckle shift vector field. Therefore, a method for representing the reconstructed drop profile must be selected.

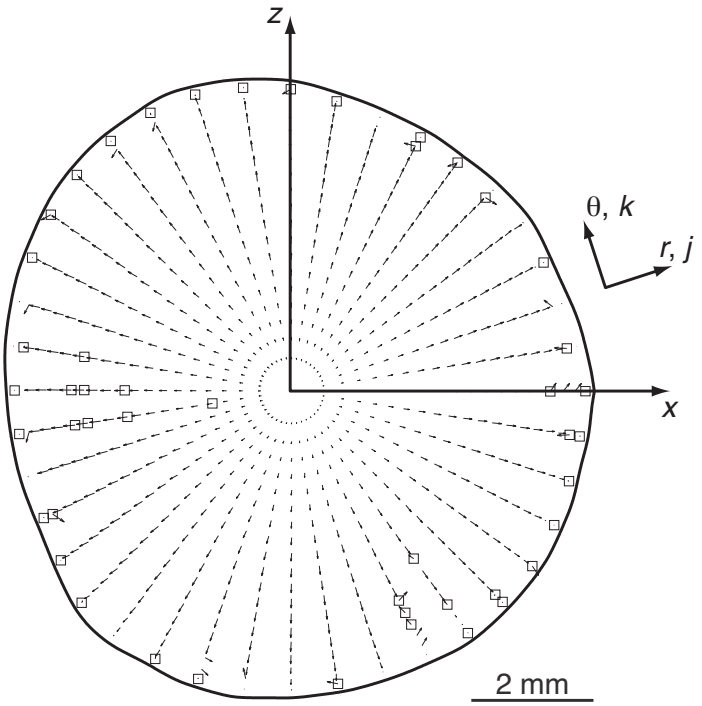

Fig. 10 : Speckle shift vector field measured by image cross-correlation at elliptic grid nodes. Identified outliers are marked by squares

The method chosen involves the use of a Fourier series for the circumferential direction, owing to its periodicity and general utility. The radial direction is represented by a Bessel series. The Fourier and Bessel series provide a simple and workable basis for reconstruction of drop shapes produced by challenging experimental conditions. Besides automatically enforcing the boundary (zero height at contact line) and smoothness conditions, this approach dramatically reduces the dimension of the parameter optimization problem. However, this approach requires remapping the contact line to the unit circle because the contact line is not necessarily circular.

To map the drop footprint to the unit circle, an elliptic grid is constructed with the contact line as its perimeter. The radial lines of the unit circle grid contain J grid points ranging from the center at the discrete radial index $j = 0$ to the contact line at $j = J - 1$. There are K radial lines specified by the circumferential index, k. The

nodes of the remapped drop grid are the points at which the drop height is specified by the reconstruction process. These points are nodes of an elliptic grid in physical space. The center point of the grid can be chosen as either the centroid of the surface area covered by the drop or the point of maximum drop height. At the contact line, the elliptic grid is constrained so the radial grid lines are perpendicular to the contact line. This permits easy calculation of the contact angle about the drop perimeter. (See Schmucker (2007) and Hoffman and Chiang (2000) for details of the elliptic grid equations and solution procedure.) Finally, a measurement of the speckle shift is made at each node of the elliptic grid using a subregion centered at the (x, z) locations of the grid nodes.

In addition to the Bessel–Fourier series, a spherical cap mode is also a part of the sum representing the drop shape. A spherical cap is specified by contact line radius, a, height, h, and sphere radius, R. Since the drop has been mapped to the unit circle ($a = 1$) and the relation $R = (a^2 + h^2)/2h$ holds, a value for h specifies the mode shape. The spherical cap mode is scaled by h to give it unit height. The spherical cap mode is the first term of the right-hand side Eq. 2.11. The form of the Bessel–Fourier series is seen in the second term of the right-hand side Eq. 2.11, where $A_{m,n}$ is the complex amplitude and $\alpha_{m,n}$ is the n^{th} real root of the m^{th}-order Bessel function of the first kind, J_m. (J_m is not to be confused with J, the total number of radial points.) The Bessel-Fourier series profile is specified by a set of coefficients $A_{m,n}$ for $m = -M \ldots M$ and $n = 1 \ldots N$. Bessel functions of negative order are related to positive order by $J_{-m} = (-1)^m J_m$. So for y to be real, it is required that $A_{-m,n} = (-1)^m \overline{A}_{m,n}$. Combining these expressions gives $A_{-m,n} J_{-m} = \overline{A}_{m,n} J_m$.

Thus, the set of coefficients A_{sc} and $A_{m,n}$ specify the reconstructed drop profile.

The drop height is expressed by the equation

$$y(j,k) = A_{\mathrm{sc}} \left(\frac{\sqrt{R^2 - (j/J)^2} - (R-h)}{h} \right) + \cdots$$
$$\cdots + \sum_{n=1}^{N} \sum_{m=-M}^{M} A_{m,n} J_m(\alpha_{m,n}\, j/(J-1)) \exp(2\pi i m k/K). \tag{2.11}$$

Calculation of the speckle shift vectors for a reconstructed drop profile using Eq. 2.8 requires both the height, y, and its gradient, $\nabla y = (\partial y/\partial x, \partial y/\partial z)$. The function y and its derivatives are calculated in the unit circle (r, θ) space and must be transformed into the (x, z) space for calculation of the shift vectors using the full equation for speckle shift (Eq. 2.8). The details of these calculations are given by Schmucker (2007) and Schmucker and White (2007).

To find the drop profile that best matches the measured speckle shift vector field, a minimization is performed of the error between the measured and reconstructed speckle shift vectors. The error is defined as the mean-squared error between the speckle shift vector components.

$$\chi^2 = \sum_{i=1}^{J \times K} \mu_i \left| \vec{s}_{i,\mathrm{meas.}} - \vec{s}_{i,\mathrm{reconst.}} \right|^2 \tag{2.12}$$

The error function can be modified to include further knowledge concerning the reconstruction. For example, each difference between reconstructed and measured vector is weighted by a factor μ_i indicating the confidence in and importance of the i^{th} shift vector. To weight by the confidence in each shift vector, χ_i^2 is multiplied by the correlation score C_i, the maximum of ζ in Eq. 2.9. Additionally, the value of χ^2 is weighted by the Jacobian determinant of the elliptic grid transformation to account for how much area a particular grid node represents in (x, z) space. A significant penalty (a penalty factor, ν, times the number of grid nodes with negative height, N_{negative}) is applied to the χ^2 error to prevent this simplex from choosing any drop

profiles with negative drop heights. Additionally, vectors identified as outliers have $\mu_i = 0$ so they make no contribution to χ^2.

Furthermore, the volume of a drop under test is also known and can be helpful when included in the definition of χ^2. To do this, an integration is performed over the contact area (CA) encompassed by the contact line of the drop. To significantly ease the computation of the integral, a change of variables is performed so the integration may be performed on the unit circle where the drop reconstruction is based on a Bessel–Fourier series. The transformation is completed through the use of the Jacobian determinant. The discrete nature of the reconstruction grid requires that the integration be performed numerically over the domain. In the interest of computation speed, this is performed through a simple sum as

$$\mathcal{V} = \iint_{CA} y(x,z)\,dx\,dz \approx \sum_{j,k} y(j,k) \left|\frac{\partial(x,z)}{\partial(j,k)}\right| \; dj\,dk. \tag{2.13}$$

This quick method for computing the volume of a drop reconstruction allows it to be used as a constraint in the reconstruction process.

Additionally, it was discovered that the reconstruction process sometimes produces results with nonphysical changes in surface curvature. To combat this, another constraint was added which attempts to miminize changes in surface curvature over the surface of the drop. The radius of curvature, R, is calculated using

$$\frac{1}{R} = \frac{1}{R_x} + \frac{1}{R_z} \tag{2.14}$$

where the curvatures in each direction are

$$R_x = \frac{\left(1 + \frac{\partial y}{\partial x}^2\right)^{3/2}}{\frac{\partial^2 y}{\partial x^2}} \qquad R_z = \frac{\left(1 + \frac{\partial y}{\partial z}^2\right)^{3/2}}{\frac{\partial^2 y}{\partial z^2}} \tag{2.15}$$

and $\partial^2 y/\partial x^2$ and $\partial^2 y/\partial z^2$ are calculated according the procedures of Appendix F in Hoffman and Chiang (2000). (Also note a correction to previous work: the second

term Eq. 3.25 of Schmucker (2007) and Eq. 7 of Schmucker and White (2007) should be positive, not negative.) The influence of this computation compares directly with the action of surface tension as it acts on the drop interface. Trial and error tests reveal the best results when the λ factors are adjusted to set the relative weight of the volume and curvature constraint terms are 5–10% of the shift vector sum.

$$\chi^2 = \nu N_{\text{negative}} + \sum_{i=1}^{J\times K} \mu_i \left|\vec{s}_{i,\text{meas.}} - \vec{s}_{i,\text{reconst.}}\right|^2 + \cdots$$
$$\cdots + \lambda_1 \left(\mathcal{V}_{\text{applied}} - \mathcal{V}_{\text{reconst.}}\right)^2 + \lambda_2 \sum_{i=1}^{J\times K} |\nabla R| \tag{2.16}$$

The reconstruction is a high-dimensional nonlinear optimization problem. The solution approach employed here is the downhill simplex method described by Press, et al. (1992). A simplex is a geometrical figure in L-dimensional space consisting of $L+1$ vertices and the lines and polygonal faces connecting them. For the drop profile optimization, each dimension represents a real-valued component of the complex Bessel–Fourier series coefficients, $A_{m,n}$. Each vertex of the simplex is a set of coefficients representing a potential drop profile.

Minimization of χ^2 using only the spherical cap mode produces a value for A_{sc}, which closely approximates the true height of the drop; this is used to set the initial configuration of the simplex. The origin of the simplex is placed at $A_{0,1} = A_{\text{sc}}/20$ with the other $L-1$ components set to zero. The other L vertices of the simplex are then set to be the origin plus $A_{\text{sc}}/20$ for each of the real parameters in turn. (From experience, it is found that the larger coefficients $A_{m,n}$ of the final result are usually on the order of 5% of A_{sc}.) The simplex is set so the Bessel–Fourier modes minimize the deviation of the true drop shape from the spherical cap fit. The algorithm evaluates χ^2 at each of the vertices. Based on the relative values, the simplex performs a series of contractions, expansions and reflections through the L-dimensional space, converging

toward the minimum of χ^2. A discussion of the reconstruction process and parameters can be found in previous work on the reconstruction technique (Schmucker et al., 2012, Schmucker and White, 2007)

Simplex optimization alone may become trapped in local minima of the χ^2 space. As a solution to this shortcoming, Press, et al. (1992) present an extension of the simplex method known as simulated annealing. Random numerical fluctuations proportional to a control parameter are added to simplex evaluations of χ^2. These fluctuations allow the simplex to jump out of local minima and continue in pursuit of the global minimum of χ^2. As the algorithm proceeds, the value of the control parameter is reduced to zero, the fluctations die out, and the algorithm reduces to exactly the downhill simplex method. The drop reconstruction is the best set of coefficients in the final simplex configuration.

C. Procedures

1. Initial Conditions

The first step of an experiment is to apply a drop to the wind tunnel floor roughness sample. The volume is measured by hand using a graduated Hamilton syringe of appropriate volume. For drops less than 100 μL in volume, the associated volume uncertainty is 1 μL. For drops larger than 100 μL, a larger syringe is used and the uncertainty increases to 2 μL.

Careful application of the drop to the surface is essential. Because the drop shedding and stability process is chaotic in nature, it is important to produce drops with similar configurations at the ininitiation of each experiment. Ideally, each drop would initially have a circular contact line. With some care and practice it becomes easier to apply drops with nearly circular contact lines. Nevertheless, some variability remains in experimental results.

Meiron, et al. (2004) performed a study that used the vertical vibration of drops on surfaces to force them into circular configurations. As mentioned previously, a drop on a rough surface generally exists in a local energy minimum, not the global minimum. This is one of the many metastable states allowable for the drop due to contact angle hysteresis. Addition of vibrational kinetic energy to the system introduces unsteadiness in the drop interface, sometimes creating instantaneous drop configurations for which the local contact angle is outside the range of θ_{r} and θ_{a}. Under those conditions, the contact line will locally either contract or expand, spurred on by the energy introduced by the vibrations. Over an appropriately long vibration time, the drop will tend to approach a circular contact line shape. Under that configuration the Wenzel equation applies, and Meiron found good agreement with the Wenzel equation.

Accordingly, another component of the test rig is a vibration stage connected to the wind tunnel floor. The mechanism which securely fastens the rough surface specimen in its position on the tunnel floor can be allowed to translate in a vertical direction. This stage is connected directly to a 6.5 in speaker powered by an amplifier. This hardware permits application of the Meiron technique to drops being tested here. However, the sandblasted aluminum surface sample used in these experiments has a very low receding contact angle. Consequently, oscillations of the drop interface rarely induce contraction of the drop contact line because the receding angle threshold is rarely surpassed. Therefore, much care is taken when applying drops in the interest of achieving initially circular contact lines. However, the caveat to this is that a perfectly circular drop placed on the surface will have an initial contact angle much closer to θ_{a} than to the equilibrium contact angle which results from the vibration process described above.

2. Near-Critical Tilt

An important component of the experimental results presented in the following chapter is a thorough examination of the stability limit, expressed as a flow speed (or Weber number) as a function of drop size (Bond number) and inclination angle. This provides insight into how drops are able to resist forcing by different mechanisms and the partitioning between those different forces. After a drop is applied, the wind tunnel is brought to a sub-critical inclination angle, rotating at a rate of one degree per second. The application of constant gravity forcing produces a commensurate decrease in the flow velocity required to dislodge the drop and likewise different characteristics of drop shape evolution.

CHAPTER III

STABILITY LIMITS

This chapter concerns the first question posed in Chapter I, Section C: "What is the critical force that causes a drop to run back along a surface and how does it depend on Bond number and the relative contributions of gravity and wind forcing?" The specific objective is to "identify stability limits in terms of Weber number as functions of Bond number and surface inclination." To address this, water drops spanning the range of 15 μL to 450 μL were placed on the rough aluminum surface sample with average surface roughness $R_A = 3.26$ μm. The tilt mechanism was then engaged to bring the wind tunnel to an inclination angle of 10°, 20°, or 30°. The wind tunnel speed was incrementally increased until the critical speed is surpassed and the drop began to run back along the surface, while images were captured at each set flow speed along the way.

The data for critical flow velocity as a function of drop volume and inclination angle are show in Fig. 11. This figure includes 235 separate drops and measurements conducted over 10 days. The four sets of data points correspond to the surface inclination angle, α. As the surface inclination increases, the downstream component of gravity acting on the drop increases, which reduces the critical flow velocity for destabilization. For small volumes, drops at each inclination angle follow the same trend with rapidly decreasing U_{crit} as the volume increases. As volume increases, the slope becomes less steep and different U_{crit} values for different surface slopes become apparent. Eventually, the curves drop to $U_{\text{crit}} = 0$ m/s for the $\alpha > 0°$ tests.

The $\alpha = 0°$ case imposes no gravity forcing, and thus represents the upper limit of critical flow velocity for a given drop volume (excluding negative inclination angles).

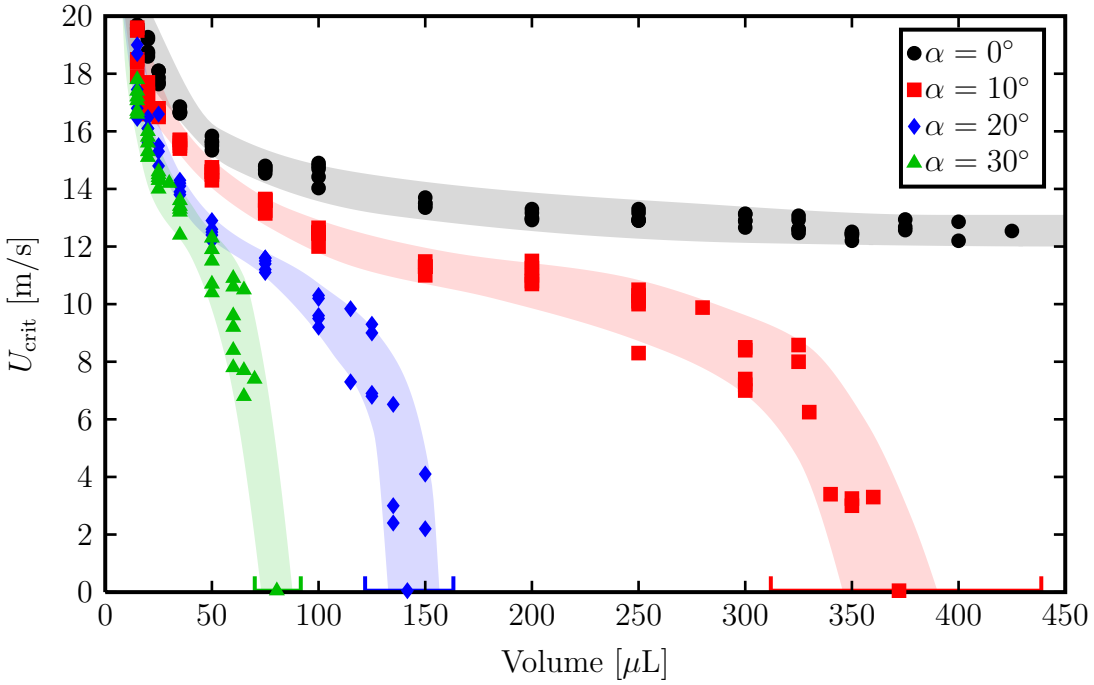

Fig. 11 : Drop runback thresholds shown as critical velocity as a function of drop volume for four surface inclination angles.

The critical flow velocity appears to asymptotically approach a constant value as drop volume increases. Beyond the volume range of the plot, gravity overcomes surface tension and flattens the drops. Those larger, high *Bo* drops were not considered for this study. The $\alpha = 0°$ case is most readily compared with other studies in the literature that use only airflow forcing.

For the data sets with $\alpha > 0°$, there exists a maximum drop volume which can adhere to the surface. This is evident in Fig. 11 where the trend takes a downward turn and intersects with the horizontal axis. Drops in this regime are very sensitive to initial conditions such as contact line shape. Likewise, other factors include small deviations in the drop volume applied with the syringe technique, imprecision in the apparatus' ability to control the tilt angle, and even surface conditions. Furthermore, evaporation may have an effect on the drop volume as the tunnel speed accelerates.

These factors may all combine to produce significantly varying runback threshold values for a particular combination of drop size and surface inclination. For instance, for the $\alpha = 20°$ data, 135 μL drops had a wide range of runback thresholds; some drops experienced runback without airflow at 20° inclination, while others did not experience runback at that angle until forced with $U > 6$ m/s. For each inclination angle, the variability in critical flow velocity is greatest at the extremes of drop volumes tested and smallest near the middle of the volume range.

The experimental procedure calls for the surface to be cleaned with alcohol between each drop experiment. It was discovered that the amount of time between cleaning the surface and applying the drop is correlated to strong difference in drop stability. It is hypothesized that this effect is due to varying dryness of the surface; a short time lapse before drop application may not allow the alcohol to completely evaporate. In that case, the water drop is placed on a thin layer of liquid alcohol. To prevent this from interfering with results, a sufficiently long time period (around 30 seconds) was required to pass between surface cleansing and drop application. Airflow over the surface encourages evaporation to aid in this process.

Also of interest is where the curves traced out by the data sets in Fig. 11 intersect the horizontal axis, i.e., what drop volume is unstable to gravity forcing alone without airflow. The experimental procedure that produced Fig. 11 is not conducive to such an investigation, so another procedure was devised.

The no-wind procedure is to carefully deposit drops between 15 and 400 μL on the surface to maximize the roundness of the drops. Then, the tilt mechanism was engaged to increase the surface inclination at a rate of 1°/s until the drop ran. As the inclination angle increases, the drops begin to elongate in the downslope direction, while the upslope portion of the contact line remains fixed. The critical inclination angle was recorded for each drop. The results of the critical inclination

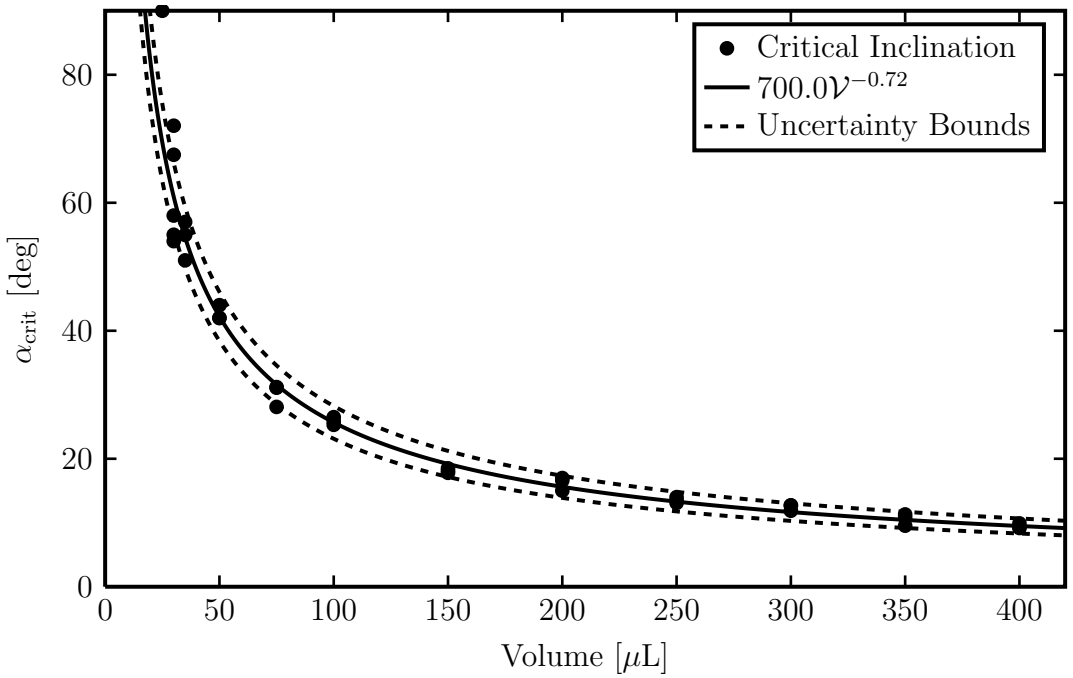

Fig. 12 : Critical inclination angle and curve fit for drops without wind forcing ($U = 0$).

angle experiments are shown in Fig. 12. Angle measurements are assumed to have an uncertainty $\sigma_{\alpha_{\text{crit}}} = 0.1°$, approximately the precision with which the wind tunnel can be zeroed to the horizontal orientation.

In a similar fashion to the wind-forced drop experiments, the critical inclination angle or point of incipient motion of the drop is defined as the angle measured when the upstream contact point was observed to begin moving downstream. The downstream contact point moves long before the upstream, in agreement with observations Bikerman (1950) and others have made of gravity-forced drops.

A power law is empirically chosen to fit the data well, as $\alpha_{\text{crit}} = a\mathcal{V}^b$, where $a = 700 \pm 68$ and $b = -0.72 \pm 0.03$ with units corresponding to α_{crit} in degrees and $\mathcal{V}$ in microliters. Uncertainty propagation is applied to produce a fit for the data, along with a 1–σ error bound, shown by the dashed lines in Fig. 12. To determine the

volume of a drop with a particular α_{crit} (such as 10°, 20°, 30° in Fig. 11), a simple inversion of the equation $\alpha_{\text{crit}} = a\mathcal{V}^b$ is required. Moreover, the uncertainty in crtitical volume for a particular inclination angle is found simply by calculating the points where the 1–σ curves intersect a particular line of constant α_{crit}. Is is these error bounds plotted along the horizontal axis of Fig. 11.

Beyond simply providing $U_{\text{crit}} = 0$ data for Fig. 11, these observations of the critical inclination angle for incipient motion of gravity-forced drops can be used to determine the force necessary to dislodge a drop from its position. Doing so under wind-forcing conditions is essentially intractable from experimental approach due to the complex flow field and combination of pressure and shear forces acting on the drop. However, gravity-forced drops present a much simpler case. Fig. 12 contains the necessary data to calculate the dislodging force as a function of volume. As given in Eq. 2.2, the maximum adhesion force of a drop is equal to the force applied by gravity at the critical inclination angle, $F_{\text{adh}} = mg \sin \alpha_{\text{crit}}$. Since α_{crit} is recorded for each drop, the adhesion force may be calculated using the drop mass $m = \rho_{\text{water}}\mathcal{V}$. For the system under test here, the relationship between critical force and drop volume is shown in Fig. 13 with accompanying uncertainty bounds. The error bars on the symbols represent uncertainty of F_{adh} calculated from drop volume and α_{crit} while the dashed lines are 1–σ bounds on the power law fit of the data.

The relation of drop volume to linear drop dimensions is shown in Fig. 14. Drop dimenions here are taken from sideview images. Conversion from image space to pixel space is carried out through a pixel scale factor, calculated from a scaling image. The uncertainty in locating the edge pixels of the scale object are taken into account and produce the pixel scale and uncertainty. These measurement errors are then carried through all the following equations involving drop dimensions, producing for instance, the sideview drop height and uncertainty, $h_{\text{sv}} \pm \sigma_{h_{\text{sv}}}$.

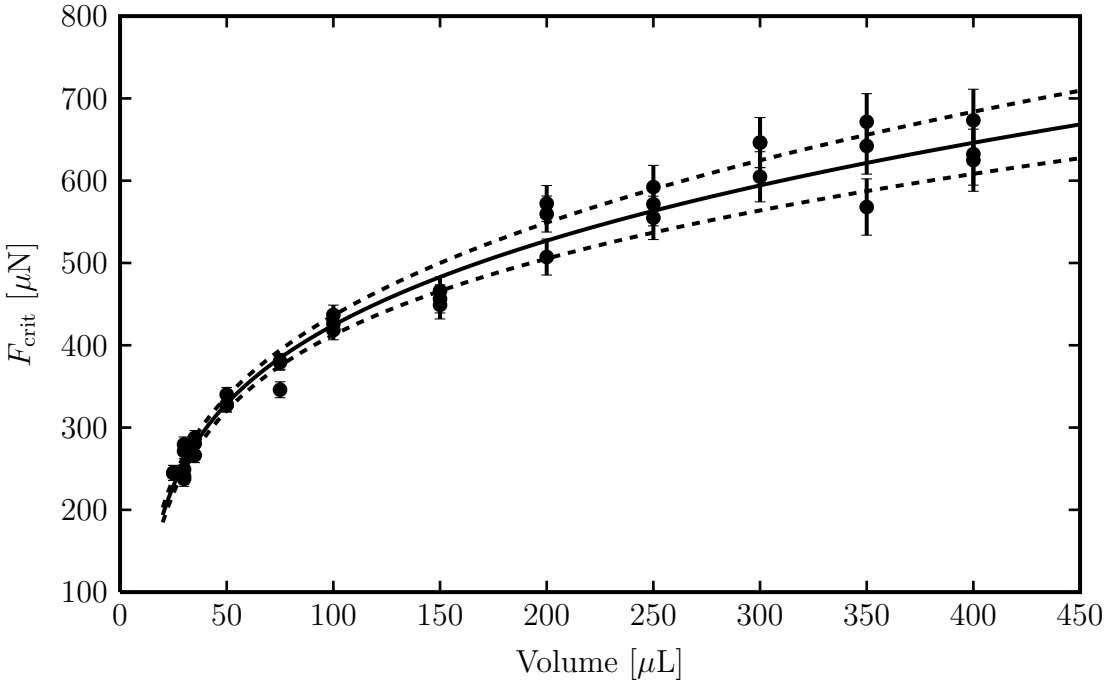

Fig. 13 : Adhesion force for drops without wind forcing ($U = 0$). Error bars are the calculated force uncertainty for each drop, while the dashed line is the uncertainty bound from the power law fit of the data

The sideview images were used to measure the width and height of each drop as initially placed on the surface. The sideview contact points and maximum drop height location were manually identified and used to calculate w_0 and h_0, the initial width and height of the as-placed drops. These values are plotted in Fig. 14 as a function of drop volume. In the absence of gravity and on an ideal surface, both w_0 and h_0 scale as $\mathcal{V}^{1/3}$, as the drops assume a spherical cap shape. However, gravity and roughness create deviations from the ideal behavior. As drop volume becomes large, the Bond number $Bo = \rho g h^2/\gamma$ becomes large, indicating the gravity force on the drop has a larger influence than surface tension. Increasingly large drops are flattened with the height approaching a constant value, while the width tends toward a $\mathcal{V}^{1/2}$ relation.

Within the range of drop volumes used in experiments here, a power law is found to fit the data well, where $h_0 = a\mathcal{V}^b$, with $a = 0.738 \pm 0.014$ and $b = 0.245 \pm 0.004$.

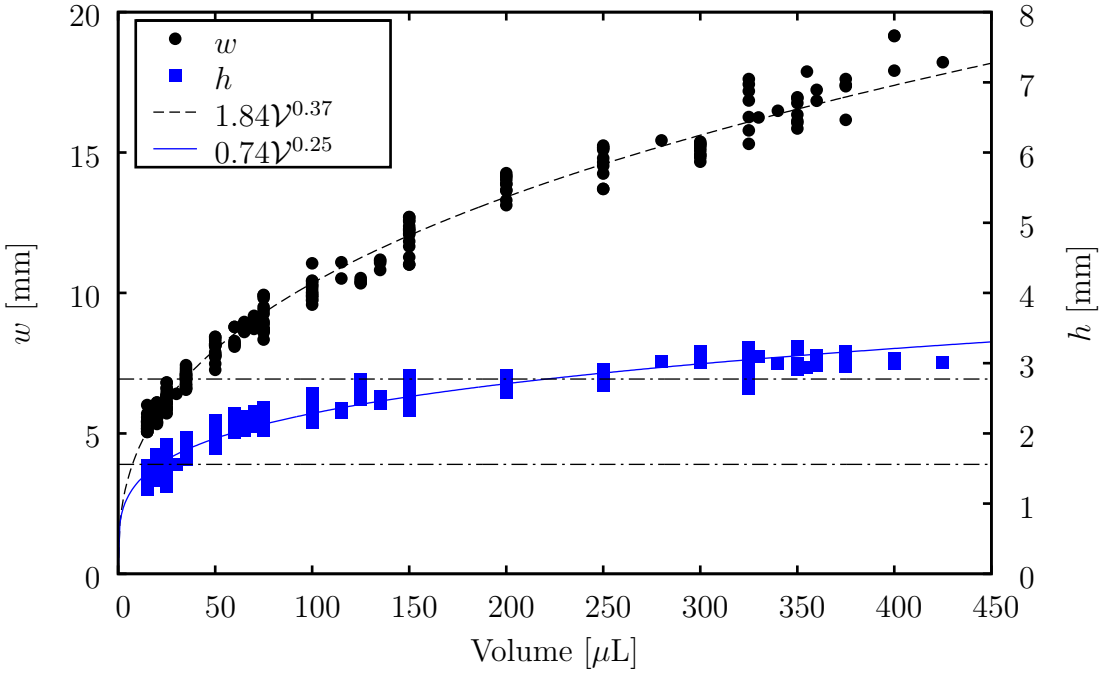

Fig. 14 : Drop dimension measurements and curve fits as functions of volume, $\mathcal{V}$. Dot-dashed lines are boundary layer thickness for $U = 4$ and 12 m/s based on 99% of freestream speed in Eq. 2.7.

The fit parameters for drop width are $a = 1.84 \pm 0.03$ and $b = 0.374 \pm 0.003$. The exponent for the drop height fit is less than 1/3, while the drop width exponent is greater than 1/3, indicating that gravity has a non-negligible influence for these drops. However, it is reassuring that the height exponent plus twice the width exponent is equal to one.

Engineering applications of drop runback limits and behavior will most likely not simulate drop shapes. For this reason, all non-dimensional numbers are calculated based on the properties of the initially deposited drop. Thus, the appropriate Reynolds and Weber numbers are Re_{h_0} and We_{h_0}, where h_0 is the initial height of the drop. Henceforth the subscript is dropped.

The height of the drop relative to the boundary layer thickness determines what portion of the drop is exposed to the shear flow and the freestream flow. The ratio of drop height to the momentum thickness of the boundary layer at the critical velocity gives values for h/δ^*_{crit} in the range of 3–7. Scaling instead by the boundary layer thickness based on 99% of U in the boundary layer fit (Eq. 2.7), shows the drop height is 0.9–2.1 times the boundary layer thickness.

The advancing and receding contact angles for the surface were calculated as the mean of multiple independent contact angle measurements from sideview images drops at the runback threshold. The advancing and receding contact angles are $\theta_{\text{a}} = 63.5^\circ \pm 3.7^\circ$ and $\theta_{\text{r}} = 8.2^\circ \pm 1.5^\circ$, for a corresponding contact angle hysteresis $\Delta\theta = 55.3^\circ \pm 4.0^\circ$.

Work by Milne (2009) shows the velocity thresholds for wind-forced drop runback collapse to self-similar curves when plotted against a the drop size parameter $(w/A)^{1/2}$, where w is the base length of the drop and A is the drop area, both as viewed from the side. The approach used by Milne to arrive at this conclusion is to first represent

the adhesion force of the drop as

$$F_{\text{adhesion}} = k\gamma w \left(\cos\theta_R - \cos\theta_A\right), \tag{3.1}$$

a quantity easily calculable from sideview image measurement, where k is a proportionality constant. Meanwhile, the forcing of the drop by air is represented as

$$F_{\text{air}} = \frac{1}{2}\rho C_D A U^2 \tag{3.2}$$

where C_D is the typical aerodynamic drag coefficient, which is related to the upstream projection of the drop area, but depends strongly on the drop shape. Equating these two forces produces Eq. 1.2, where the constants k and C_D cannot be determined a priori. Milne hypothesizes that the ratio k/C_D is itself a non-linear function of $(w/A)^{1/2}$.

To replicate this analysis, the spherical cap approximation is once again used along with the known drop height and sideview base width. The parent sphere has radius

$$R = \frac{w^2 + 4h^2}{8h}. \tag{3.3}$$

An equation is derived for the sideview area by integrating the equation for the sphere height across the base length, resulting in

$$\begin{aligned} A &= \int_{-w/2}^{w/2} \left[\sqrt{R^2 - x^2} + (R - h)\right] dx \\ &= 2h\frac{w}{2} + \frac{w}{2}\sqrt{R^2 - \left(\frac{w}{2}\right)^2} + R^2 \tan^{-1}\left(\frac{w}{2}\Big/\sqrt{R^2 - \frac{w}{2}}\right) - 2R\frac{w}{2}. \end{aligned} \tag{3.4}$$

The quantity $(w/A)^{1/2}$ has units of $\text{m}^{-1/2}$, and arises from Eq. 1.2. Furthermore, Milne showed all the data collapse when both U_{crit} and $(w/A)^{1/2}$ for each drop are normalized by their values for a particular drop volume. Fig. 16 demonstrates the results of this procedure. The slight differences in slope between the four datasets in

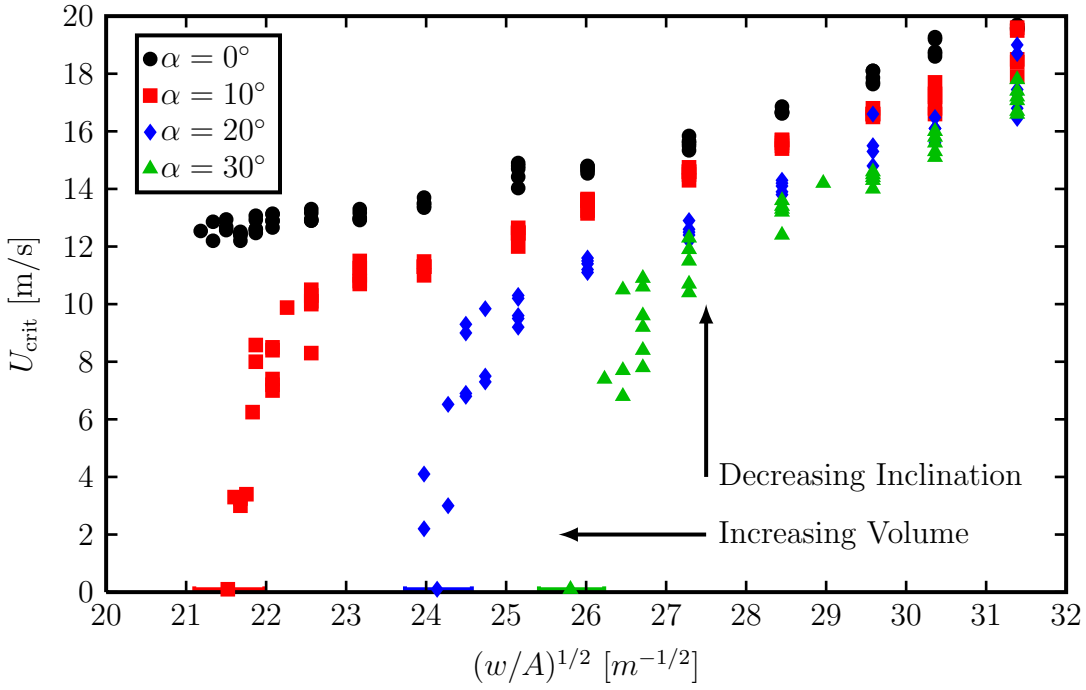

Fig. 15 : Runback thresholds shown as critical velocity as a function of the parameter $(w/A)^{1/2}$

this figure indicate the effect of gravity forcing on the drops. Furthermore, the steep drop in critical velocity is hypothesized to be the point where the effects of gravity forcing are the dominant factor in drop stability. This will be discussed further in the next chapter.

The experimental data by Milne falls within the same parameter regime in Fig. 15 and obeys the same trend as the $\alpha = 0°$ data here. The apparent linearity of the data in critical air velocity can be described by

$$U_{\text{crit}} = a \exp\left(b(w/A)^{1/2}\right). \tag{3.5}$$

where each system of liquid and surface has different fit coefficients.

Figure 17 presents the drop stability threshold data in fully nondimensional form, with Weber number as a proxy for flow speed and Bond number as a proxy for drop size. A contour map of Reynolds number is also shown, where an expression for the

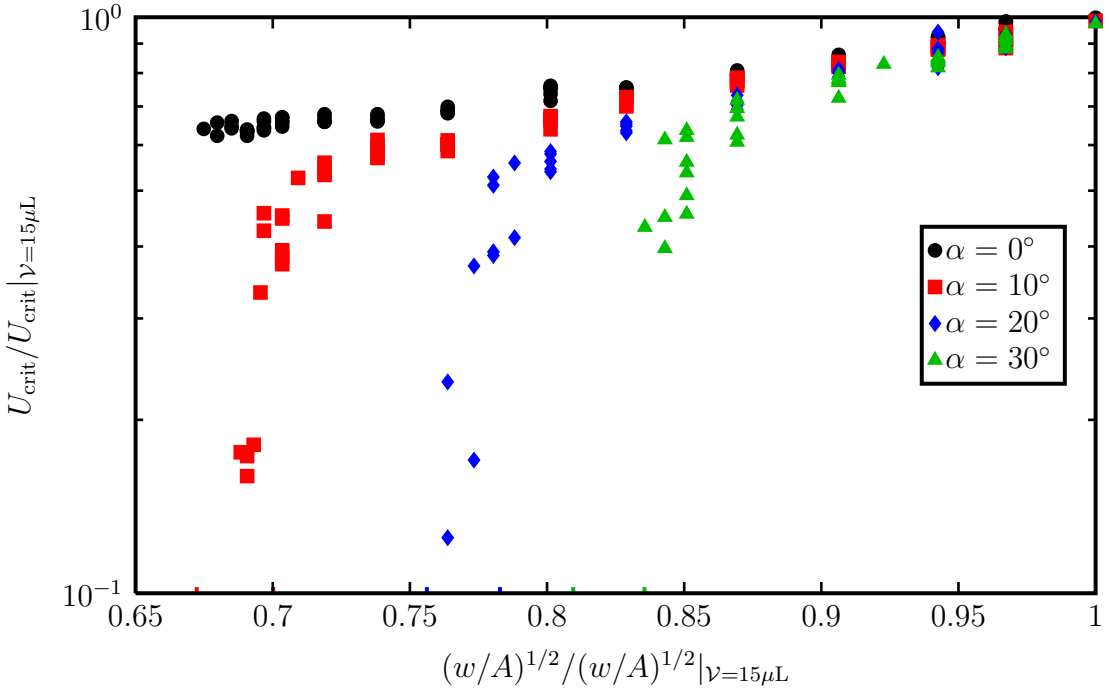

Fig. 16 : Normalized drop runback thresholds shown as critical velocity as a function of the parameter $(w/A)^{1/2}$. Both velocity and $(w/A)^{1/2}$ are normalized by their values for the smallest drops, $\mathcal{V} = 15$ µL

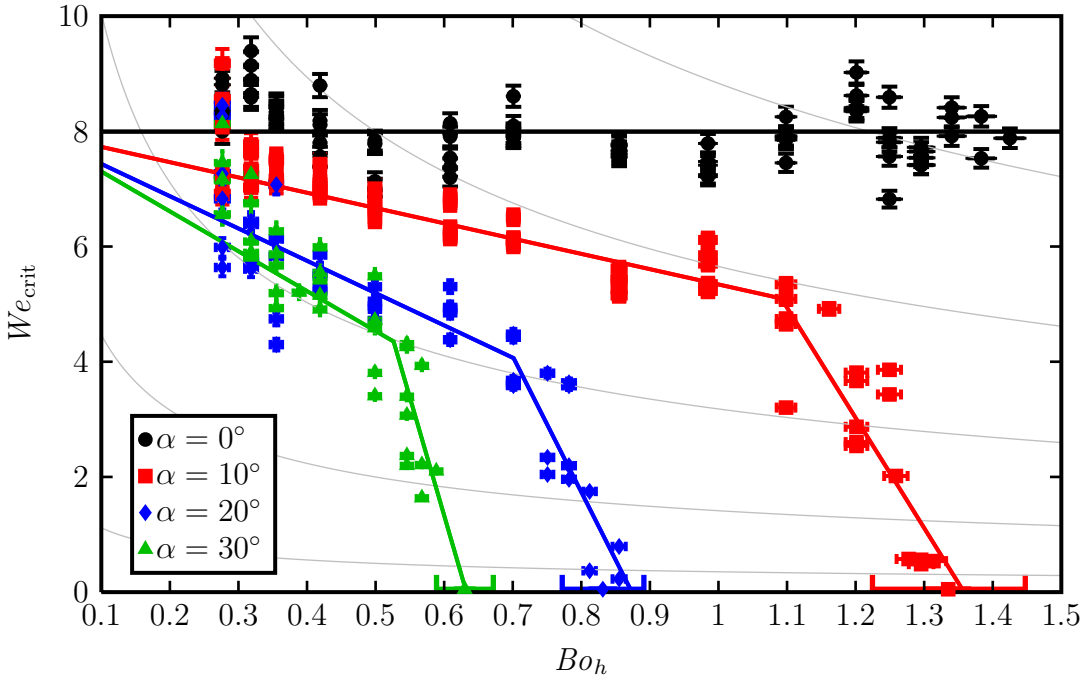

Fig. 17 : Critical Weber number as a function of Bond number. Contour lines are constant Reynolds number, beginning at the bottom with $Re = 500$ with incremental increases by 500

Reynolds number is derived as a function of Bond and Weber numbers alone. Most drops fall within the range $1000 < Re_{\text{crit}} < 2000$. Drops for $\alpha = 0°$ were observed to undergo significant oscillations for large volumes. For smaller volumes, the $\alpha = 0°$ drops were observed to undergo smaller oscillations at and just above the critical flow speed. These conditions correspond to Reynolds numbers greater than 2000, while all but a handful of drops in the $\alpha > 0$ cases had runback thresholds for which $Re_{\text{crit}} > 2000$. The $\alpha > 0°$ drops were not observed to undergo significant oscillations and generally behaved in a steady manner. The condition $Re > 2000$ then signifies a change in the system behavior, where drop interface oscillations come into effect. Perhaps the increased data spread for $\alpha = 0°$, $Re > 2500$ drops can be explained by the effect of unsteady interface dynamics on the stability threshold.

Drops with zero inclination experience runback at a nearly constant Weber number

of 8.0 ± 0.5. That such a threshold exists agrees with the constant Weber number threshold of White and Schmucker (2008) for water drops on aluminum in a turbulent stagnation point boundary layer. Furthermore, though the work by Ding and Spelt (2008) is for the low-Re regime, they observed that the critical Weber number appears to eventually approach a constant value as Re is increased. The Reynolds number here is between 1500 and 3000, far above the maximum Reynolds number of 74 used by Ding and Spelt, thus well into the regime where they predict constant Weber number runback.

For the three sets of drops with non-zero inclination, the critical Weber number is not constant. Increasing from zero Bond number, the critical Weber number decreases linearly. This trend does not continue indefinitely; there is a corner where the critical Weber number takes a sharp downward turn as Bond number continues to increase. It is hypothesized that the point where this change occurs is indicative of an experimental configuration where the forcing by gravity becomes important relative to the forcing by airflow. This will be discussed further in following sections. Fig. 18 shows the relationship between airflow and gravity forcing as a function of Bond number. Naturally, for $\alpha = 0^\circ$ drops, all forcing is provided by airflow. For inclined drops however, the fraction of forcing provided by the air decreases with increasing Bond number or drop size.

The corner location from Fig. 17 is plotted as a vertical dashed line in Fig. 18. These lines intersect with the data trends at approximately 0.2 for all three inclination angles. As a general rule, then, the effect of gravity on the stability limit is important when it provides more than 80% of the necessary to dislodge a drop by gravity alone. The effect of this partitioning of gravity and wind forcing on the evolution of the drop will be discussed further in Chapter IV. The relatively large magnitude of Weber and Reynolds number indicates the importance of pressure and intertial forces in

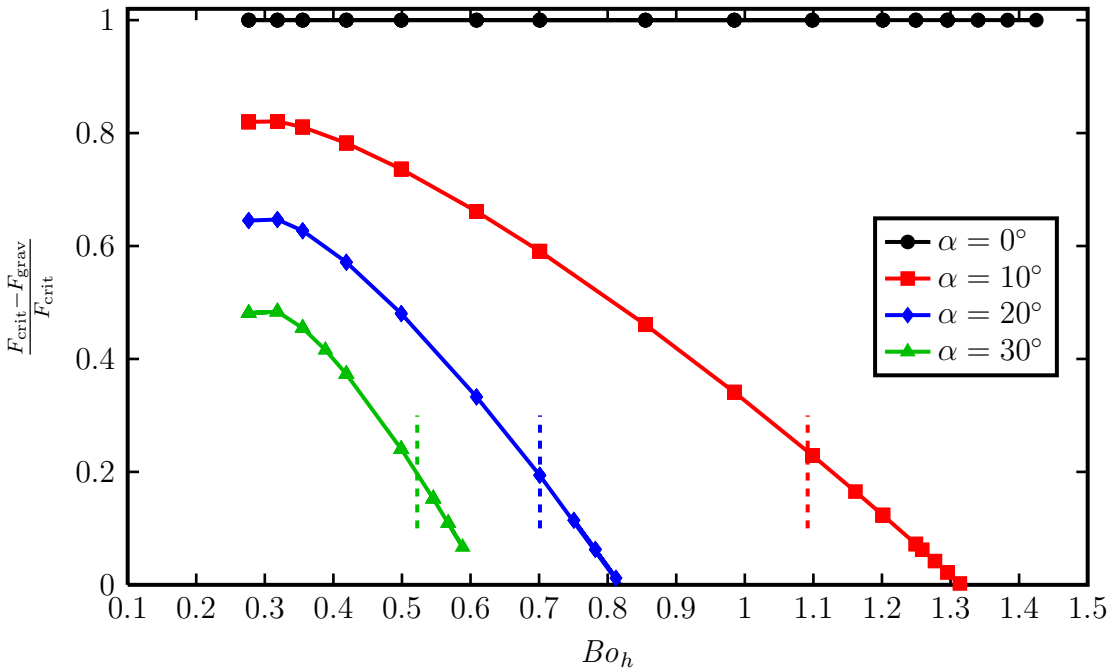

Fig. 18 : Fraction of critical drop force applied by airflow as a function of Bond number and inclination angle. Vertical dashed lines indicate the break in slope from Fig. 17

determining the stability limits. Meanwhile, the drops here have capillary number, $Ca = We/Re = \mu U/\gamma$, much less than one, indicating viscosity (and thus shear force) plays little role in the downstream forcing on the drop.

CHAPTER IV

DROP BEHAVIORS

Macroscopic stability limits of drops subjected to gravity and wind forcing on a rough aluminum surface were presented in the previous chapter. As discussed in Chapter I, Section C, while these global stability parameters are useful, opportunity remains for better understanding of drop stability through accurate measurements of the profiles of forced drops and their evolution as applied forcing increases. This chapter contains analysis of the features and behavior of the drops as they are brought to critical forcing conditions. This analysis is conducted to gain insight into the questions posed in Chapter I, Section C, which are "How do the contact line and contact angle distribution evolve as increased forcing is applied?" and "What is the shape of a wind-forced drop at the runback threshold?" The specific objective laid out was to "measure the evolution of the drop profile, contact line shape, and contact angles as gravity and wind forcing are increased."

This first section of this chapter presents the reconstruction results for a single realization of the experimental procedure applied to a typical drop. The drop evolution is traced from its initial placement on the surface until runback. Then results from several other drops are presented to compare and constrast their behavior over the parameter range. The important features of drop evolution are discussed in anticipation of the following section, where the same types of results are presented as average behavior over the whole sample of drops.

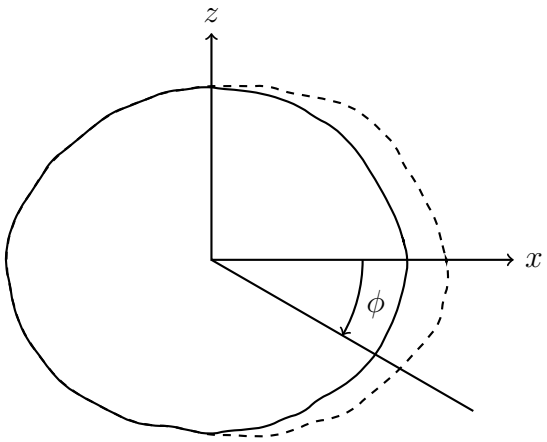

Fig. 19 : Drop contact line and coordinate system for contact angle distribution plots. The angle ϕ is defined from the center of the initially sessile drop (solid line) and remains so for evolving drop shapes (dashed line)

A. Typical Drop Evolution

To provide some familiarity with the results of an experiment and the output of the measurement technique, the process is described here for a representative drop. The experimental conditions for the selected drop are a volume of 50 μL and a surface inclination angle of 0°.

When discussing reconstruction results it is necessary to define a coordinate system to identify position along the contact line. Following the convention of Ding and Spelt (2008), the position along the contact line is defined as the angle ϕ in Fig. 19. The center of this coordinate system is the center of the elliptic grid produced by the drop reconstruction analysis algorithm for the first image in a drop sequence. The origin of the ϕ coordinate system remains fixed even as the drop deforms and its contact line spreads downstream.

Contact line location is measured from the topview drop images. For this drop, the contact line, shown in Fig. 20, did not move during the first four captured images, meaning that in response to the flow the drop was able to sufficiently reconfigure its

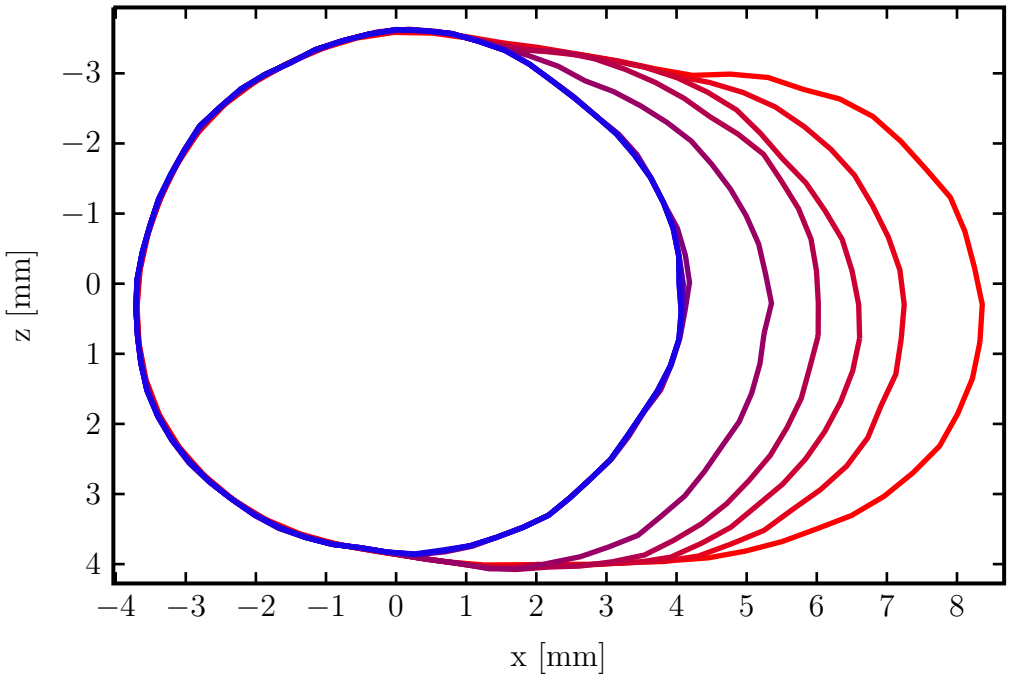

Fig. 20 : Contact line evolution for a typical drop, in this case, a 50 μL drop with inclination $\alpha = 0°$. Line color indicates relative flow speed: blue is $U = 0$ and red is $U = U_{\text{crit}}$, with a smooth gradient between

interface shape with that initial contact line to resist any motion in the surface plane. By the fifth measurement, for which the flow velocity was 80% of U_{crit}, the contact line extends in the downstream direction. Beyond that level of forcing, the contact line extends significantly as the drop readjusts its shape.

A sequence of reconstructed profiles for this drop are shown in Fig. 21. Each subfigure also shows the boundary layer profile for the test conditions of that measurement. The velocity is normalized so that the velocity $U = U_{\text{crit}}$ occupies the full range of the x-axis in the final reconstruction. Forcing increases from left to right along each row. Additionally, the freestream velocity and volume of each reconstruction is shown above the drop profile.

The drop begins with approximate circular symmetry. The contact angle is approximately constant about its perimeter. As airflow is initiated, the drop profile

experiences minimal change. The force applied to the drop by pressure and viscosity is insufficient to significantly deform the drop. With further increased flow velocity, changes in the drop shape are seen. As the contact line begins to move, the force of the airflow begins to accumulate more and more of the drop's fluid on the downstream portion of the contact area. Meanwhile, the upstream region of the drop is flattened. When the critical velocity is exceeded, the drop is observed to maintain the critical profile as it slides downstream.

No gravity force is applied to this drop; accordingly, all changes in the drop shape are due to flow only. This behavior is evident in the evolution of reconstructed sideview profiles, seen in Fig. 22. The initial drop configuration (seen in blue) closely resembles a spherical cap. When flow is first initiated, very little change occurs in the sideview profile. With increased flow velocity, the upstream side of the drop is progressively pushed downward by the pressure force, collecting the liquid in the downstream portion of the drop and extending the contact line in the downstream direction.

The evolution of contact angle distribution is shown in Fig. 23. As expected, this drop has an initial profile with nearly constant contact angle, with slight variations accounted for by the lack of perfect circular symmetry and measurement error. This drop's initial contact angle is approximately $49 \pm 1^{\circ}$. The measurement technique detects minimal changes in the contact angle up to flow speeds of 9.8 m/s. For higher flow velocities, the drop is deformed in response to the flow force applied. The first significantly changed contact angle distribution sees the contact angle decrease on the upstream side and increase on the downstream side.

At this point of first significant drop shape deformation, the accuracy of the contact angle measurements begins to degrade. In reality, the contact angle on the downstream side should be very near the advancing contact angle for these experiments. Similarly,

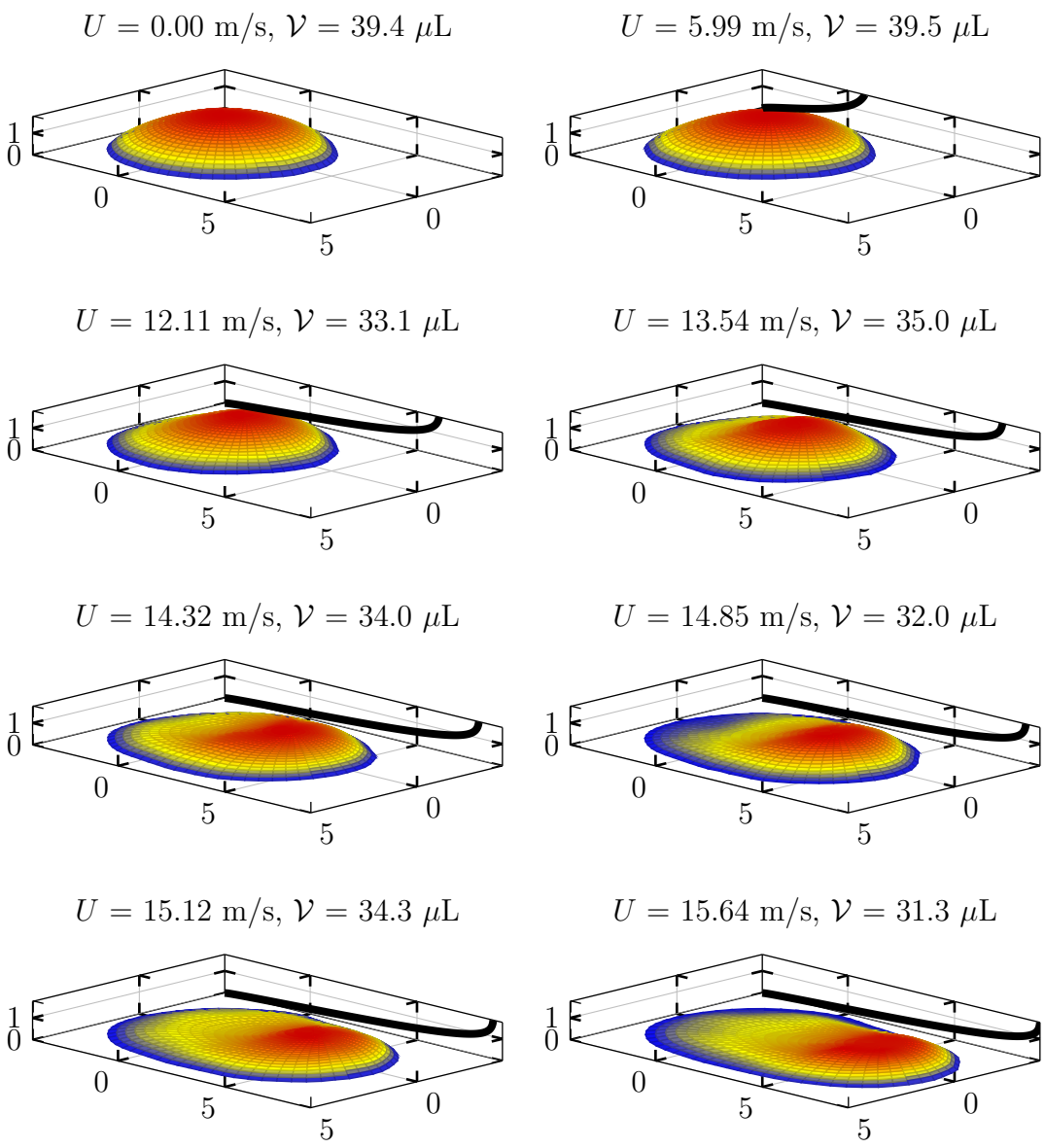

Fig. 21 : Drop profile reconstruction sequence for a typical drop, in this case, a 50 µL drop with inclination $\alpha = 0°$. Boundary layer profile corresponding to the flow velocity for each measurement is shown, with $U = U_{\text{crit}}$ scaled to the x-axis limits

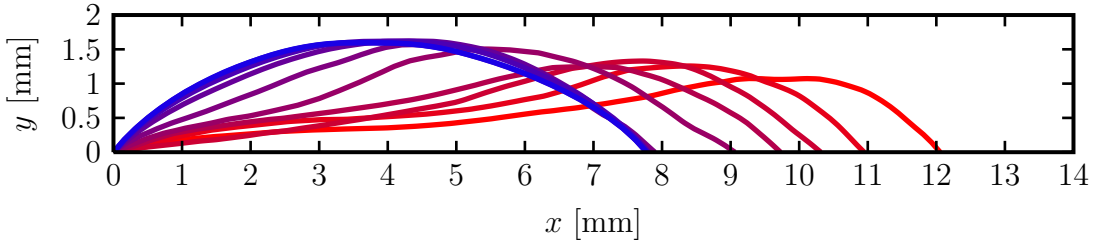

Fig. 22 : Reconstructed sideview profile for a typical drop, in this case, a 50 µL drop with inclination $\alpha = 0°$. Line color indicates relative flow speed: blue indicates $U = 0$ and red indicates $U = U_{\text{crit}}$, with a smooth color gradient between

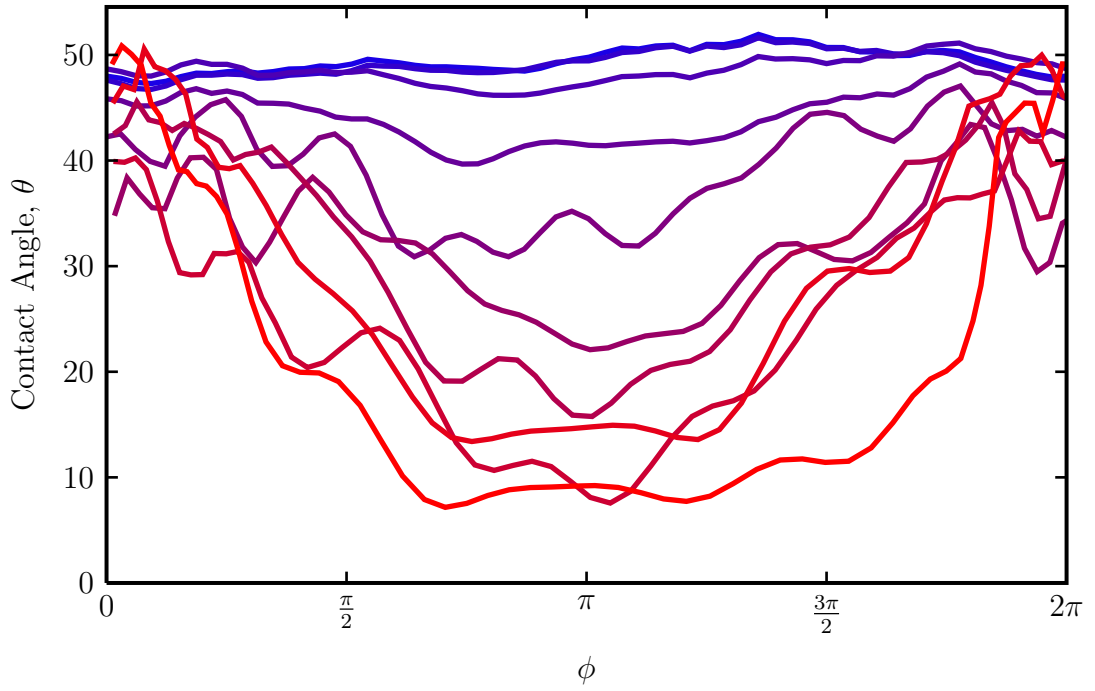

Fig. 23 : Evolution of contact angle distribution for a typical drop, in this case, a 50 µL drop with inclination $\alpha = 0°$. Line color indicates relative flow speed: blue indicates $U = 0$ and red indicates $U = U_{\text{crit}}$, with a smooth color gradient between

the contact angle should be close to the receding contact angle on the upstream side. However, the measurement method fails to produce reconstructions with contact angle distributions that vary so widely. As currently implemented, Bessel–Fourier series reconstruction method is unable to reproduce profiles in which so much of the drop's mass shifts to the downstream end. While these measurements are imperfect, relative changes in contact angle along the contact line still provide useful insights.

The force with which a drop adheres to a surface depends on the action of the surface tension force and is mediated by the drop geometry through contact angles and the shape of the contact line. Sideview measurements of drops are only able to estimate the adhesion force using the drop width and contact angles, as in Eq. 3.1. This simplification hides the complete nature of the contact line shape and only captures the true adhesion force in a crude sense. Full drop profile measurements made here enable adhesion force calculation directly through Eq. 4.1 for the first time. At every point around the contact line, the surface tension acts along a vector perpendicular to the contact line and tangent to the drop surface–this is the vector that defines the contact angle at that point. That adhesion force is given by the integral

$$\vec{F} = \gamma \oint_{\mathrm{CL}} \cos(\theta)\hat{n}\, d\ell \tag{4.1}$$

where θ is the contact angle, $\hat{n}$ is the unit vector normal to the contact line in the surface plane, and ℓ is the differential length element along the contact line.

The integral is calculated as a sum over the grid nodes along the discretized contact line. The contact line normal vector $\hat{n}$ is computed as the normal to the two adjacent grid nodes along the contact line. Since the adhesion force is a vector, the x- and z-components of the adhesion force are computed by simply using the appropriate components of $\hat{n}$. Forcing is applied only in the x-direction in these experiments, so any non-zero result for F_z indicates measurement error. An estimate of measurement

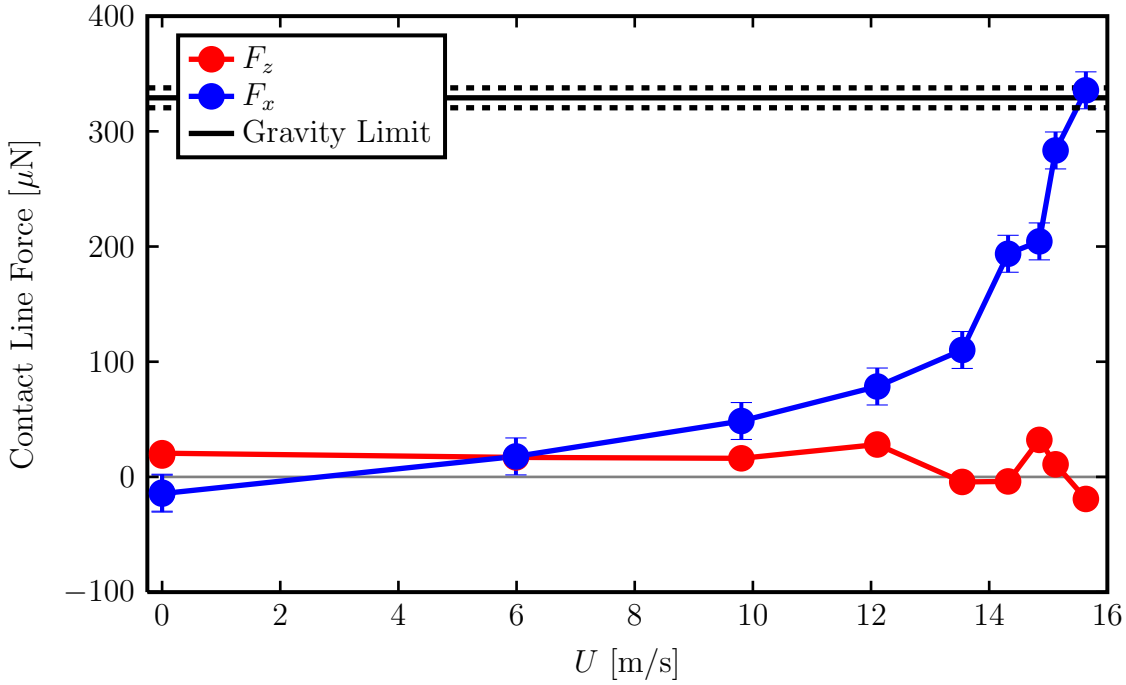

Fig. 24 : Evolution of contact line force for a typical drop, in this case, a 50 µL drop with inclination $\alpha = 0°$.

error in F_x is obtained by taking the root-mean-square of the F_z measurements for each drop.

Applying the contact line force integral, Fig. 24 shows the evolution of contact line force with increasing flow velocity. Only gradual increases in contact line force are observed up to about 9.8 m/s; subsequently, the contact line force increases much more rapidly. The gravity limit and its uncertainty from Fig. 13 is shown to demonstrate the contact line integral technique measures similar forces. In fact, the critical airflow force equal measured for this drop is equal (within uncertainty) to that of the gravity force required to dislodge a drop of the same volume.

Moving on to results for drops at other locations within the parameter space, Figure 25 shows the evolution of sideview profiles for three 15 µL drops at inclination angles of $\alpha = 10°$, $20°$, and $30°$. Due to the small size of these drops, the effect of

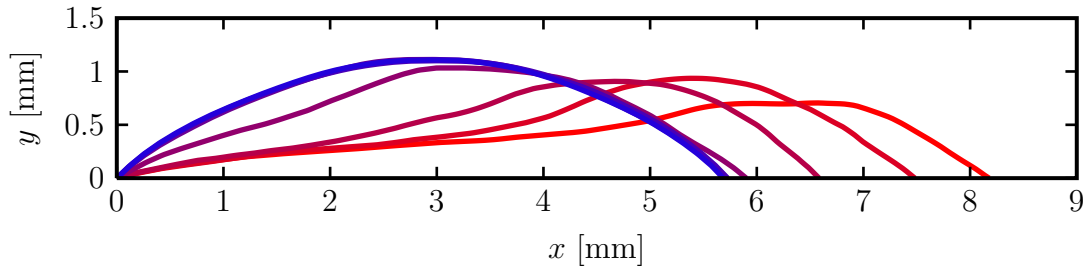

(a) $\alpha = 10°$

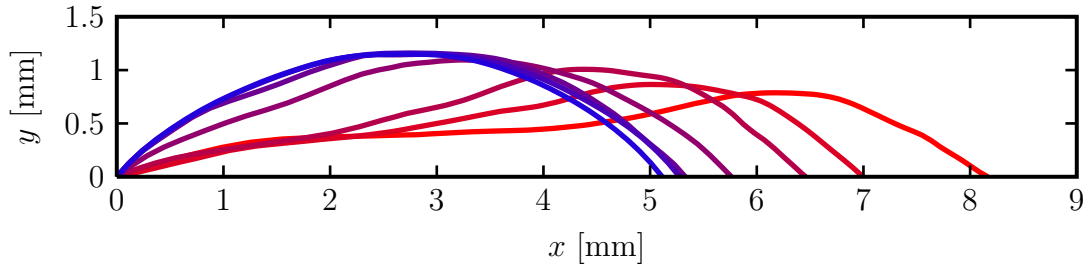

(b) $\alpha = 20°$

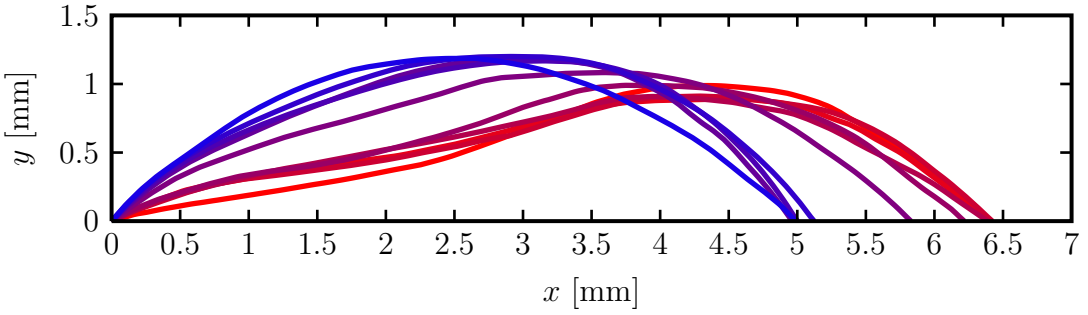

(c) $\alpha = 30°$

Fig. 25 : Reconstructed sideview profiles for 15 μL drops with varying inclination. Line color indicates relative flow speed: blue indicates $U = 0$ and red indicates $U = U_{\text{crit}}$, with a smooth color gradient between

gravity is somewhat small. Accordingly, the stability limits and drop behavior are expected to be dominated by air forcing. Indeed, the evolution of sideview profiles in Figure 25 follows a similar trend independent of the inclination angle, confirming the idea that gravity is insignificant. Only the $\alpha = 30°$ case shows an initial small deformation of the drop due to gravity.

The evolution of contact line force is shown in Fig. 26 for the same drops. The

$\alpha = 10°$ and $20°$ cases see very similar trends, with minimal forcing up to about $0.5U_{\text{crit}}$, then steep force increase as the drop profile shifts toward the critical configuration. The difference evident in the $\alpha = 30°$ case is that an inclination of $30°$ is apparently sufficient to necessitate a reaction from the drop to maintain adhesion to the surface. This agrees well with the sideview profile evolution seen in Fig. 25c.

The same effect of gravity forcing is evident in the contact angle distribution. For example, Fig. 27 shows contact angle evolution for two drops with surface inclination of $10°$. The drops' volumes are 35 μL and 300 μL, which are well within the wind and gravity dominated regimes, respectively (see Fig. 17). Again, the wind dominated drop shows little deformation in the early stages of increasing flow velocity. On the other hand, the large-volume, gravity-dominated drop shows immediate deformation, then experiences only slight variation in its shape due to airflow which supplies the final push toward the runback threshold. The same trends are evident for the other inclination angles. In particular, Fig. 28 shows the contact angle evolution for drops with volumes 15 μL and 70 μL with $30°$ inclination.

To further illustrate the difference between airflow and gravity dominated drop stability, Fig. 29 shows sideview profile evolution for the same two drops in Fig. 28, one much smaller than the air/gravity threshold and one larger. The profiles in Fig. 29a exhibit a region of negative curvature of the drop profile induced by the pressure force on the upstream side of the drop. For the drop in Fig. 29b, however, gravity provides nearly all the force required to dislodge the drop. The remaining force deficit supplied by the airflow is insufficient to produce a strong negative curvature region on the upstream drop face.

Finally, to give a physical perspective of the difference between the profile evolution of an airflow dominated drop (as seen in Fig. 21) a gravity dominated drop profile evolution is shown in Fig. 30. The profiles near the critical velocity in the sequence do

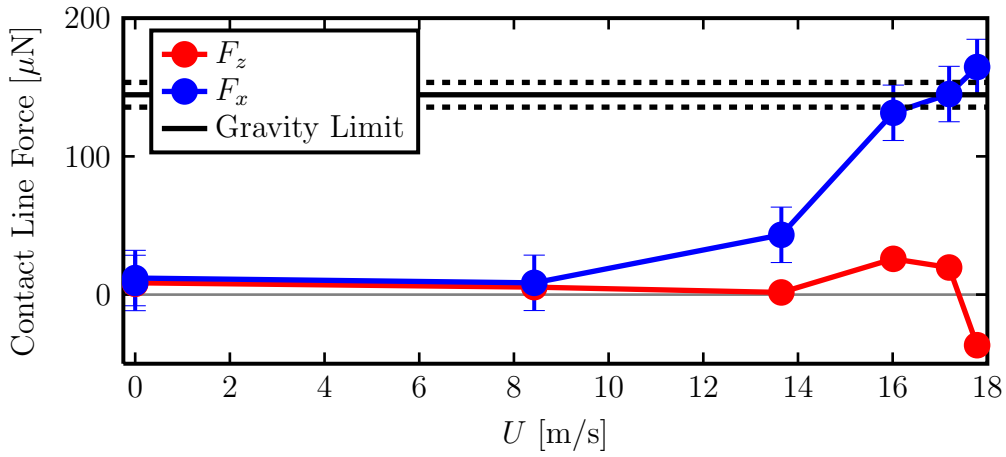

(a) $\alpha = 10°$

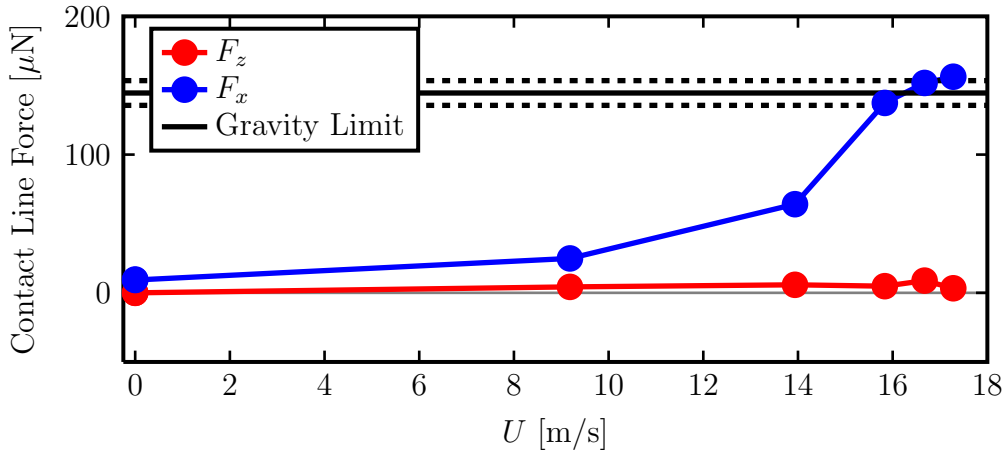

(b) $\alpha = 20°$

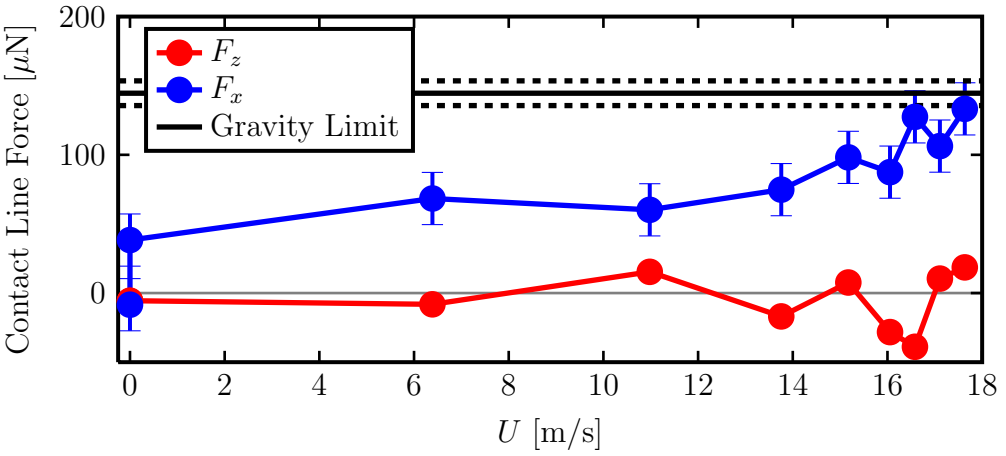

(c) $\alpha = 30°$

Fig. 26 : Contact line force evolution for 15 µL drops with varying inclination

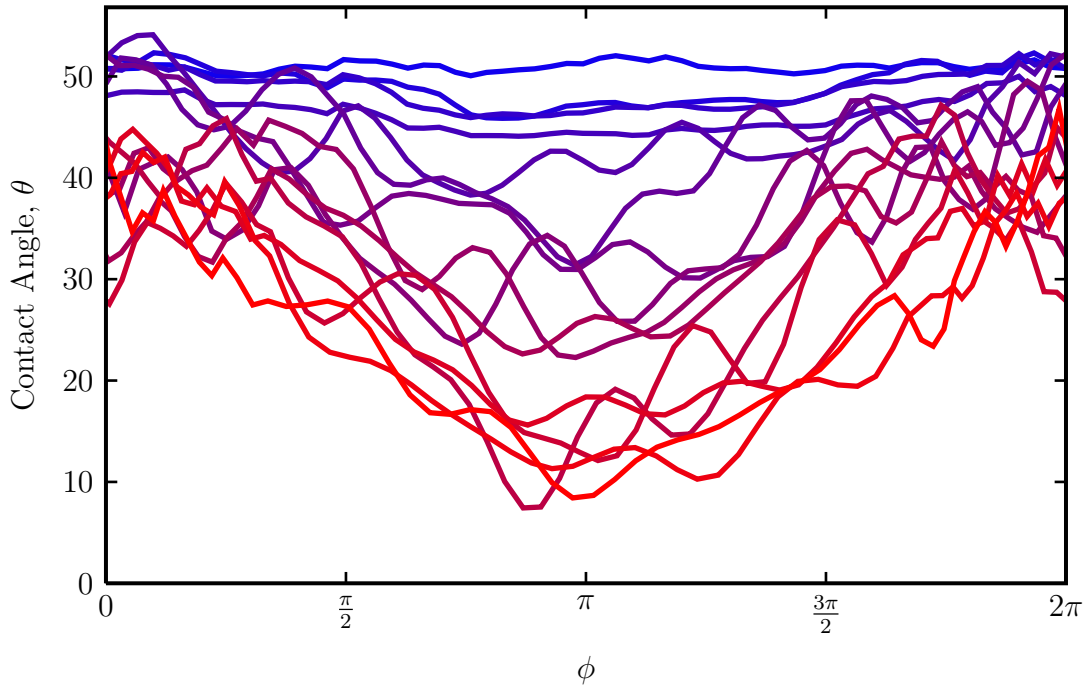

(a) $\mathcal{V} = 35$ µL

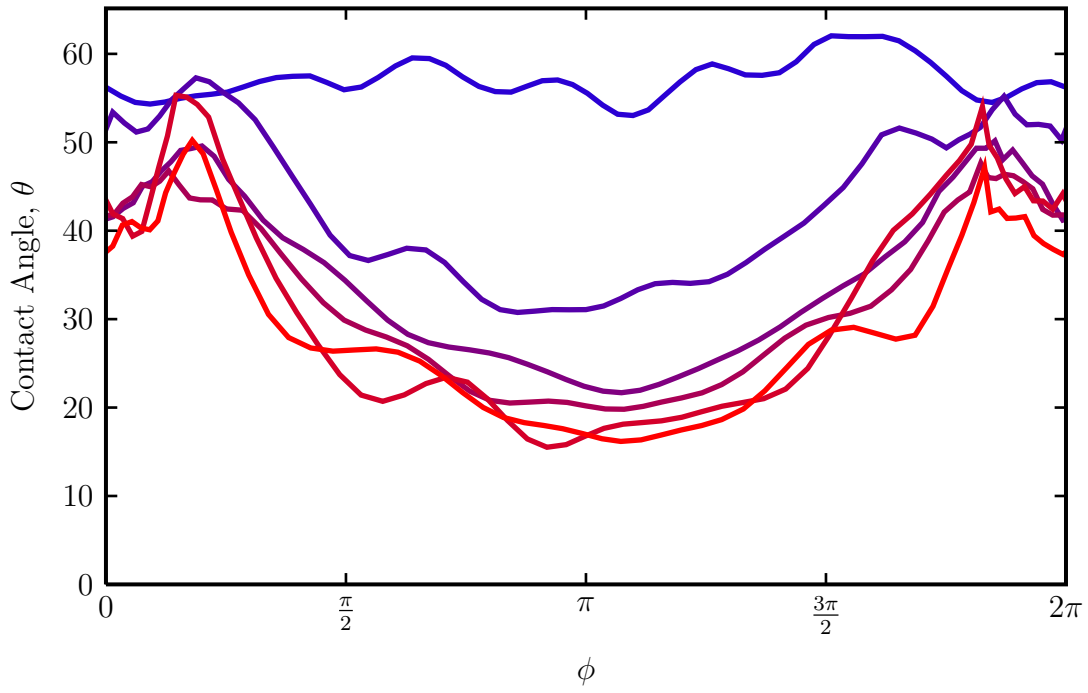

(b) $\mathcal{V} = 300$ µL

Fig. 27 : Contact angle distribution evolution sequence $\alpha = 10°$ drops with varying volume. Line color indicates relative flow speed: blue indicates $U = 0$ and red indicates $U = U_{\text{crit}}$, with a smooth color gradient between

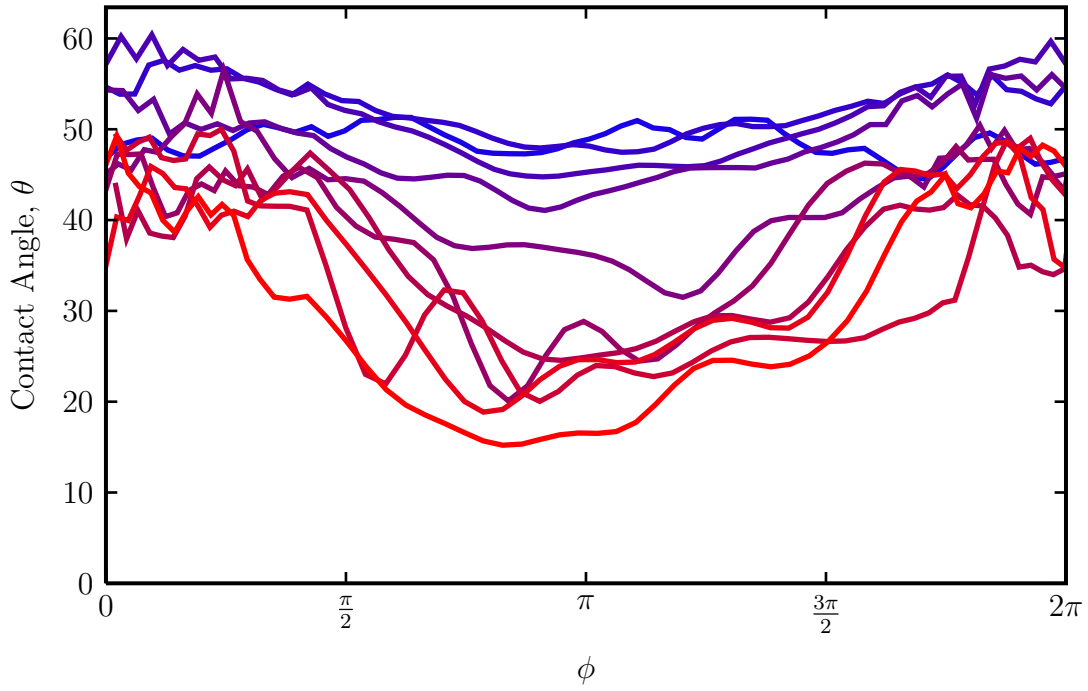

(a) $\mathcal{V} = 15$ µL

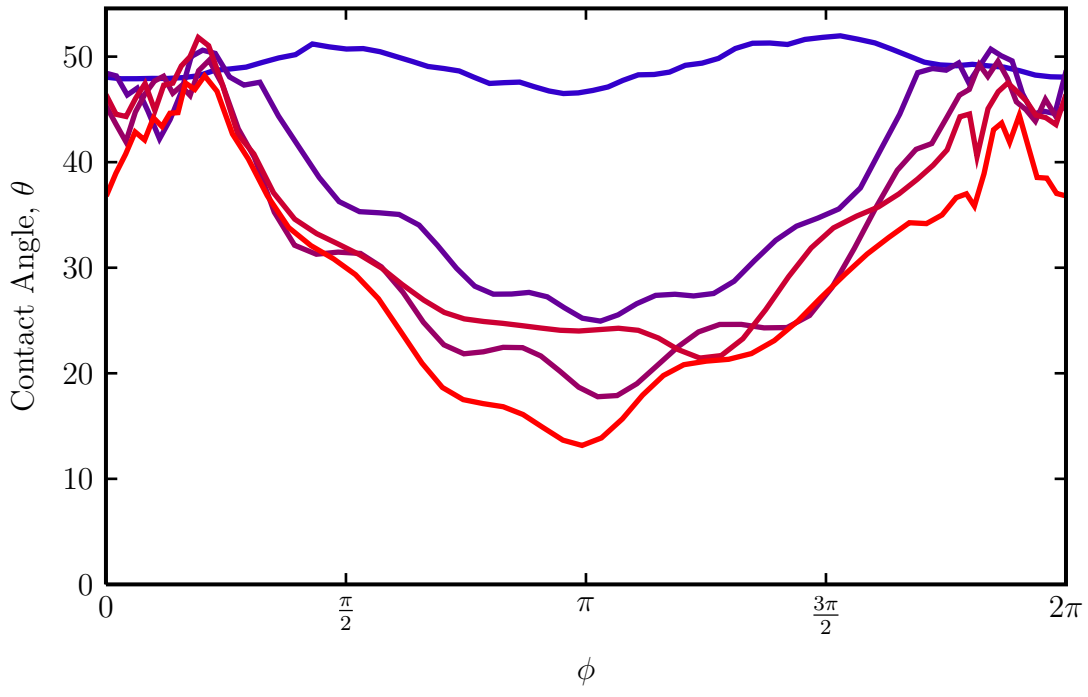

(b) $\mathcal{V} = 70$ µL

Fig. 28 : Contact angle distribution evolution sequence $\alpha = 30°$ drops with varying volume. Line color indicates relative flow speed: blue indicates $U = 0$ and red indicates $U = U_{\text{crit}}$, with a smooth color gradient between

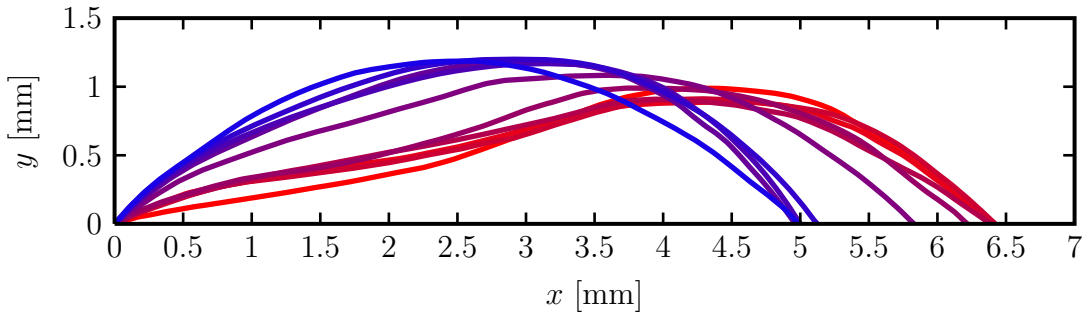

(a) $\mathcal{V} = 15$ µL

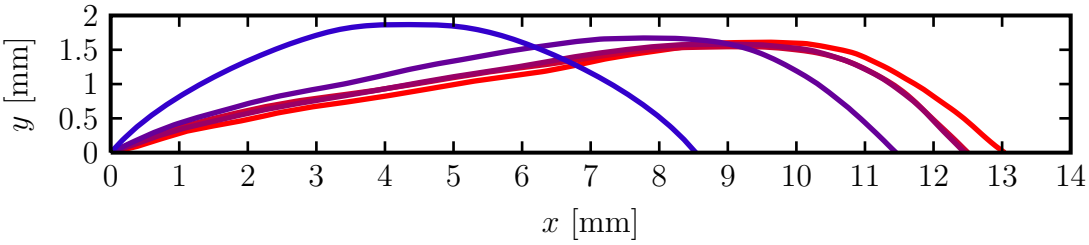

(b) $\mathcal{V} = 70$ µL

Fig. 29 : Sideview profile evolution for drops at surface inclination of 30°

not exhibit the flat upstream region and accumulated fluid in the downstream region. Rather, the drop profiles maintain a fairly smooth curvature across the entire contact area.

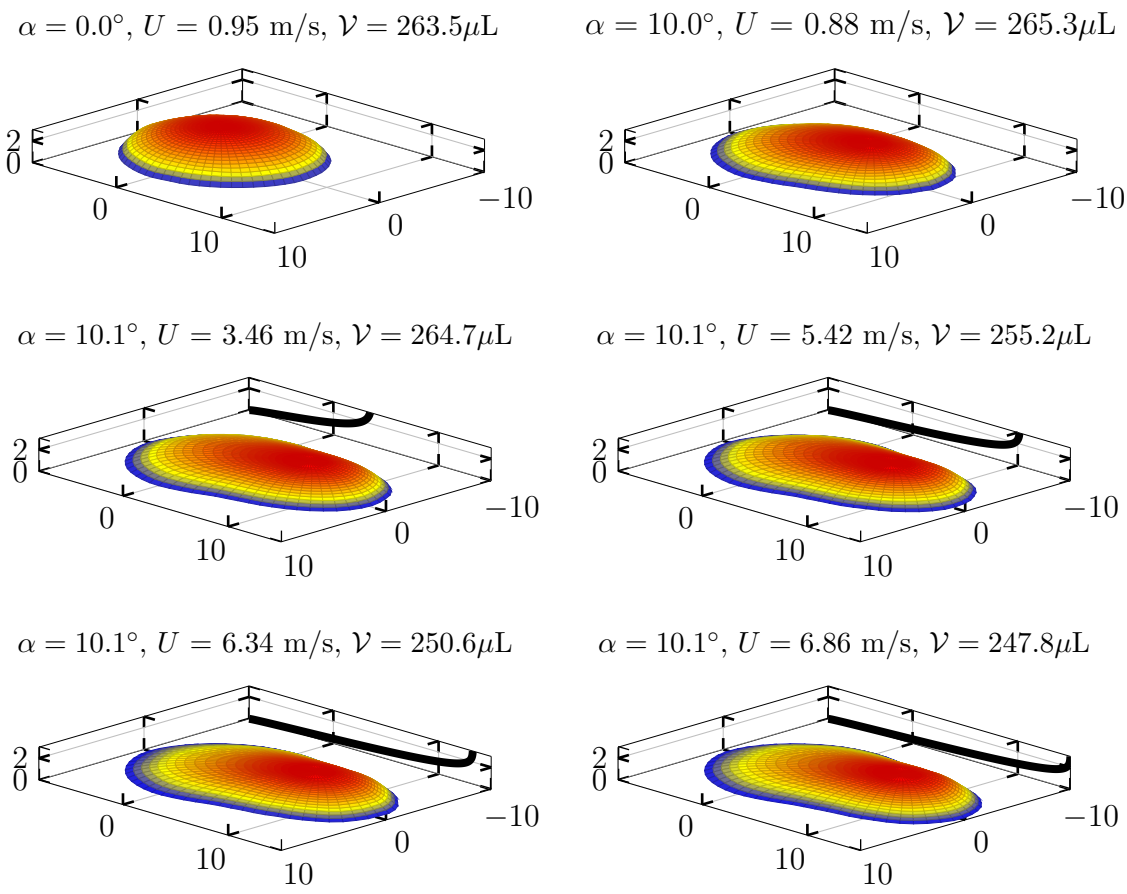

Fig. 30 : Drop profile reconstruction sequence for a typical drop, in this case, a 300 µL drop with inclination $\alpha = 10°$. Boundary layer profile corresponding to the flow velocity for each measurement is shown, with $U = U_{\text{crit}}$ scaled to the x-axis limits

B. Aggregate Drop Evolution

1. Contact Line Evolution

The contact line shape is a critical component of a drop's ability to adhere to the surface. It defines the direction along which surface tension acts in the plane of the substrate. Knowledge of likely contact line shapes and how the drop evolves from its initial placement until runback are important to understand how the drop reconfigures itself to counteract increased forcing. Several other studies in the literature have studied this element of the drop stability problem; those results will be discussed in relation to the current results when appropriate.

Numerical simulations by Dimitrakopoulos and Higdon (1998) used two different conditions for the motion of the contact line. In one configuration, the contact line was not allowed to spread in the spanwise direction, while the other permitted such behavior. They hypothesized that these two conditions occur in an experiment depending on initial conditions. The constrained case occurs when the initial contact angle is θ_a and slight airflow forces the downstream hysteresis condition to be violated first. The unconstrained case corresponds to a drop with an initial contact angle of θ_r, so that initiation of airflow first violates the hysteresis condition on the upstream side, causing the drop to expand in the spanwise direction. Ding and Spelt (2008) attempted to replicate the behavior observed by Dimitrakopoulos; two of the selected test cases had initial contact angle $\theta_0 = \theta_a$ and $\theta_0 = \theta_r$.

The technique used for drop application in these experiments produces drops with initial contact angle much closer to θ_a than to θ_r. Following the hypothesis of Dimitrakopoulos, the drops should extend in the downstream, not spanwise, direction. In fact, this is precisely what was observed for nearly all drops. Drops that did not behave this way did not undergo spanwise extension of the type Dimitrakopoulos

observed; rather, these drops simply ran downstream with a slight misalignment to the flow direction. While the precise cause of this behavior is unknown, it was only observed in rare cases and is most likely due to atypical initial conditions or an inhomogeneous surface state resulting from improper cleaning.

In the context of this hypothesis by Dimitrakopoulos, the drop data are used to investigate the change of contact line shape. The circumferential position around the drop is defined as in Fig. 19, with the origin remaining at the grid center of the initial drop (solid line), even as the contact line shape evolves and extends downstream (dashed line).

For each drop image in a sequence, the contact line is detected as part of the image analysis and drop profile reconstruction. A distribution of drop radius as a function of ϕ is calculated using the K points on the drop boundary and the center point of the drop. The initially placed drop has radius distribution of $r_0(\phi)$ and subsequent images have distribution $r_i(\phi)$ up through the critical distribution $r_{\text{crit}}(\phi)$, from the last image captured before drop runback.

The initial and final contact lines are shown in Fig. 31 as a mean contact line and 1–σ variation for all wind-forced drops. The x- and z-coordinates of the contact line for each drop are normalized by $\langle r_0 \rangle$, the mean radius of the initial drop. For comparison, the same plot is made for all drops forced by gravity alone in Fig. 32. The final contact line for wind-forced drops has very nearly straight-line segments on the top and bottom, connected by approximately circular arcs. Bikerman (1950) observed circular arcs connected by parallel segments for gravity-forced drops. Bikerman's drops contracted in the spanwise direction before running downslope. Gravity forcing here produces a contact line with a circular segment of smaller radius at the downslope side than the upslope. These circular segments appear to be connected by straight lines and may have a slight curvature opposite to that of the initial contact line.

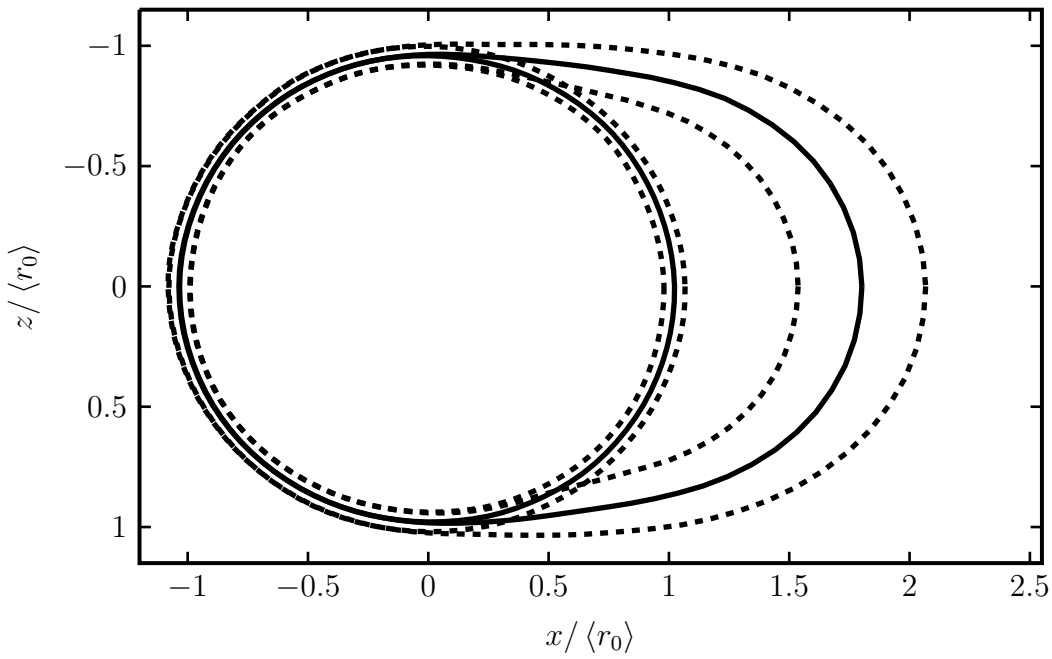

Fig. 31 : Mean and standard deviation of 182 wind-forced drop contact lines for initially placed sessile drops and the last sub-critical drop measurement. Drops range in volume from 15 μL to 350 μL and span the full range of α. Dashed lines show one standard deviation

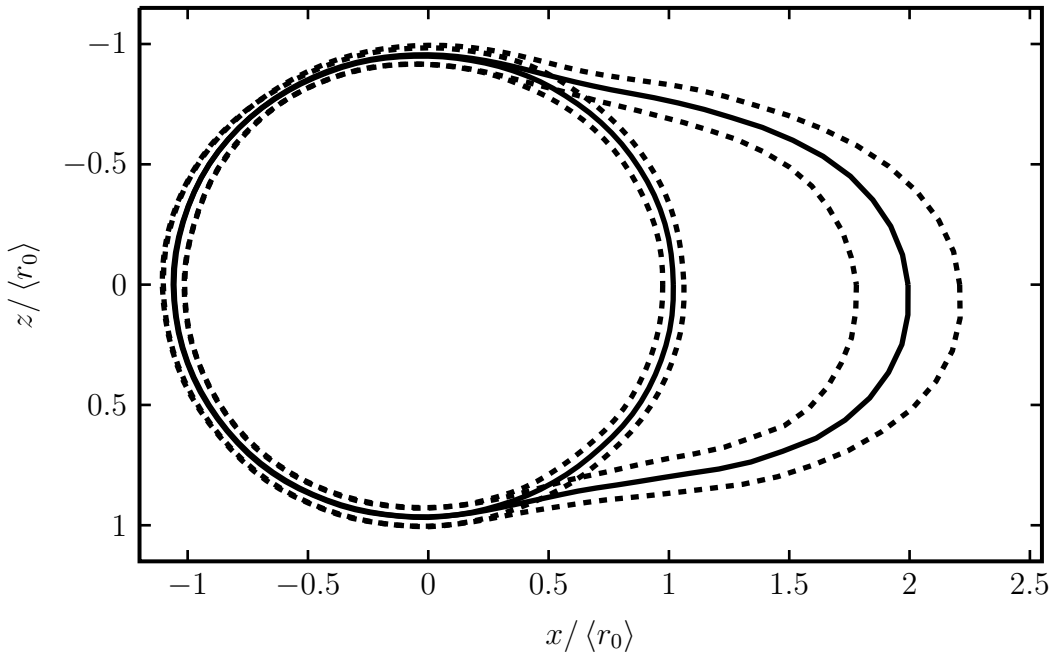

Fig. 32 : Mean and standard deviation of contact lines for 31 gravity-forced drops. The two solid curves are the initially placed sessile drops and the last sub-critical drop measurement. Dashed lines show one standard deviation

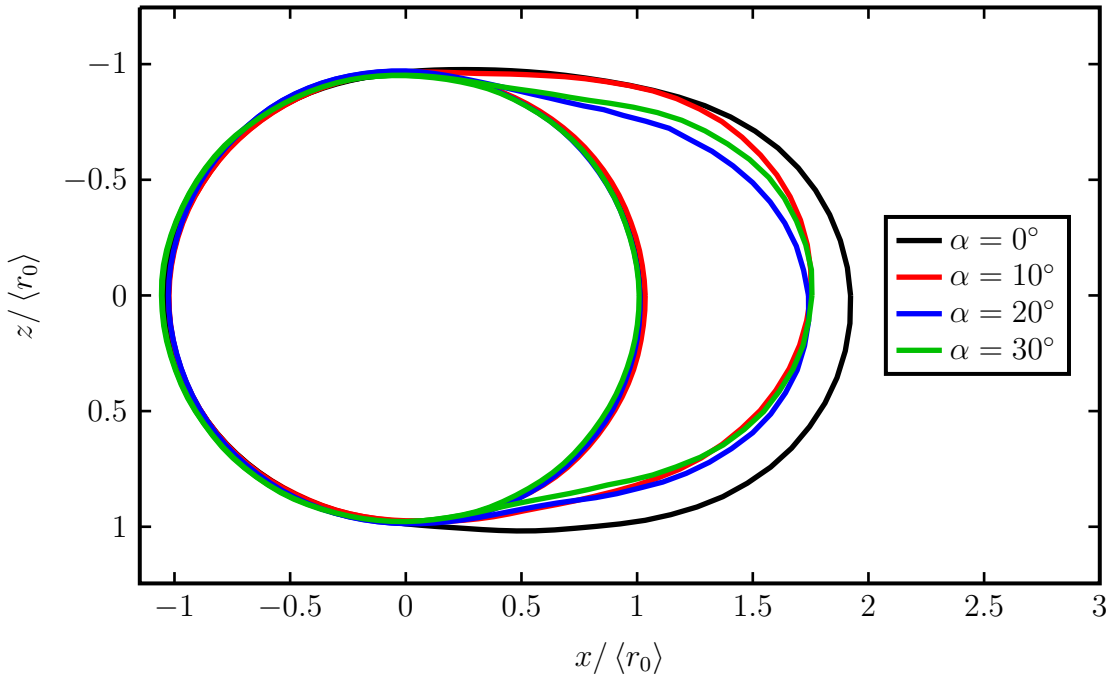

Fig. 33 : Variation of mean drop contact lines with inclination angle for wind-forced drops

To calculate which portions of the contact line have moved, first the quantity

$$\frac{r_i(\phi) - r_0(\phi)}{r_0(\phi)} \tag{4.2}$$

calculates the percent change in drop radius, with care taken to ensure the radius is sampled at a consistent set of ϕ values. All values of ϕ for which the radius ratio exceeds the empirically chosen threshold value of 2% are deemed to have moved. The first image in the sequence for which at least 20% of the contact line has moved (this prevents the occurrence of poor results due to misidentification of contact lines) is selected and the ϕ-extrema are recorded. The result of this process for an example drop are shown in Fig. 34. The ϕ values for the extents of first observed motion are shown in Fig. 35 in a histogram form. As a caveat, the lack of time resolution in data collection may present some trouble in correctly identifying the points of the contact line which first move.

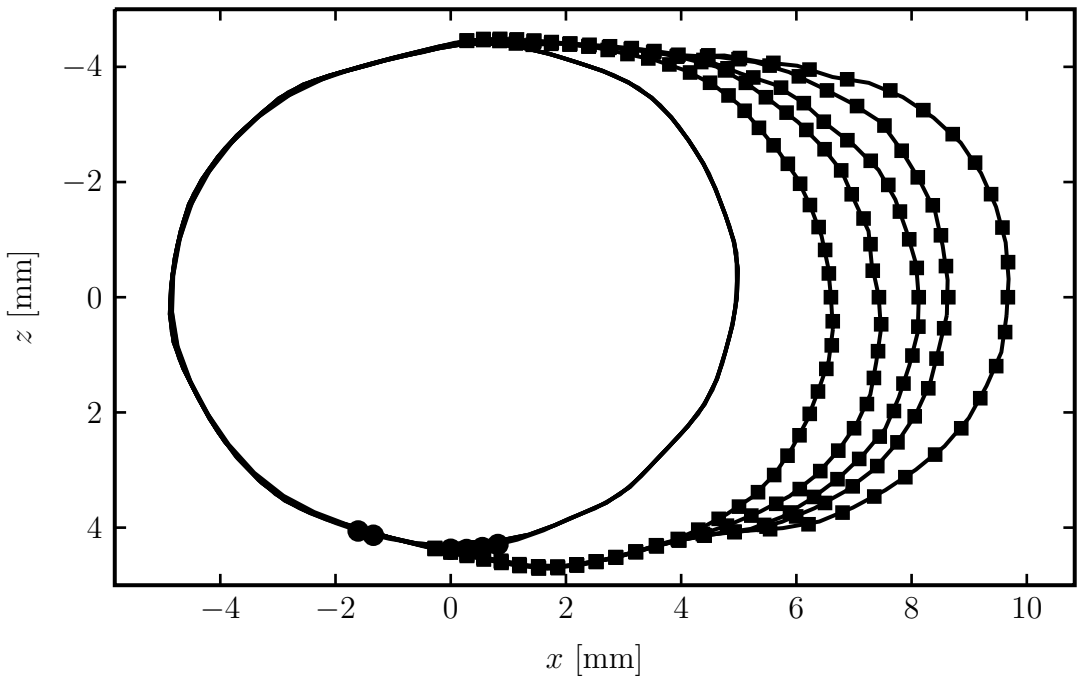

Fig. 34 : An example contact line evolution sequence with movement detection. The extent of contact line deemed to have moved is marked by squares. Circles mark detected, but rejected motion

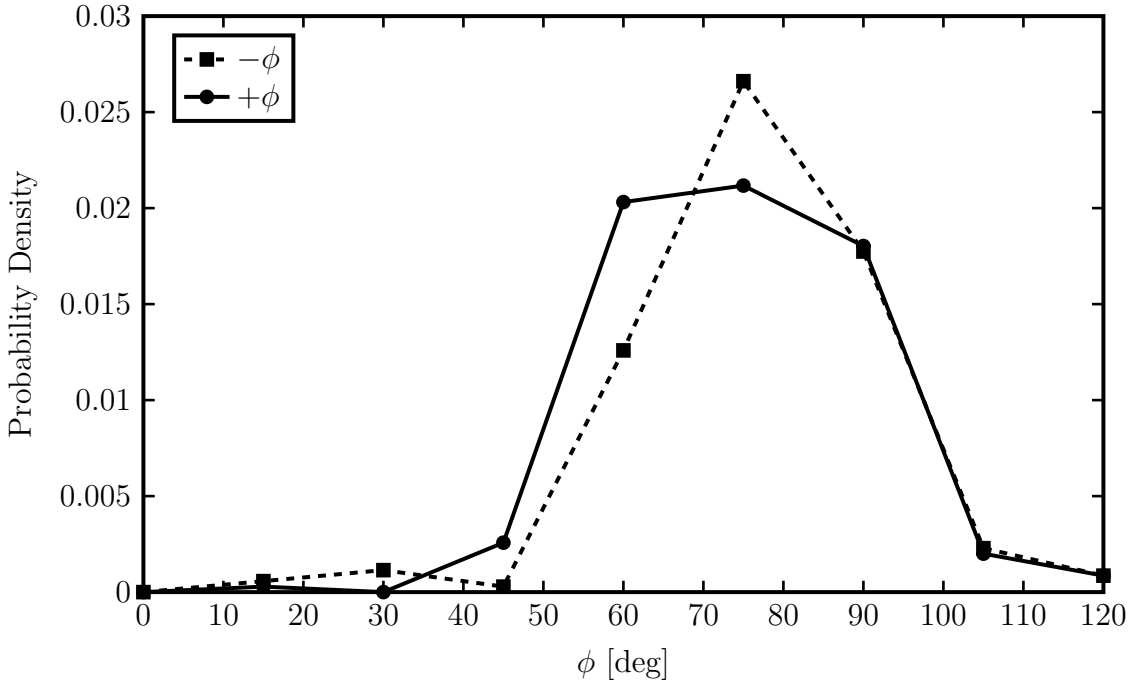

Fig. 35 : Histogram of ϕ values for the bounds of first significant contact line movement, split by the upper and lower portion of the drop

That the two histograms in Fig. 35 are nearly identical indicates the expected side-to-side symmetry as drops become unstable. The aggregate behavior is symmetric even while this is not necessarily true for each individual drop tested due to imperfect initial conditions. For this experimental configuration, the most likely location at which drop contact lines first become unstable is $\phi = \pm 75°$.

Inspecting the contact line instability more closely, Fig. 36 splits the ϕ values into four curves based on the surface inclination. Here it becomes apparent that the contact line motion begins differently for drops on an inclined surface than a level one. In most cases, drops placed on the surface and then inclined to 10, 20, or 30° experience elongation before the airflow begins. The smaller drops, however, are able to maintain their initial contact line shape for these inclinations. Gravity forcing initiates contact line motion between markedly smaller values of ϕ, as the histogram peaks move to smaller ϕ as surface inclination increases. For airflow forcing alone, the $\alpha = 0°$ condition in Fig. 36 shows the most likely bounds for contact line instability are $\pm 90°$, corresponding to the motion of all downstream portions of the contact line. These observations coincide with the contact line behavior in Fig. 31 and Fig. 32, where it is clear that the contact line of drops forced by gravity alone moves downstream with a narrower range of ϕ.

The extent to which the area wetted by the drop changes due to gravity forcing is shown in Fig. 37. Larger drops with smaller critical angles experience more spreading than smaller drops with large critical angles. This agrees well with data on drop length extension and width contraction in Table 3 of Bikerman (1950). Figures 38 and 39 show the relationship between wetted area ratio and the critical Reynolds and Weber numbers. For sub-critical gravity forcing combined with airflow, Fig. 40 shows the variation in wetted area as drop Reynolds number increases. In both cases, wetted area ratio at runback increases slightly with the increased flow speed. The area

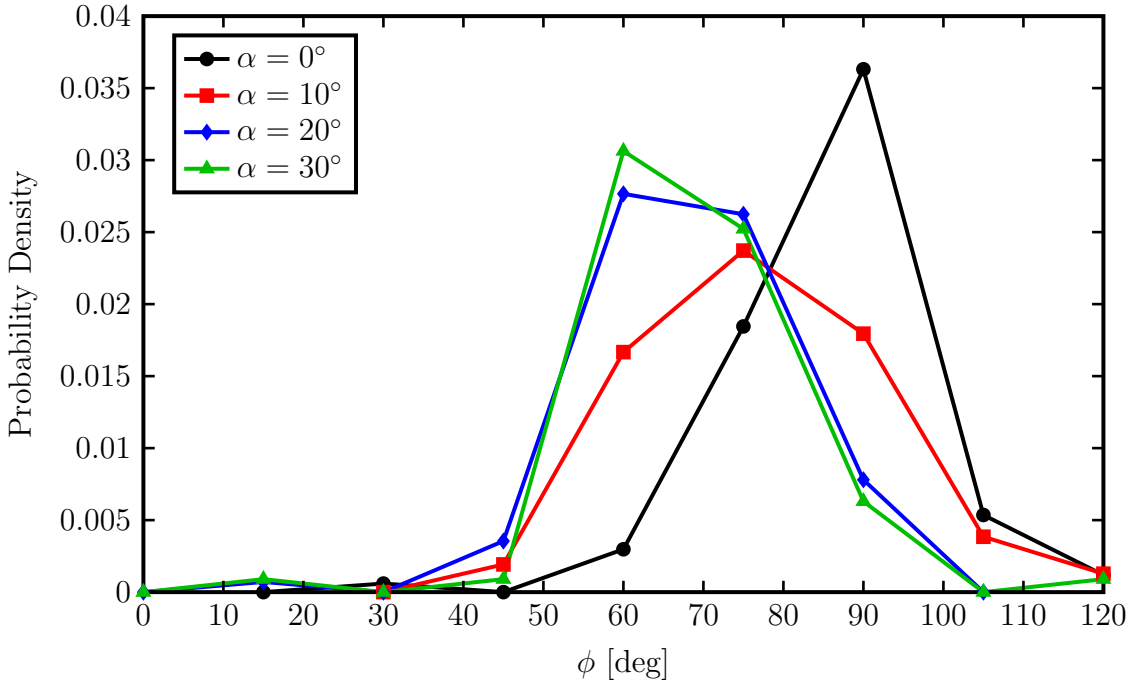

Fig. 36 : Histogram of ϕ values for the bounds of first significant contact line movement, split by inclination angle, α

enclosed by the drop's initial contact line is used to scale drop area for subsequent drop images. A Reynolds number for each measurement is calculated based on h from the empirical fit for drop height and U_∞, the freestream velocity for each drop measurement.

Ding and Spelt (2008) found the wetted area ratio at the runback threshold to be in the range of approximately 1.1–1.6, quite similar to that observed here. The area ratio is 1.42 for the mean wind-forced drop contact line shown in Fig. 31. The relationship with Reynolds number, however, behaves differently. Ding and Spelt (see Figure 11) found wetted area ratio to obey an exponential decay with increasing Reynolds number while the results here show no such trend. Ding and Spelt simulated Reynolds number up to 74.1, so this difference may be attributable to the relative effects of pressure and shear forcing in each case.

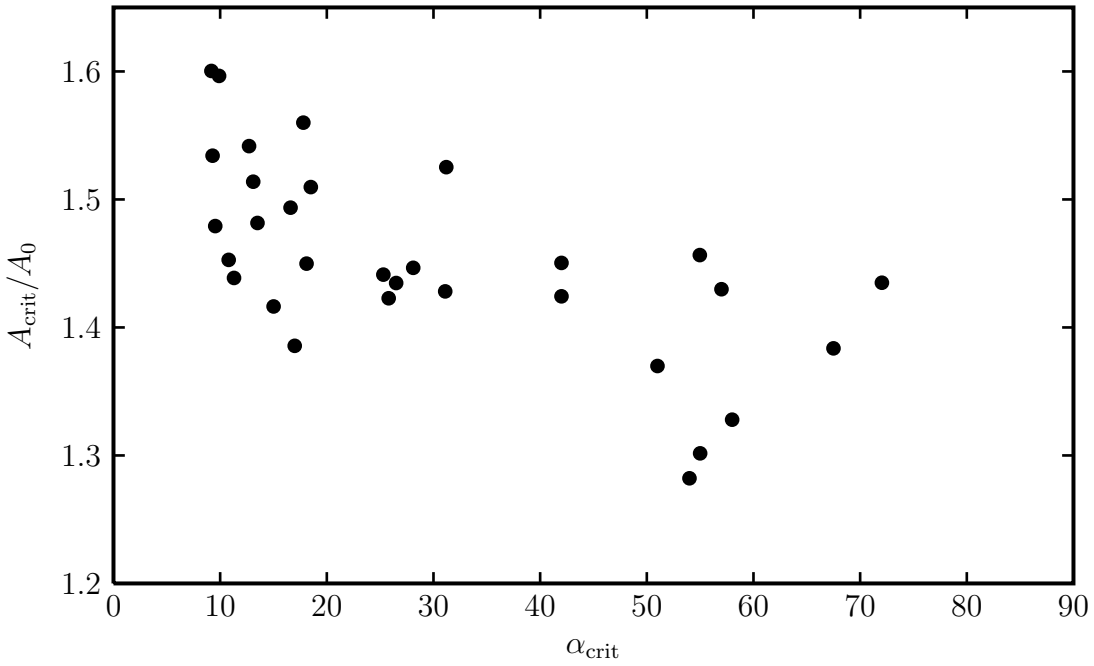

Fig. 37 : Ratio of wetted area at runback threshold to initially wetted area for gravity-forced drops

The variation of wetted area ratio is shown in Fig. 40 for every sub-critical measurement of all drops. The point size indicates drop volume. All drops begin at (0,1). Drops for which gravity forcing is first applied may or may not experience spreading before airflow is initiated. The $\alpha = 0°$ case clearly experiences the most spreading and highest Reynolds number. When forced by gravity and air, smaller drops seem to spread as much or more than larger drops at the same inclination. Drops with zero inclination experience minimal spreading until the Reynolds number is greater than about 1500. Conversely, drops with combined forcing tend to spread at a much lower Reynolds number.

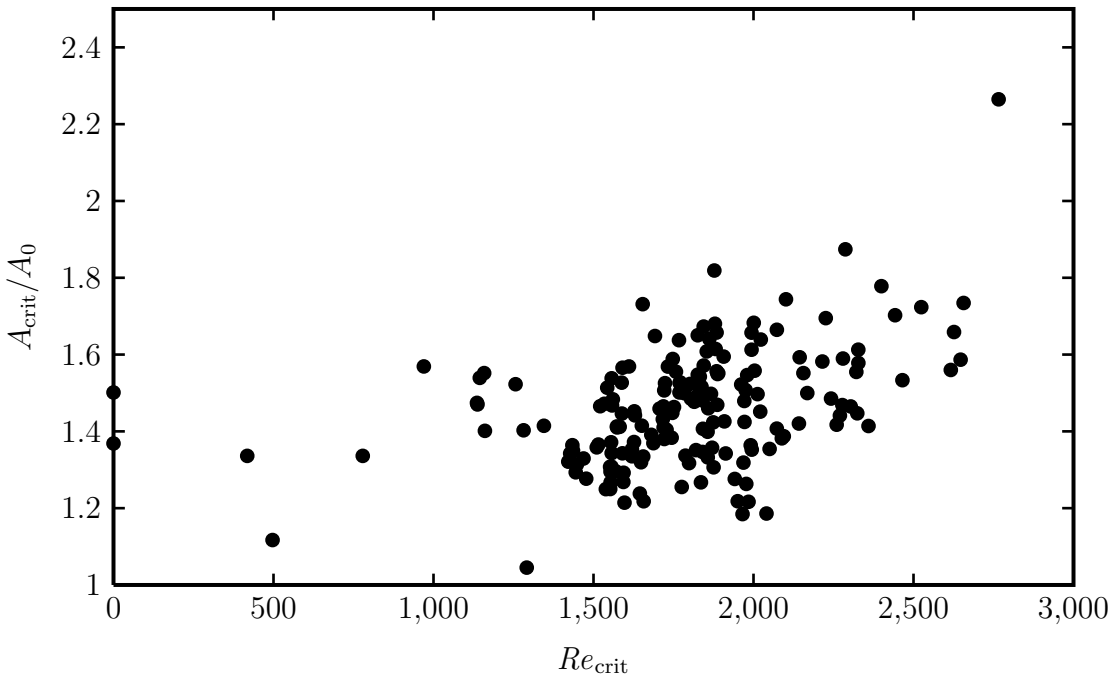

Fig. 38 : Ratio of wetted area at runback threshold to initially wetted area versus critical Reynolds number for wind-forced drops

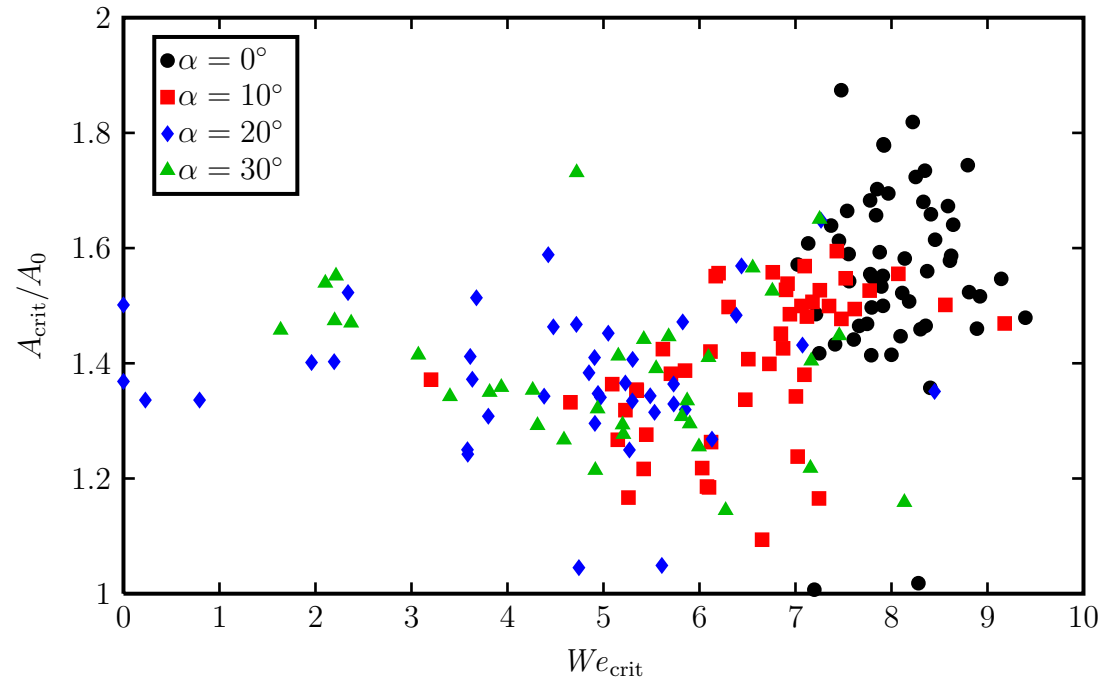

Fig. 39 : Ratio of wetted area at runback threshold to initially wetted area versus critical Weber number for wind-forced drops

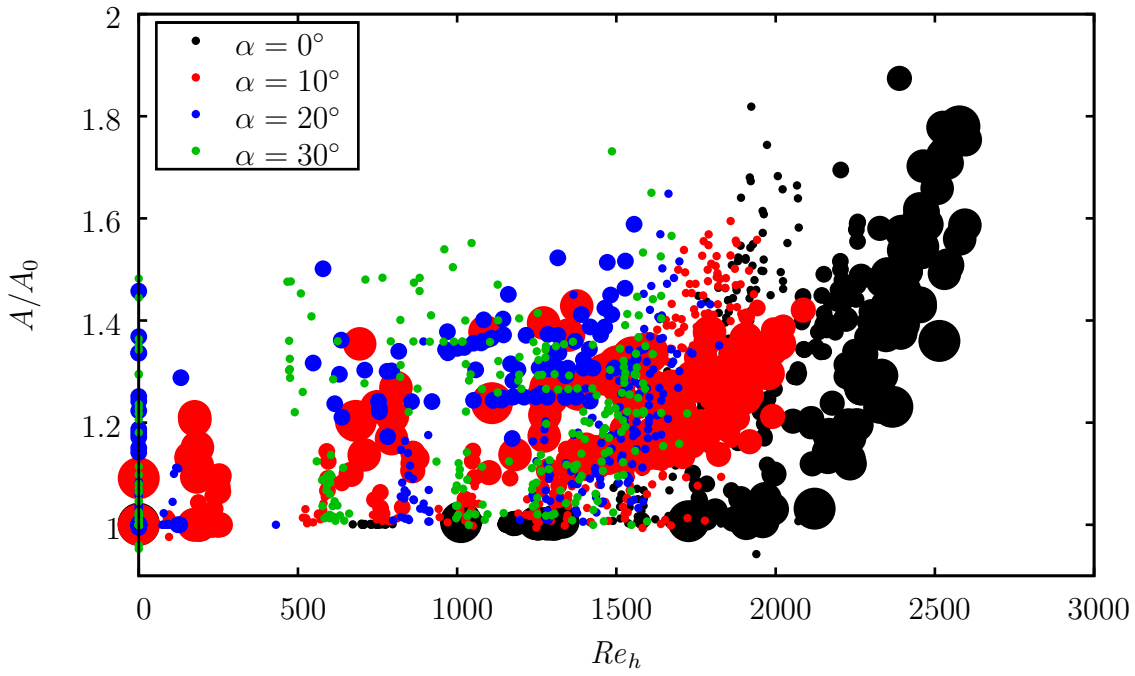

Fig. 40 : Area ratio variation with Reynolds number and drop volume. Drop height, h, is a constant for each drop, calculated from the drop height fit. Marker size is proportional to drop volume

2. Drop Shape Evolution

A sequence of sideview images captured for a typical drop experiment is shown in Fig. 41. Of particular interest in these images is the change in curvature of the upstream portion of the profile as the flow speed is increased. The pressure inside a sessile drop is higher than that of the surrounding fluid due to the force applied along the interface by surface tension. The sessile drop in the absence of gravity maintains a constant curvature and thus assumes a spherical cap shape. Airflow over the drop and the force of gravity combine to alter the pressure field both inside and outside the drop. The effects of these forces can be seen in the evolution of the drop profile.

Initial drop profiles take an approximately spherical cap shape when viewed from any direction. For example, Fig. 42 shows the initial line profile of all drops looking along the flow direction. At the runback threshold, the drops take on a significantly different profile, most notably from the side. The average reconstructed sideview drop profile is shown in Fig. 43 for each inclination angle. Both dimensions are normalized by the drop width at the runback threshold. The most interesting feature here is that drop profiles contain inflection points where the curvature changes sign.

Splitting the profiles up into groups based on both inclination angle and drop size relative to the Bond number threshold, Fig. 44 shows the final sub-critical reconstructed sideview profile. Dimensions are normalized by the drop width at the measured runback threshold. The profile and band displayed are the mean and standard deviation of a collection of drop profiles. Drops smaller than the slope discontinuity point in Fig. 17 possess a region of negative curvature on the upwind side of the drop. Larger drops whose stability limits have been shown to be dominated by the force of gravity (see Fig. 18) maintain configurations with curvature similar to the sessile drop case, with no sign changes in the curvature. In the hydrostatic configuration, the force exerted by

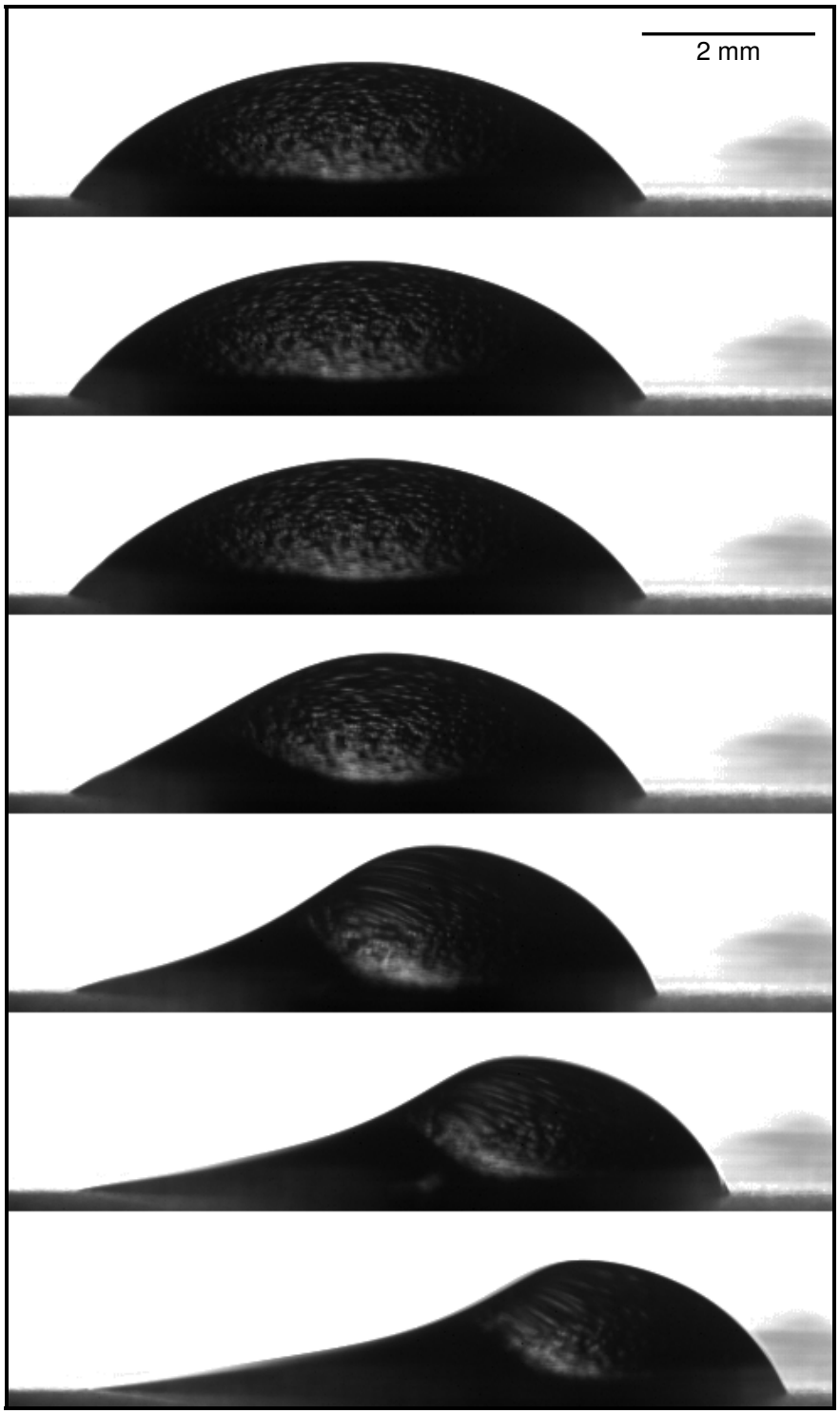

Fig. 41 : A typical sequence of sideview images from the initially sessile drop to the runback threshold. Test conditions were $\mathcal{V} = 50$ μL and $\alpha = 0°$. The critical flow speed was $U_{\text{crit}} = 17.7$ m/s

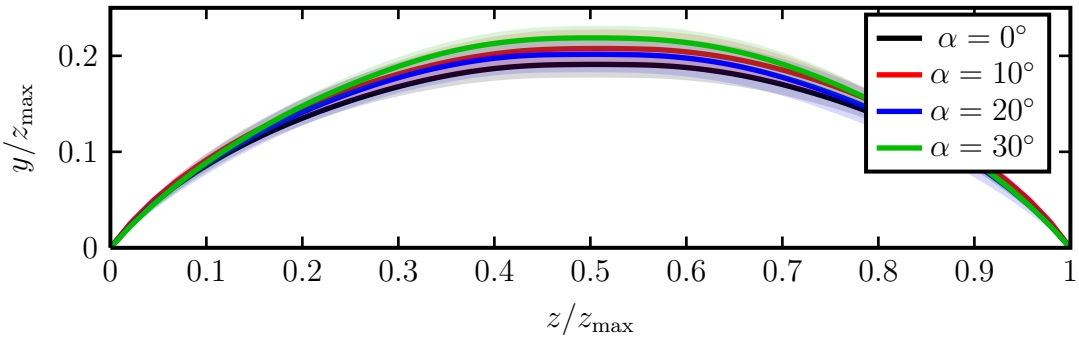

Fig. 42 : The initial frontal area projection of reconstructed drops, split by inclination angle

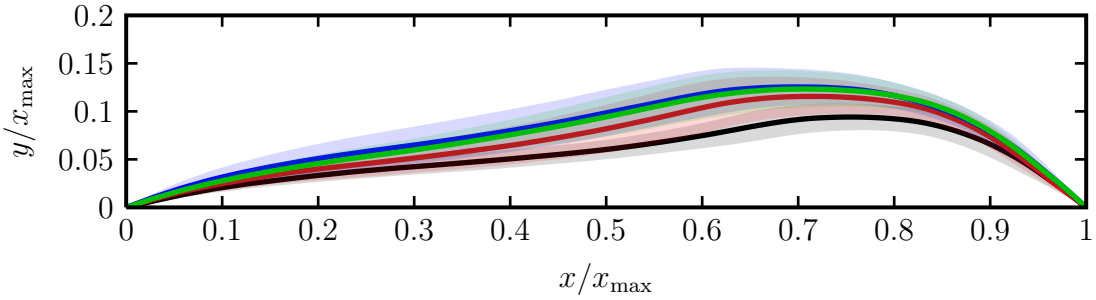

Fig. 43 : Mean of reconstructed sideview drop profiles split by inclination angle, α

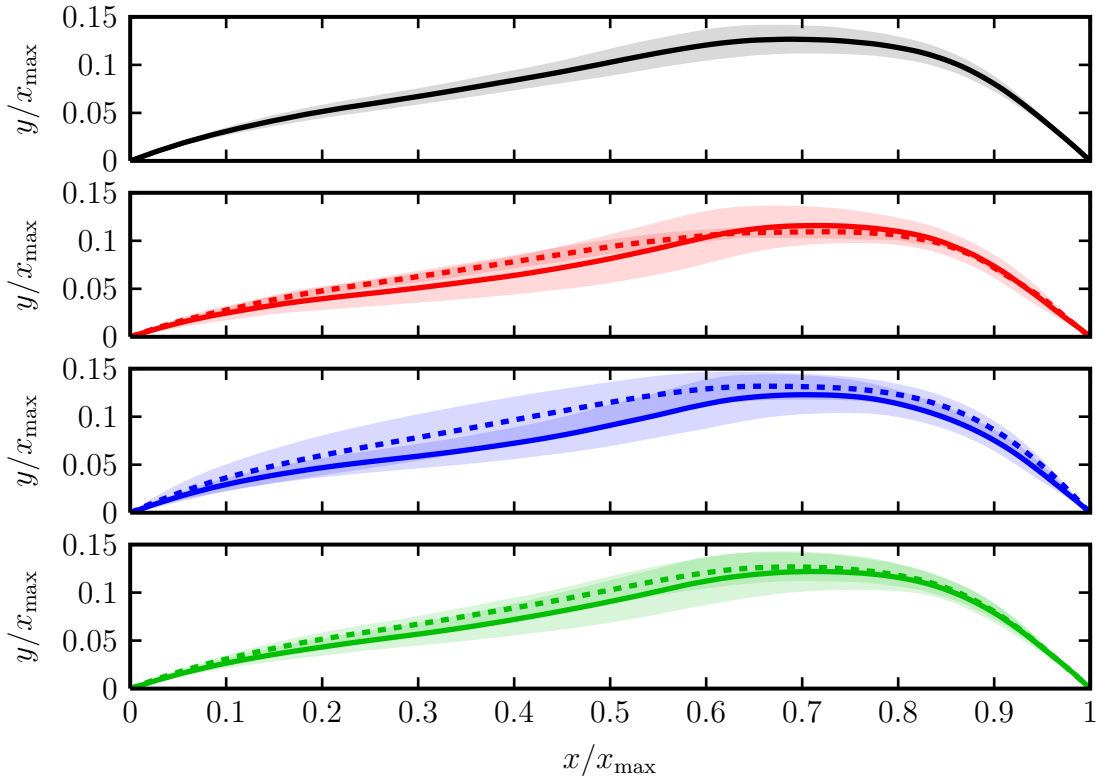

Fig. 44 : Final drop profiles, split by volume and inclination angle. Plots show inclination angles of $\alpha = 0°$, $10°$, $20°$, $30°$, beginning at the top. Drops smaller than the *Bo* threshold in Fig. 17 are shown with solid lines; larger drops are shown with dashed lines

surface tension due to the interface curvature resists the essentially uniform pressure field around the drop. For smaller drops where the stability limit is dominated by airflow effects, the complex pressure field surrounding the drop is responsible for the negative interface curvature on the upwind drop side.

Figure 45 shows the evolution of the volume of reconstructed drops normalized by the applied drop volume and demonstrates a clear decreasing trend for all inclination angles past about $U/U_{\text{crit}} = 0.5$. Two effects may be at work here. First, because the experiments take place in an open wind tunnel, evaporation may occur. The relative humidity in the room is less than 100%, so evaporation may be slightly to blame for decreasing drop volume as an experiment progresses over the course of about two minutes. Second, the drop reconstruction technique may be making consistenly low measurements of drop volumes. This idea is first corroborated by the initial drop volume at $U/U_{\text{crit}} = 0$, where reconstruction volumes range from about 70% to 90% of the applied drop volume. At larger flow velocities, the added complexity of reconstructing deformed drop shapes decreases further the reconstructed volume relative to the applied volume. Reconstruction inaccuracies are most likely the cause of underestimated volume, however, the relative importance of these two factors in decreasing drop volumes cannot be determined. This underestimation of drop volume is discussed further in the following section in conjuction with contact angle results.

3. Contact Angle Evolution

The measurement of full profile evolution sequences enables further exploration of the details of drop evolution and stability. Of particular interest is the evolution of the contact angle distribution.

Figure 46 shows the mean and standard deviation of contact angle for all drops measured in the last image before runback, split into groups by the inclination angle.

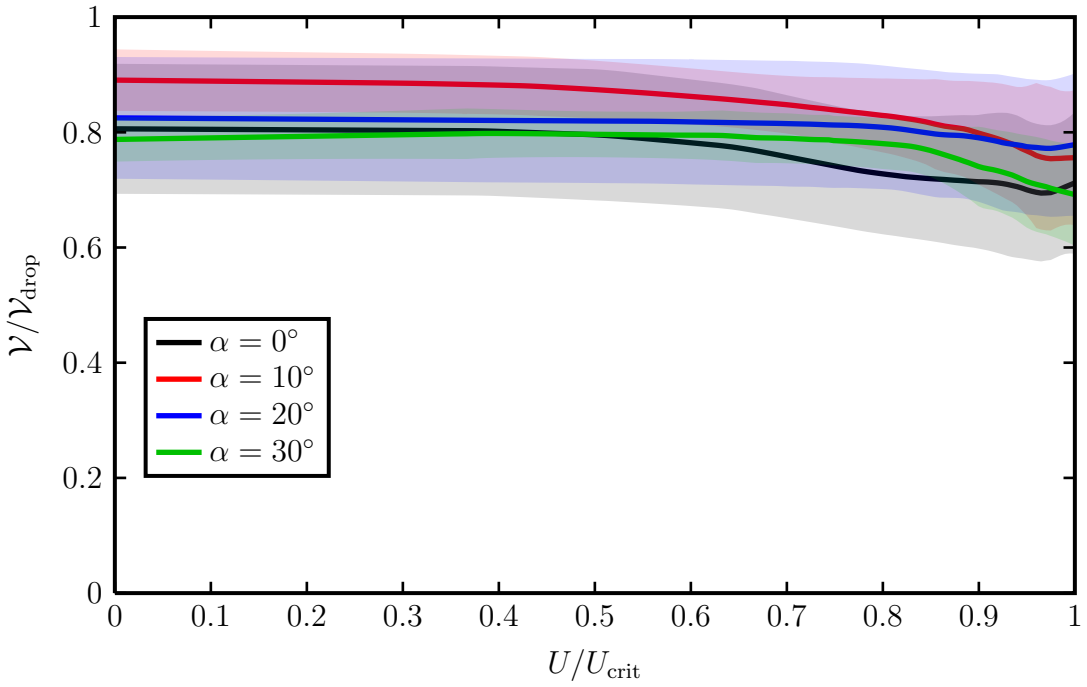

Fig. 45 : Reconstructed drop volume normalized by applied drop volume

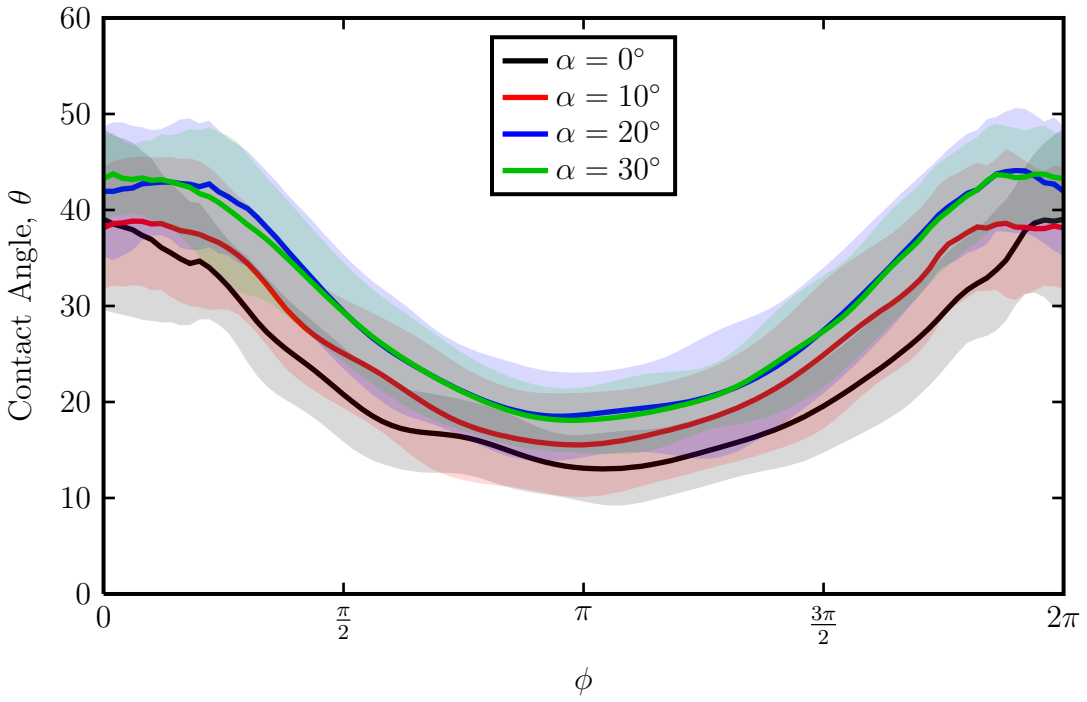

Fig. 46 : Contact angle distribution along the contact line for drops at incipient runback

The width of the "valley" in contact angle distribution depends on both the contact angle variation around the perimeter and the contact line shape. Dependence on contact line shape enters through the definition of the angle ϕ in a way such that drops that experience more spreading will exhibit a wider valley with contact angle near θ_{r} and a narrow peak near θ_{a}. This may factor into interpretation of the results here, particularly when contact angle distributions are averaged over many drops. Some of the highly smoothed nature of contact angle distributions seen in this section are a reflection of this averaging process. Averaging many distributions with sharp jumps at slightly different ϕ locations can produce a smooth distribution.

The distribution shape at runback (Fig. 46) is very similar for $\alpha = 10°$, $20°$, and $30°$, with a slight shift toward lower contact angles for the $\alpha = 10°$ case. The $\alpha = 0°$ case indeed exhibits the effect of more contact line spreading through the appearance of a wider valley in the distribution. Referring back to Fig. 33, greater spreading of $\alpha = 0°$ drops is the likely cause. Again, the error in these contact angle measurements is significant. Nevertheless, the observation that all contact angle distributions follow the same trends is an important one.

Figure 47 shows the evolution of contact angle distribution as the flow velocity is increased from $U = 0$ to U_{crit}. The standard deviation for the sample of drops at each flow velocity is shown as band of the same color about the mean contact angle distribution. While contact angle distributions are known across the whole range of U/U_{crit}, only five are shown to maintain visual clarity.

Initially placed drops have a fairly constant contact angle not only as expected, but also as observed in previous work by Schmucker et al. (2012). Distributions for $U/U_{\mathrm{crit}} = 0.25$ show the deformation by gravity of inclined drops before significant deformation by airflow begins. Then, as flow speed increases to U_{crit}, the contact angle decreases significantly on the upstream side of the drop, maintaining a smooth

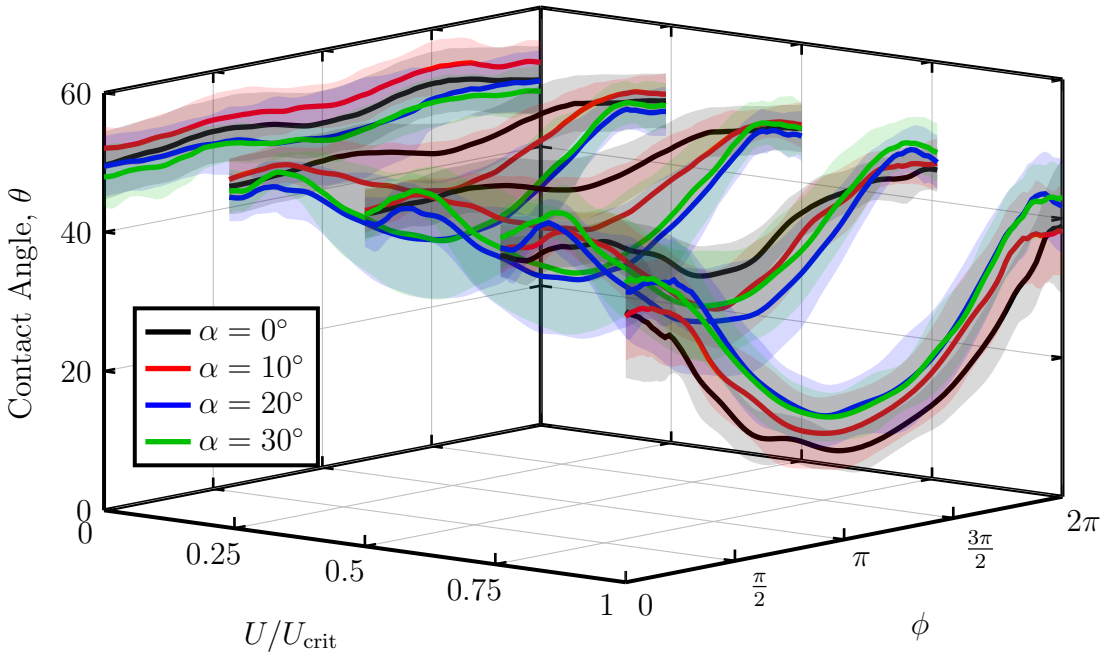

Fig. 47 : The evolution of mean contact angle distribution and its standard deviation along the contact line for all drops in the study, separated into groups by inclination angle. Contact angle distributions are shown for $U/U_{\text{crit}} = 0$, 0.25, 0.5, 0.75, 1

increase along the contact line toward the downstream side.

In Fig. 47, the distribution for each inclination angle encompasses drops of a wide range of volumes. Small drops experience much less deformation due to gravity than do larger drops at the same inclination angle. For inclination angles of 10° and 20° in particular, the portion of critical forcing supplied by gravity varies widely over the drop size range; this is the reason for the exceptionally large standard deviation for the $U/U_{\text{crit}} = 0.25$ and 0.5 curves.

For drops with gravity forcing, there are two measurements of a drop profile at $U/U_{\text{crit}} = 0$. The first is a measurement of the initially placed profile with zero downstream forcing. The second is a measurement with only gravity forcing when $\alpha > 0°$ and $U/U_{\text{crit}} = 0$. So, some deformation of drops by gravity occurs at $U/U_{\text{crit}} = 0$, which is shown in the first set of contact angle distribution data in Figures 48 to 51.

Figures 48 to 51 show more clearly the evolution of contact angle distribution of all drops. Each figure shows the evolution for a particular inclination angle. Within each figure, drops are grouped together whose stability behavior is deemed to be dominated by gravity or wind by the Bond number or volume threshold from Fig. 17. The $\alpha = 0°$ drops in Fig. 48 experience no gravity forcing and thus have no Bond number threshold. Instead, these drops were split into two groups by an arbitrary drop size threshold. Very little difference is observed between the contact angles of these two groups, implying drops subjected only to wind force experience very similar evolution with increased forcing.

Figures 49 to 51 demonstrate drops with combined gravity and wind forcing evolve in a significantly different manner depending on the relative influence of gravity and wind. Gravity dominated drops are shown with dashed lines and experience significant deformation due to gravity long before wind dominated drops achieve similar contact angle distributions. In fact, the contact angle distributions are dissimilar until $U = U_{\text{crit}}$, at which point the distributions match very well. To the extent which the measurements used here are able to discern, it seems drop configuration (specifically contact angle distribution) at the runback threshold is not dependent on the relative contributions of gravity and wind.

An inspection of Figures 46 to 51 shows the average reconstructed contact angle at the advancing edge of the drop is about 40°. However, from sideview images the true advancing contact angle was measured to be $\theta_{\text{a}} = 63.5° \pm 3.7°$. This difference is a manifestation of measurement error, which exists for several reasons. Chief among those is poor measurement of shift vectors on the grid ring adjacent to the contact line, which is a major cause of inaccuracy in drop profile measurements. Without accurate shift vectors to compare to a reconstructed profile in this region of the drop, the reconstruction algorithm has no information in the region and must simply guess

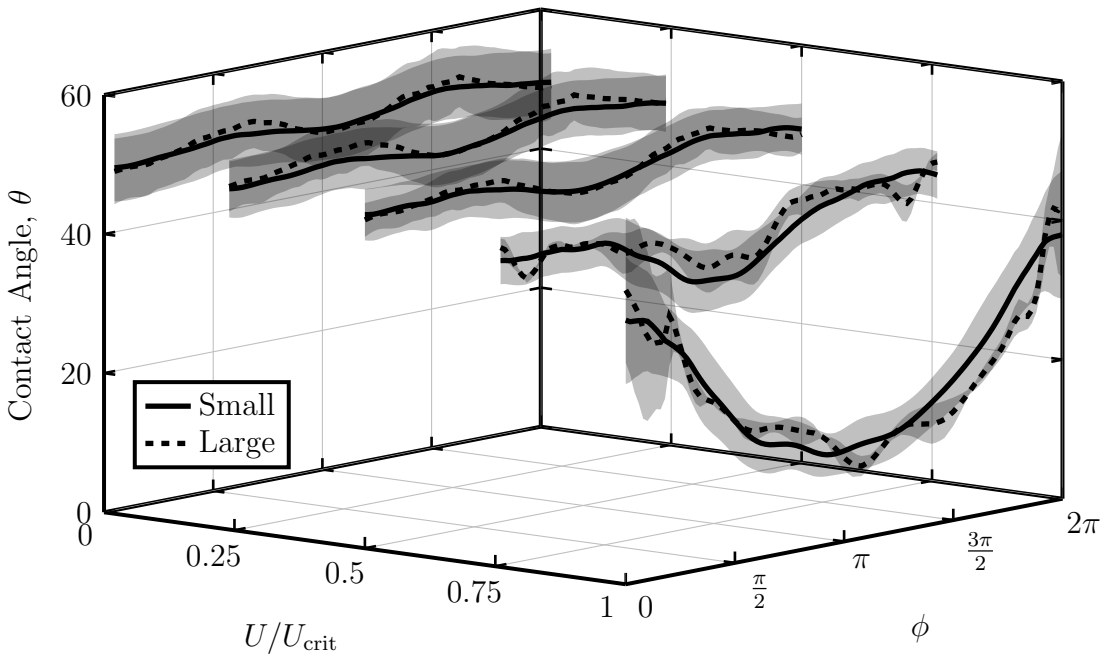

Fig. 48 : The evolution of mean contact angle distribution and its standard deviation along the contact line for all drops with inclination angle $\alpha = 0°$, split by drop size. Contact angle distributions are shown for $U/U_{\text{crit}} = 0$, 0.25, 0.5, 0.75, 1

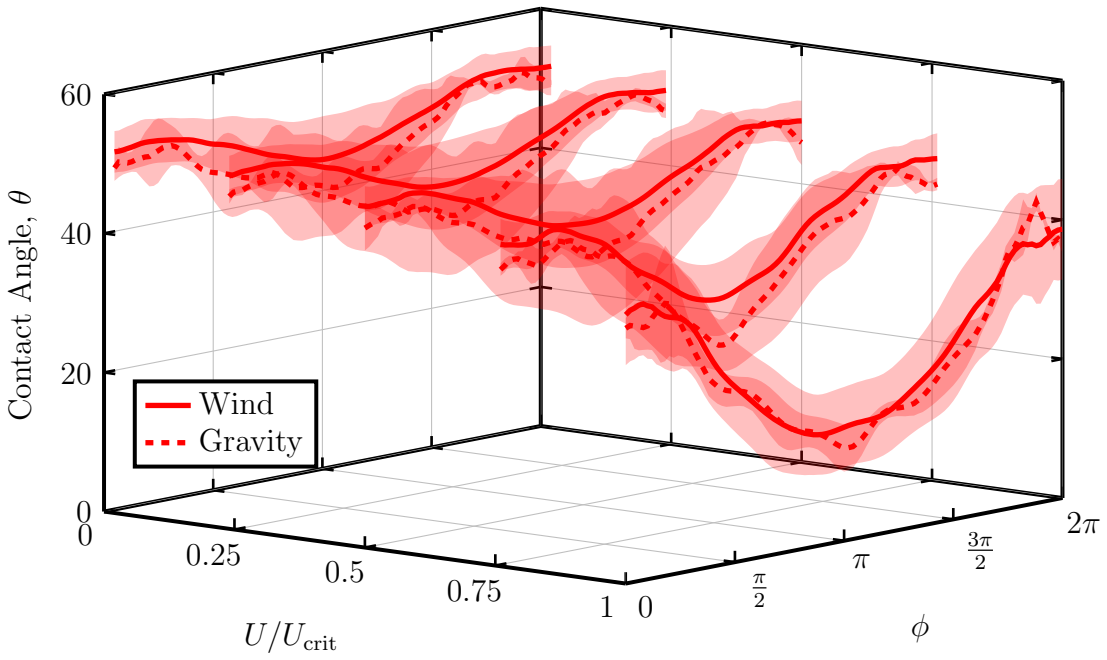

Fig. 49 : The evolution of mean contact angle distribution and its standard deviation along the contact line for all drops with inclination angle $\alpha = 10°$, split by *Bo* threshold. Contact angle distributions are shown for $U/U_{\text{crit}} = 0$, 0.25, 0.5, 0.75, 1

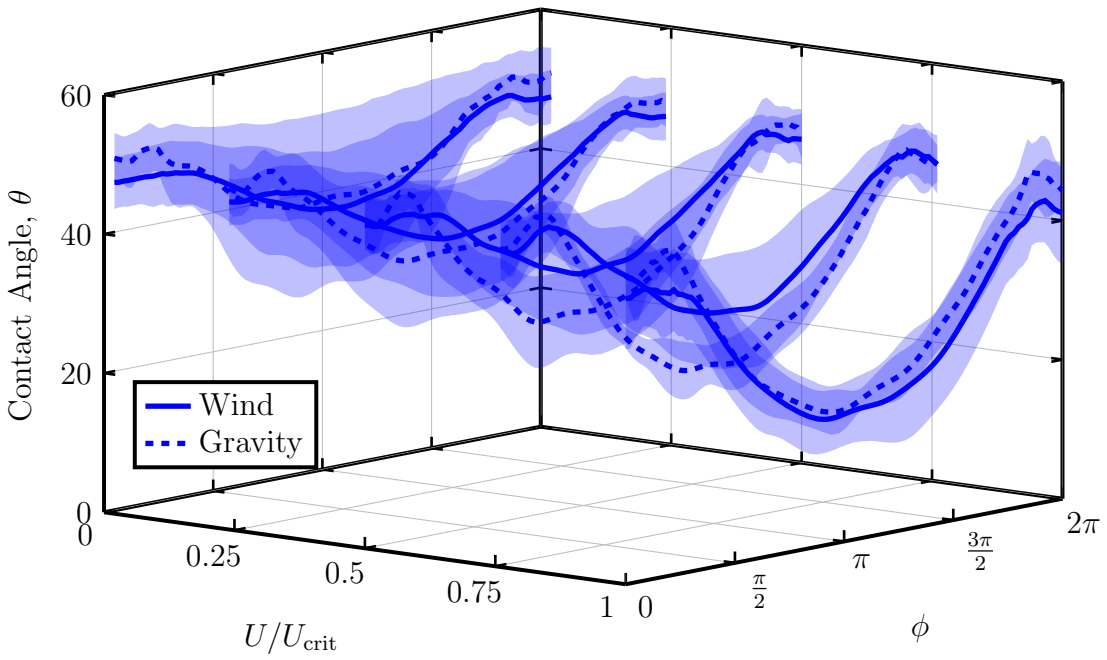

Fig. 50 : The evolution of mean contact angle distribution and its standard deviation along the contact line for all drops with inclination angle $\alpha = 20°$, split by *Bo* threshold. Contact angle distributions are shown for $U/U_{\text{crit}} = 0,\ 0.25,\ 0.5,\ 0.75,\ 1$

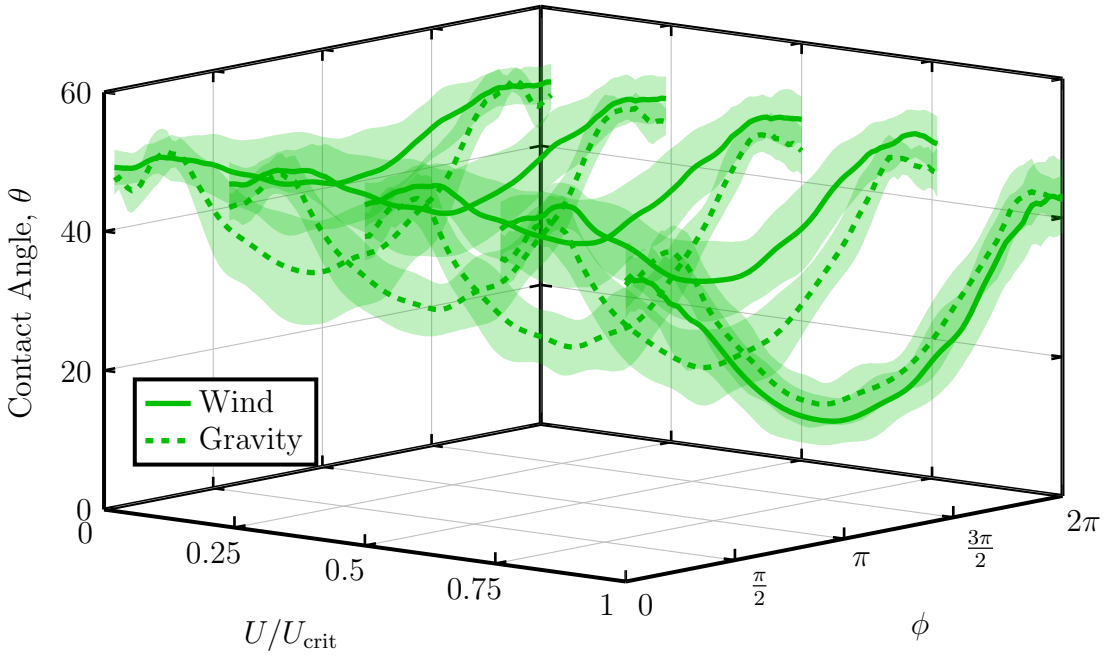

Fig. 51 : The evolution of mean contact angle distribution and its standard deviation along the contact line for all drops with inclination angle $\alpha = 30°$, split by *Bo* threshold. Contact angle distributions are shown for $U/U_{\text{crit}} = 0,\ 0.25,\ 0.5,\ 0.75,\ 1$

the contact angle. Thus, if the reconstruction underestimates the drop height at the first ring, the end result is affected in two important ways. First, and most obviously, the measured contact angle will be below its actual value. Second, the measured drop volume will be below its true value, as drop heights continue to be underestimated across the drop interior. For these reasons, the quantitative results presented here are not claimed to be highly accurate; rather, we propose the qualitative trends of overall drop behavior and evolution to be accurate and valid. Moreover, simulations of comparable drop stability conditions should not expect precise matching with qualitative results presented here.

4. Adhesion Force Evolution

Figure 52 shows the evolution of the contact line integral force as a function of flow speed. Both axes are normalized by the respective maximum for each drop so that all drops for a particular inclination angle may be plotted together. The solid lines represent the x- and z-components of the contact line force; the shaded bands surrounding them indicate the standard deviation of all drops in each sample.

In a broad qualitative sense, the trend of force evolution for $\alpha = 0°$ drops in Fig. 52 agrees with what is expected from scaling analysis. Basic aerodynamic principles dictate the drag force on a drop due to wind is proportional to U^2 (ignoring changes in drag coefficient due to drop shape change). And in general, the force evolution curves in Fig. 52 follow the expected trend of an initially slow force increase, followed by an increasingly steep change in force as the critical velocity nears. Past about 70% of U_{crit} the calculated contact line force increases much more quickly until it reaches its maximum value at the critical drop configuration. For the $\alpha = 0°$ curve in Fig. 52, the force evolution seems to almost follow a trend with two linear segments, the first from $U/U_{\text{crit}} = 0$ to 0.7, and the second from about $U/U_{\text{crit}} = 0.75$ to 1.0 with a connecting

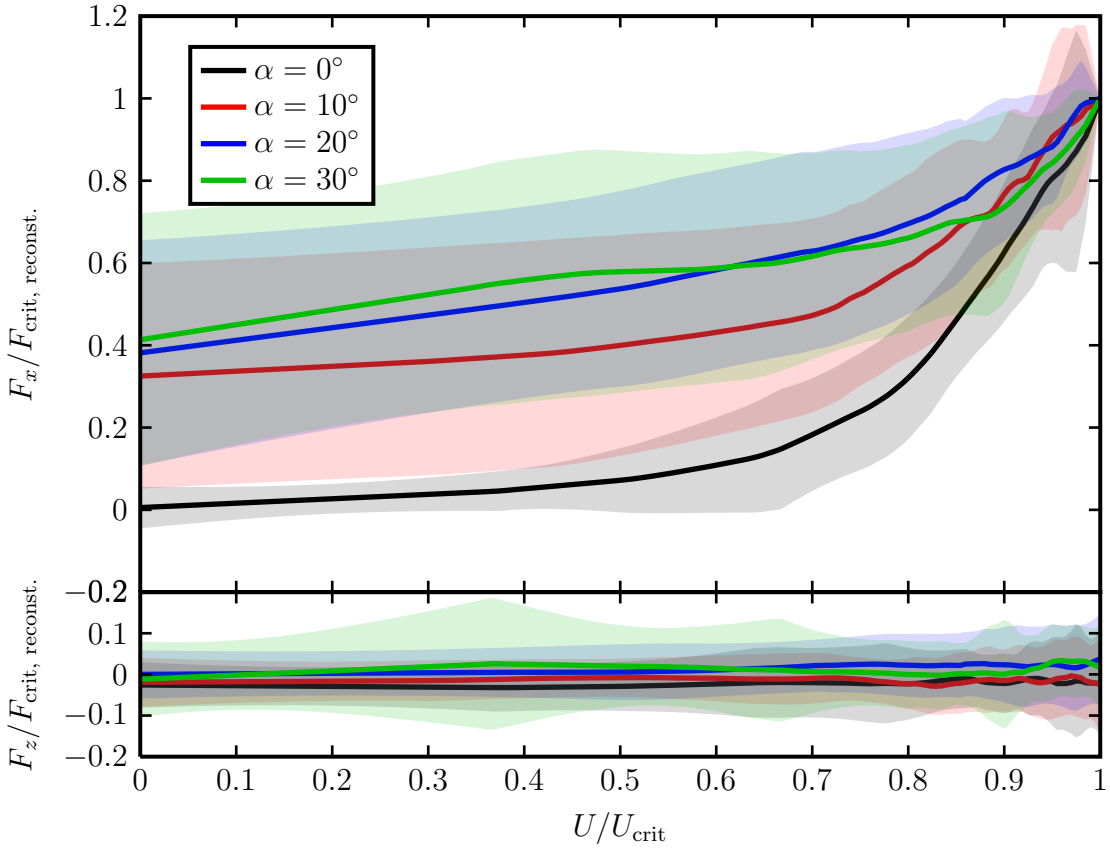

Fig. 52 : The evolution of contact line force components as a function of flow speed. Contact line forces are normalized by the final reconstructed force for each drop

curve between.

Scaling the force evolution by F_{crit} for each drop volume (calculated using $F_{\text{crit}} = mg \sin \alpha_{\text{crit}}$ and shown in Fig. 13) results in a force evolution curves of Fig. 53. It is evident a mismatch exists between the wind-forced drops and drops forced only by gravity. The measurements of contact line force for these wind-forced drops produce a critical force about 70–80% of the critical force under gravity alone. Figure 53 suggests that the maximum force indeed depends on the nature of the forcing and wind-forced drops have a forcing threshold 20% lower than drops forced by gravity alone. However, it is likely this behavior is simply the result of measurement error and the contact line integral method of drop reconstruction simply under-predicts the

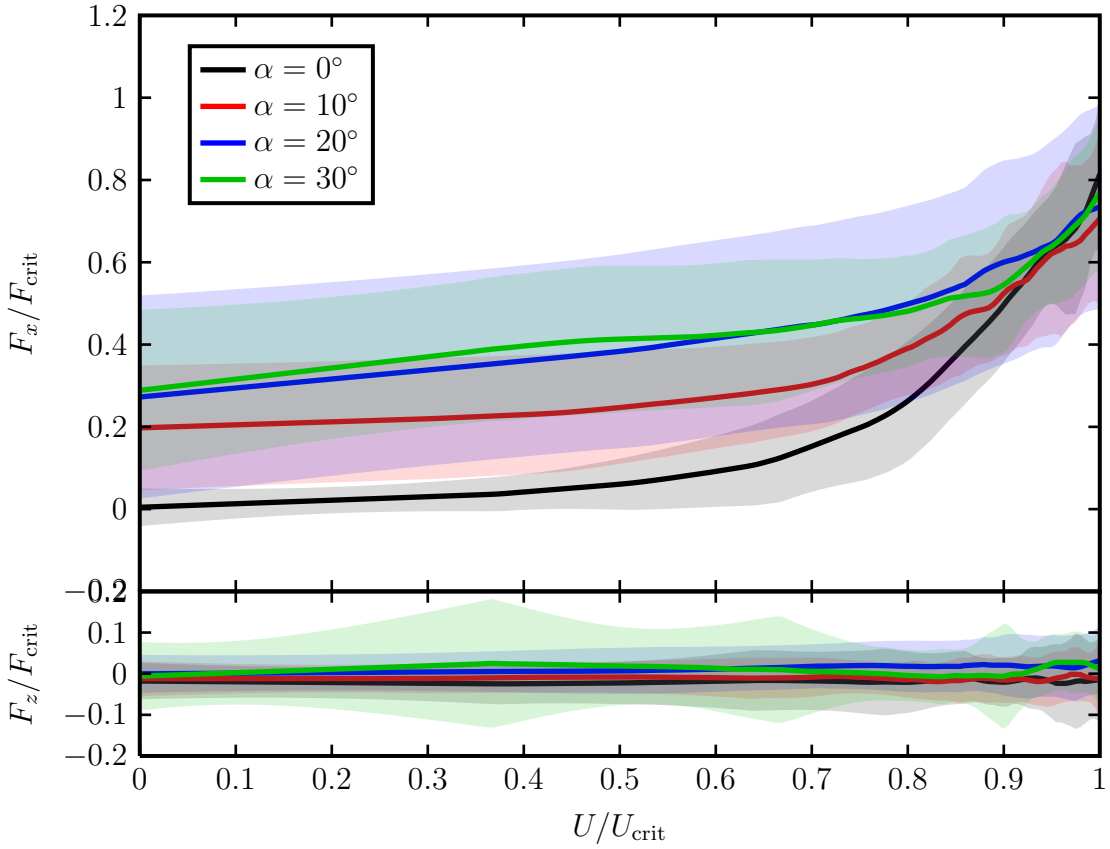

Fig. 53 : The evolution of contact line force components as a function of flow speed. Contact line forces are normalized by the critical gravity force of a drop of equal size (from Fig. 13)

adhesion force of critically wind-forced drops. Supporting this idea is the fact that the drop reconstructions produce contact angle distributions that do not span the full known range of contact angle between θ_{a} and θ_{r}, which are known to be the maximum and minimum allowable contact angles for these quasi-static drops. Furthermore, the integral contact line force was calculated for reconstruction of gravity-forced drops to be $72\% \pm 9\%$ of F_{crit}. So within their respective error bounds, contact line force integrals for both gravity and combined forcing produce equivalent answers. Thus, the mismatch is explained by measurement error. Furthermore, that critical contact line forces are about 20% below their true value is attributable to the result in the previous section that the measurement technique is underestimating the contact angle on the advancing side of the drops.

Returning to the scaling equation for the force applied by air, $F_{\mathrm{air}} = \frac{1}{2}\rho C_D A U^2$, we can attempt to gain insight into how drop shape deformations change the drag coefficient. The complex nature of a drop's interaction with the boundary layer is ignored in this equation. Instead, the freestream speed is used as the reference velocity. The product $C_D A$ is a composite indicator of the effects of drop shape on the drag force. The evolution of this quantity for drops forced only by wind is shown in Fig. 54. The plot range is limited to U greater than 20% of U_{crit} because the quantity is very sensitive to measurement noise at low flow speeds.

As the flow velocity initially increases from 0 m/s, the drop is able to significantly lower $C_D A$ and maintain a low level of forcing. This corresponds to the relatively flat part of the curves in Figures 52 to 53. After achieving its minimal value in the range $U/U_{\mathrm{crit}} = 0.5$ to 0.7, $C_D A$ begins to steadily increase and F_x does likewise. In this region, the drop is no longer able to adjust its shape sufficiently to account for the increasing flow speed (for example, see Fig. 21), and fluid begins to accumulate in the downstream portion of the contact area. From $U/U_{\mathrm{crit}} = 0.7$ to 1.0, $C_D A$ increases

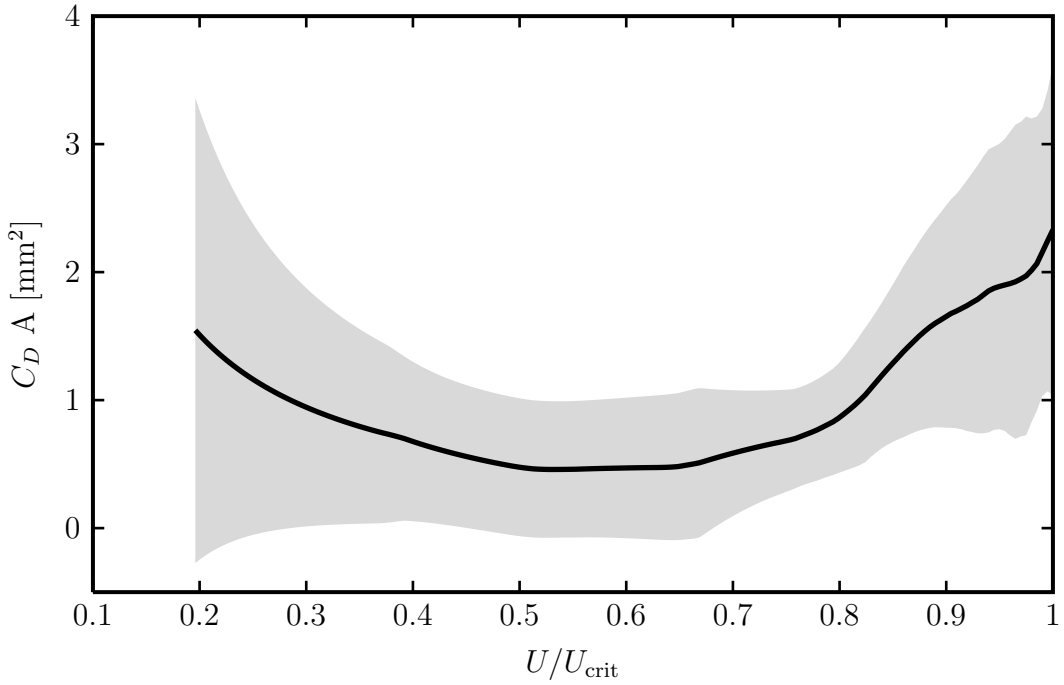

Fig. 54 : Evolution of the product $C_D A$ governing the drag force on a drop.

rapidly, producing a rise in F_x more steep than the expected U^2 dependence.

CHAPTER V

SUMMARY, CONCLUSIONS & FUTURE WORK

A. Summary

This dissertation presents the results of a series of experiments on the stability of water drops to combined gravity and wind forcing. Drops on surfaces experiencing airflow occur in wide-ranging applications, from heat exchangers and fuel cells to industrial coating processes and ice accretion on aircraft. Identification and understanding of when drops remain stationary or move along the surface is important in predicting their behavior and the overall behavior of a larger system such as an airfoil in icing conditions. The contact angle, contact angle hysteresis, and the phenomena of adhesion and wetting play crucial roles in determining the ability of a drop to adhere to a surface. Some computational studies of this process are found in the scientific literature, however, they have received little experimental validation. The difficulty of making detailed measurements of drop shapes has been mostly responsible for this lack of validation.

The novelty of the research presented here is in the application of a drop profile measurement technique capable of producing a full three-dimensional reconstruction of the drop profile from only topview images of the drop. The technique is based on the refraction of light rays at the drop interface, a process that causes the speckle pattern characteristic of the rough surface to be distorted by the lensing effect of the drop. The speckle shift vector field is measured through cross-correlation of image subregions centered on nodes of an elliptic grid constructed within the detected contact line. The drop shape is represented as a sum of a spherical cap and Bessel–Fourier series modes.

A simulated annealing algorithm is then applied to find the drop shape by minimizing the difference between the shift vector field of the reconstructed drop shape and the measured vector field.

An experimental rig was designed and built to provide a combination of gravity (through tilting) and wind forcing. Topview and sideview cameras collected a series of images of the drops as they were brought to criticality, beyond which the contact line is unable to remain pinned and the drops begin to run downstream.

On the wind tunnel floor was placed a sandblasted aluminum sample with average roughness $R_A = 3.26$ μm. Drops in the volume range of 15 μL to 400 μL were applied to the surface sample. The apparatus was then inclined to angles of 0°, 10°, 20°, and 30° and subsequently the flow was increased until drop runback. This stability experiment was repeated for a sample of 235 drops. An average of 9 drop images and forcing measurements were captured for each drop before runback.

B. Conclusions

Drops for $\alpha = 0°$ were found to have a constant runback threshold, $We = 8.0 \pm 0.5$. For combined gravity and wind forcing, the runback threshold followed a decreasing linear trend which takes a sharp turn toward zero Weber number once less than 20% of the critical forcing remains to be added by airflow.

The evolution of a drop contact line with increased forcing was investigated. It was found that drops with $\alpha = 0°$ are most likely to experience contact line motion on the entire downstream portion of the contact line while the upstream portion experiences motion only at runback. Drops first inclined to $\alpha > 0°$ before initiation of airflow were observed to experience contact line motion in a narrower region of the downstream contact line.

Reconstructed sideview profiles and full 3D profiles were used to demonstrate another significant difference in wind- versus gravity-dominated drop behavior. Drops in the wind-dominated regime contain a region of negative curvature on the upstream side of the drop due to the force of the flow through increased pressure. Gravity-dominated drops exhibit no such characteristics and instead maintain positive curvature throughout much like a simple sessile drop.

Full drop profiles were used to calculate the distribution of contact angle along the contact line. The evolution of contact angle distribution with increasing flow velocity was shown for various drop size ranges and inclination angles. Increasing inclination angle imparts significant drop deformation at an earlier point along a drop's evolution toward runback. Gravity- and wind-dominated drops were found to have nearly identical distributions at criticality, but take much different paths to arrive there.

The adhesion force due to surface tension was seen to evolve in a manner mostly consistent with scaling analysis predictions. Deviations from a quadratic relationship between flow velocity and drag force can be explained by the deformation of the drop shape and commensurate changes in drop area, drop shape, and accordingly, drag coefficient.

The qualitative usefulness of these results was seen to exceed the quantitative accuracy. Drop volumes were underestimated by the profile reconstruction technique and measured contact angles did not achieve the expected extrema of θ_{a} and θ_{r}. Several reasons for this were presented and the hypothesis put forth that these new observations of drop behaviors and evolution trends are useful for validation of future simulations even though the quantitative data are not.

The rig was designed to combine gravity and wind forcing so that drops could be brought to critical conditions with low Reynolds number by the application of

sub-critical gravity forcing. This was done with the intention of comparing to current numerical simulations of drop stability over a matched range of parameters, particularly Reynolds and Weber numbers. In practice, however, it remained quite difficult to achieve runback with Reynolds numbers as low as current simulations. Moreover, it has been demonstrated that gravity forcing produces a significantly different pattern of drop evolution than that seen under wind forcing alone. Drop profile shapes, contact angle distributions, and contact line forces were seen to behave quite differently under the varying test conditions. Therefore, it cannot be recommended to extrapolate the combined forcing results outside the used parameter range or to use combined forcing results to predict behavior of drops forced by airflow alone.

C. Future Work

As discussed in Chapter IV, results of Dimitrakopoulos and Higdon (1998) led to the hypothesis that drop behavior depends on the initial contact angle, which can naturally take any value between θ_a and θ_r. Specifically, they found dramatic variation in the contact line evolution. Most drops here were placed in a manner such that their initial contact angle is much closer to θ_a. Thus, these experiments made no effort to investigate the effect of this initial condition on the stability limits or drop shape evolution. However, this remains an open question to answered by experiment.

This research focused on one specific combination of working fluid and surface. The combination of water, air and surface sample used in this research had hysteresis $\Delta\theta = 55°$. As such, it made no attempt to identify the influence of surface roughness or varying contact angle hysteresis. Hysteresis is widely considered the single most important factor in drop stability, so future application of drop profile measurement method should attempt to understand the effects of different combinations of equi-

librium contact angle and contact angle hysteresis. This will broaden the scope of knowledge and seek to develop more universal understanding of the stability of drops to wind forcing. The ability to predict drop runback thresholds for use in engineering simulation and product design is highly coveted.

Furthermore, it must be mentioned that the results here are most likely specific to this particular setup. Application of stability thresholds in predictive simulations should be based on experiments closely matched to the expected conditions. Further research is required to bring to light the universal drop stability behavior across the full range of conditions under which the problem is relevant.

The research presented in this dissertation has applied a three-dimensional drop profile measurement to the wind-forced drop stability problem on a rough surface. Experiments of this type have not previously existed. This research provides new data on the stability limits of drops on rough surfaces and the way a drop responds to and resists increased forcing until it is no longer able and begins to run back along the surface.

REFERENCES

Acarlar MS, Smith CR (1987) A study of hairpin vortices in a laminar boundary layer. Part 1. Hairpin vortices generated by a hemisphere protuberance. J Fluid Mech 175(1):1–41

Barlow J (1999) Low-Speed Wind Tunnel Testing. Wiley, New York

Bikerman JJ (1950) Sliding of drops from surfaces of different roughnesses. J Colloid Sci 5(4):349–359

Cebeci T, Kafyeke F (2003) Aircraft icing. Annu Rev of Fluid Mech 35(1):11–21

Dimitrakopoulos P (2007) Deformation of a droplet adhering to a solid surface in shear flow: onset of interfacial sliding. J Fluid Mech 580(1):451–466

Dimitrakopoulos P, Higdon JJL (1997) Displacement of fluid droplets from solid surfaces in low-Reynolds-number shear flows. J Fluid Mech 336(1):351–378

Dimitrakopoulos P, Higdon JJL (1998) On the displacement of three-dimensional fluid droplets from solid surfaces in low-Reynolds-number shear flows. J Fluid Mech 377(1):189–222

Dimitrakopoulos P, Higdon JJL (1999) On the gravitational displacement of three-dimensional fluid droplets from inclined solid surfaces. J Fluid Mech 395:181–209

Ding H, Spelt PD (2008) Onset of motion of a three-dimensional droplet on a wall in shear flow at moderate Reynolds numbers. J Fluid Mech 599(1):341–362

Durbin PA (1988) On the wind force needed to dislodge a drop adhered to a surface. J Fluid Mech Digit Arch 196(1):205–222

Dussan V EB (1976) The moving contact line: the slip boundary condition. J Fluid Mech Digit Arch 77(04):665–684

Dussan V EB (1985) On the ability of drops or bubbles to stick to non-horizontal surfaces of solids. Part 2. Small drops or bubbles having contact angles of arbitrary size. J Fluid Mech Digit Arch 151(1):1–20

Dussan V EB (1987) On the ability of drops to stick to surfaces of solids. Part 3. The influences of the motion of the surrounding fluid on dislodging drops. J Fluid Mech Digit Arch 174(1):381–397

Dussan V EB, Chow RTP (1983) On the ability of drops or bubbles to stick to non-horizontal surfaces of solids. J Fluid Mech Digit Arch 137(1):1–29

Dussan V EB, Davis SH (1974) On the motion of a fluid-fluid interface along a solid surface. J Fluid Mech Digit Arch 65(01):71–95

ElSherbini A, Jacobi A (2004a) Liquid drops on vertical and inclined surfaces: I. An experimental study of drop geometry. J Colloid Interface Sci 273(2):556 – 565

ElSherbini A, Jacobi A (2004b) Liquid drops on vertical and inclined surfaces: II. A method for approximating drop shapes. J Colloid Interf Sci 273(2):566 – 575

Extrand CW, Kumagai Y (1995) Liquid drops on an inclined plane: The relation between contact angles, drop shape, and retentive force. J Colloid Interf Sci 170(2):515–521

Feng JQ, Basaran OA (1994) Shear flow over a translationally symmetric cylindrical bubble pinned on a slot in a plane wall. J Fluid Mech 275:351–378

Furmidge CGL (1962) Studies at phase interfaces. I. The sliding of liquid drops on solid surfaces and a theory for spray retention. J Colloid Sci 17(4):309–324

de Gennes PG (1985) Wetting: statics and dynamics. Rev Mod Phys 57:827–863

Hoffman KA, Chiang ST (2000) Computational Fluid Dynamics, vol 1. Engineering Education Systems

Johansson AV, Alfredsson PH (1982) On the structure of turbulent channel flow. J Fluid Mech 122:295–314

Kandlikar SG, Steinke ME (2002) Contact angles and interface behavior during rapid evaporation of liquid on a heated surface. Int J Heat Mass Tran 45(18):3771 – 3780

Kind R, Potapczuk M, Feo A, Golia C, Shah A (1998) Experimental and computational simulation of in-flight icing phenomena. Prog in Aero Sci 34(5-6):257 – 345

Li X, Pozrikidis C (1996) Shear flow over a liquid drop adhering to a solid surface. J Fluid Mech 307:167–190

Macdougall G, Ockrent C (1942) Surface energy relations in liquid/solid systems. I. The adhesion of liquids to solids and a new method of determining the surface tension of liquids. P Roy Soc A-Math Phy 180(981):151–173

Marmur A (1996) Equilibrium contact angles: theory and measurement. Colloid Surface A 116(1-2):55–61

Marmur A (2006) Soft contact: measurement and interpretation of contact angles. Soft Matter 2:12–17

McAlister G, Ettema R, Marshall JS (2005) Wind-driven rivulet breakoff and droplet flows in microgravity and terrestrial-gravity conditions. J Fluid Eng 127(2):257–266

Meiron TS, Marmur A, Saguy I (2004) Contact angle measurement on rough surfaces. J Colloid Interf Sci 274(2):637 – 644

Messinger BL (1953) Equilibrium temperature of an unheated icing surface as a function of airspeed. J Aero Sci 20:29–41

Milne AJB, Amirfazli A (2009) Drop shedding by shear flow for hydrophilic to superhydrophobic surfaces. Langmuir 25(24):14,155–14,164

Olsen W, Walker E (1986) Experimental evidence for modifying the current physical model of ice accretion on aircraft surfaces. NASA TM 87184, NASA Lewis Research Center

Podgorski T, Flesselles JM, Limat L (2001) Corners, cusps, and pearls in running drops. Phys Rev Lett 87(3):036,102

Press WH, Teukolsky SA, Vetterling WT, Flannery BP (1992) Numerical recipes in C (2nd ed.): the art of scientific computing. Cambridge University Press, New York, NY, USA

Rio E, Daerr A, Andreotti B, Limat L (2005) Boundary conditions in the vicinity of a dynamic contact line: Experimental investigation of viscous drops sliding down an inclined plane. Phys Rev Lett 94(2):024,503

Schlichting H (2000) Boundary-layer theory. Springer, Berlin New York

Schmucker JA (2007) A technique for measurement of water droplet profiles for use in icing physics studies. Master's thesis, Case Western Reserve University, Cleveland, OH

Schmucker JA, White EB (2007) Technique for measurement of droplet profiles for use in icing physics studies. SAE

Schmucker JA, Osterhout JC, White EB (2012) Speckle technique for dynamic drop profile measurement on rough surfaces. Exp Fluids 52:123–136

Stalder AF, Kulik G, Sage D, Barbieri L, Hoffmann P (2006) A snake-based approach to accurate determination of both contact points and contact angles. Colloid Surface A

Tadmor R, Yadav PS (2008) As-placed contact angles for sessile drops. J Colloid Interf Sci 317(1):241 – 246

Theodorakakos A, Ous T, Gavaises M, Nouri J, Nikolopoulos N, Yanagihara H (2006) Dynamics of water droplets detached from porous surfaces of relevance to PEM fuel cells. J Colloid Interf Sci 300(2):673 – 687

Wenzel RN (1936) Resistance of solid surfaces to wetting by water. Ind Eng Chem 28(8):988–994

Westerweel J (1993) Digital particle image velocimetry — theory and application. PhD thesis, Delft University of Technology, Delft

Westerweel J (1997) Fundamentals of digital particle image velocimetry. Meas Sci Tech 8(12):1379–1392

White E, Schmucker J (2008) A Runback Criterion for Water Drops in a Turbulent Accelerated Boundary Layer. J Fluid Eng 130:061,302

Wolansky G, Marmur A (1999) Apparent contact angles on rough surfaces: the Wenzel equation revisited. Colloid Surface A 156(1-3):381 – 388

Wright W (2008) User's manual for LEWICE version 3.2. Final contractor report, National Aeronautics and Space Administration

VITA

Jason Allen Schmucker began undergraduate studies at Goshen College in August 2001 and received his Bachelor of Arts degree in Physics from Goshen College, Goshen, Indiana in April 2005. His Master of Science degree in Mechanical Engineering was awarded in August 2007 from Case Western Reserve University, Cleveland, OH. He began his graduate study at Texas A&M University in August 2007 under Dr. Edward White. His research interests include experimental aerodynamics, measurement techniques, and drop stability.

Mr. Schmucker may be reached by email at schmucker.jason@gmail.com or by contacting Dr. Edward White, Department of Aerospace Engineering, Texas A&M University, College Station, TX 77843-3141.